Monthly Notices
of the
ROYAL ASTRONOMICAL SOCIETY

MNRAS **456,** 3671–3701 (2016) doi:10.1093/mnras/stv2906

Formation and stellar spin-orbit misalignment of hot Jupiters from Lidov–Kozai oscillations in stellar binaries

Kassandra R. Anderson,★ Natalia I. Storch† and Dong Lai

Cornell Center for Astrophysics and Planetary Science, Department of Astronomy, Cornell University, Ithaca, NY 14853, USA

Accepted 2015 December 8. Received 2015 October 29

ABSTRACT

Observed hot Jupiter (HJ) systems exhibit a wide range of stellar spin-orbit misalignment angles. This paper investigates the inward migration of giant planets due to Lidov–Kozai (LK) oscillations induced by a distant stellar companion. We conduct a large population synthesis study, including the octupole gravitational potential from the stellar companion, mutual precession of the host stellar spin axis and planet orbital axis, tidal dissipation in the planet and stellar spin-down in the host star due to magnetic braking. We consider a range of planet masses (0.3–5 $M_{\rm J}$) and initial semimajor axes (1–5 au), different properties for the host star, and varying tidal dissipation strengths. The fraction of systems that result in HJs depends on planet mass and stellar type, with $f_{\rm HJ} = 1$–4 per cent (depending on tidal dissipation strength) for $M_{\rm p} = 1\,M_{\rm J}$, and larger (up to 8 per cent) for more massive planets. The production efficiency of 'hot Saturns' ($M_p = 0.3M_{\rm J}$) is much lower, because most migrating planets are tidally disrupted. We find that the fraction of systems that result in either HJ formation or tidal disruption, $f_{\rm mig} \simeq 11$–14 per cent is roughly constant, having little variation with planet mass, stellar type and tidal dissipation strength. The distribution of final HJ stellar obliquities exhibits a complex dependence on the planet mass and stellar type. For $M_p = (1$–$3)M_{\rm J}$, the distribution is always bimodal, with peaks around 30° and 130°. The distribution for $5M_{\rm J}$ planets depends on host stellar type, with a preference for low obliquities for solar-type stars, and higher obliquities for more massive (1.4 $M_\odot$) stars.

Key words: planets and satellites: dynamical evolution and stability – planet–star interactions – binaries: general.

1 INTRODUCTION

The growing sample of close-in giant planets (hot Jupiters, hereafter HJs) continues to yield surprises. These planets (with orbital periods of ∼3 d) could not have formed *in situ*, given the large stellar tidal gravity and radiation fields close to their host stars, and must have formed beyond a few au and migrated inwards. The recent discoveries of many HJs with orbital angular momentum axes that are misaligned with respect to their host star's spin axis (e.g. Hébrard et al. 2008; Narita et al. 2009; Winn et al. 2009; Triaud et al. 2010; Albrecht et al. 2012b; Moutou et al. 2011) has stimulated new studies on the dynamical causes behind such configurations. The presence (or lack) of such misalignment in an HJ system serves as a probe of the planet's dynamical history, and can potentially constrain the planet's migration channel. Therefore, understanding the dynamics behind spin-orbit misalignments is an important endeavor.

HJ systems with low spin-orbit misalignments are commonly thought to have arisen from smooth disc-driven migration, thereby preserving an initially low stellar obliquity.[1] In contrast, systems with high misalignments must have undergone a more disruptive high-eccentricity migration, in which the eccentricity becomes excited to a large value, with subsequent orbital decay due to dissipative tides raised on the planet by the host star. This assumption has been challenged recently with the suggestion of a 'primordial misalignment' (Bate, Lodato & Pringle 2010; Foucart & Lai 2011; Lai, Foucart & Lin 2011; Thies et al. 2011; Batygin 2012; Batygin & Adams 2013; Lai 2014; Spalding & Batygin 2014; Fielding et al. 2015), in which the protoplanetary disc itself becomes tilted with respect to the stellar spin and planets subsequently form and smoothly migrate within the misaligned disc, resulting in close-in planets with large stellar obliquities. Collectively, these works show

★ E-mail: kra46@cornell.edu

† Present address: TAPIR, Walter Burke Institute for Theoretical Physics, Mailcode 350-17, Caltech, Pasadena, CA 91125, USA.

[1] Throughout this paper, we use the terms 'spin-orbit misalignment' and 'stellar obliquity' interchangeably.

that much remains to be done in disentangling the various possible dynamical histories of HJs.

High-eccentricity migration requires either one or more additional planets in the system, or the presence of a stellar binary companion. In the former case, the eccentricity excitation can be caused by strong planet–planet scatterings (Rasio & Ford 1996; Chatterjee et al. 2008; Ford & Rasio 2008; Jurić & Tremaine 2008), and various forms of secular interactions, such as secular chaos with at least three giant planets (Wu & Lithwick 2011) and interactions between two modestly eccentric coplanar planets (Petrovich 2015b), or, most likely, a combination of both (Nagasawa, Ida & Bessho 2008; Beaugé & Nesvorný 2012). In the case of a stellar companion, high eccentricity is achieved from 'Lidov–Kozai' (LK) oscillations (Kozai 1962; Lidov 1962), in which an inclined stellar companion pumps up the planet's eccentricity to values close to unity; during the brief high-eccentricity phases, dissipative tides within the planet cause orbital decay and inward migration, eventually resulting in a planet with an orbital period of a few days (e.g. Wu & Murray 2003; Fabrycky & Tremaine 2007; Naoz, Farr & Rasio 2012; Petrovich 2015a). Note that LK oscillations with tidal dissipation from stellar companions have also been invoked to explain the existence of tight inner binaries in stellar triple systems (e.g. Mazeh & Shaham 1979; Eggleton & Kiseleva-Eggleton 2001; Fabrycky & Tremaine 2007; Naoz & Fabrycky 2014).

To assess the feasibility of HJ formation from the dynamical effects of distant perturbers, searches for both planetary and stellar companions in HJ systems have been conducted. Knutson et al. (2014) searched for radial velocity signatures from distant companions in systems known to host HJs, and estimated a companion occurrence rate of ∼50 per cent for HJ systems (corrected for sample incompleteness), for companion masses in the range ∼1–13$M_{\rm J}$ and separations ∼1–20 au. By direct imaging, Ngo et al. (2015) performed a similar survey for stellar mass companions, and found an occurrence rate of 48 ± 9 per cent for companions at separations ∼50–2000 au; this is larger than 24 per cent, the fraction of binaries (of the same separation range) among solar-type field stars (Raghavan et al. 2010), suggesting that the presence of a stellar companion increases the likelihood of HJ formation. Taken together, Ngo et al. (2015) suggested a total companion fraction (including stars and planets) of ∼70 per cent for systems hosting HJs. Using a combination of adaptive optics imaging and radial velocity, Wang et al. (2015) searched for stellar companions in systems containing *Kepler* Objects of Interest, focusing on gas giant planets with orbital periods ranging from a few days to hundreds of days. They found that the stellar multiplicity fraction of companions with separations between 20 and 200 au is a factor of ∼2 higher for stars hosting a giant planet, compared to a control sample with no planet detections. Since many of the objects in their sample are HJs, this highlights the potential role of companion stars in the formation of close-in giant planets.

Despite these optimistic companion fractions, some aspects of HJ formation via LK oscillations remain problematic. Assuming steady-state formation of HJs, high-eccentricity migration implies the presence of giant planets at wide orbital separations and large eccentricities, with $a \sim$ several au and $e \gtrsim 0.9$ ('supereccentric migrating Jupiters,' Socrates et al. 2012). However, this class of planets is not observed (Dawson, Murray-Clay & Johnson 2015). Whether this apparent lack of ultra-eccentric giant planets is due to the majority of HJs being formed from disc-driven migration, or whether our understanding of high-eccentricity migration needs to be revised remains to be determined. In addition, the discovery that a significant fraction of HJs have giant planet companions at a few au (Knutson et al. 2014), including a number of systems with full orbit solutions for the companions (e.g. Becker et al. 2015; Feng et al. 2015; Neveu-VanMalle et al. 2015), and the observed stellar-metallicity trend of giant planet eccentricities (Dawson & Murray-Clay 2013), suggest that LK oscillations driven by stellar companions may not account for the majority of the observed HJ population. Regardless, these issues clearly highlight the need for a better understanding of all channels of HJ formation.

In this paper, we focus on HJ formation in stellar binaries through LK oscillations with tidal dissipation, and present the results of a large-scale population synthesis. Initial population studies of HJ formation by the LK mechanism included the leading order (quadrupole) gravitational potential of the binary companion on the planet's orbit (Fabrycky & Tremaine 2007; Wu, Murray & Ramsahai 2007; Correia et al. 2011). Naoz et al. (2012) incorporated the octupole potential of the binary (Ford, Kozinsky & Rasio 2000), and showed that the octupole terms could alter the outcome of the population synthesis (e.g. they claimed that the efficiency of HJ production can be significantly increased due to increases in the maximum eccentricity). Taking a slightly different approach, Petrovich (2015a) conducted a thorough octupole-level population synthesis study, focusing on the steady-state distributions of the planet's orbital elements. He showed that the octupole potential leads to a significant increase in the fraction of tidally disrupted planets. Both Naoz et al. (2012) and Petrovich (2015a) have presented results for the distribution of the stellar obliquities of HJs formed in this scenario, showing a broad spread in the spin-orbit misalignment angles (from ∼20° to ∼140°). Thus far, all population studies have focused on a single planet mass ($1M_{\rm J}$) and limited stellar spin properties. However, in a recent paper (Storch, Anderson & Lai 2014), we showed that gravitational interaction between the planet and its oblate host star can lead to chaotic evolution of the stellar spin axis during LK cycles, and this evolution depends sensitively on the planet mass and stellar rotation period. The chaotic spin dynamics arises from secular spin-orbit resonances and related resonance overlaps (Storch & Lai 2015). In the presence of tidal dissipation, the complex spin evolution can leave an imprint on the final spin-orbit misalignment angles. Thus, the result of Storch et al. (2014) shows that the stellar spin properties and the planet mass can have a strong effect on the distribution of stellar obliquities in HJ systems produced by the LK mechanism. The goal of this paper is to expand upon this previous work by running a large ensemble of numerical simulations with varying planet masses and stellar mass and spin properties. We perform a thorough survey of the parameter space and examine a range of planetary semimajor axes, binary separations, inclinations and eccentricities. We show that, not only the spin-orbit misalignments are affected by stellar types and planet masses, but also the various outcomes of the planets (HJ formation and tidal disruption) are strongly influenced by the properties of the planets and host stars. We also present a number of new analytical calculations and estimates to help understand our numerical population synthesis results.

This paper is organized as follows. In Section 2, we describe the problem setup and present the secular equations of motion that govern the evolution of the system. Section 3 presents several analytical results for understanding the dynamics of the planet's orbit and stellar spin evolution – these results will be useful for interpreting the numerical calculations of later sections. In Section 4, we investigate the properties of the stellar spin evolution, and illustrate the various possible paths of generating spin-orbit misalignments. Section 5 presents our population synthesis calculations. We first discuss results (with and without octupole effects) for a given value

of binary separation and initial planet semimajor axis (Sections 5.2 and 5.3; Table 2). The most general population synthesis results are presented in Sections 5.4 and 5.5 (Table 3). We conclude in Section 6 with a summary of results and discussion of their implications.

2 FORMULATION

We consider a hierarchical triple system, consisting of an inner binary (host star and planet) of masses $M_\star$ and $M_{\rm p}$, with a distant, inclined outer (stellar) companion $M_{\rm b}$. The planet and binary companion have semimajor axes a and $a_{\rm b}$, respectively, with $a/a_{\rm b} \ll 1$. We include the secular gravitational perturbations on the planet from the outer companion to octupole order in the disturbing potential, along with spin-orbit coupling between the oblate host star and planet, tidal dissipation within the planet and periastron precession due to various short-range forces (SRFs, General Relativity, and rotational and tidal distortions of the planet). We ignore the perturbations from the inner binary ($M_\star$ and $M_{\rm p}$) on the outer binary ($M_\star$ and $M_{\rm b}$). The planetary orbit is characterized by the unit vectors ($\hat{\boldsymbol{L}}$, $\hat{\boldsymbol{e}}$), where $\hat{\boldsymbol{L}}$ is normal to the orbital plane (in the direction of the angular momentum vector $\boldsymbol{L}$) and $\hat{\boldsymbol{e}}$ is in the direction of the eccentricity vector $\boldsymbol{e}$. Similarly, the orbit of the outer binary is characterized by the unit vectors ($\hat{\boldsymbol{L}}_{\rm b}$, $\hat{\boldsymbol{e}}_{\rm b}$). The invariant plane is determined by the outer binary angular momentum axis $\hat{\boldsymbol{L}}_{\rm b}$. The secular equations of motion for the planetary orbit take the forms

$$\frac{{\rm d}\boldsymbol{L}}{{\rm d}t} = \left.\frac{{\rm d}\boldsymbol{L}}{{\rm d}t}\right|_{\rm LK} + \left.\frac{{\rm d}\boldsymbol{L}}{{\rm d}t}\right|_{\rm SL} + \left.\frac{{\rm d}\boldsymbol{L}}{{\rm d}t}\right|_{\rm Tide}, \tag{1}$$

and

$$\frac{{\rm d}\boldsymbol{e}}{{\rm d}t} = \left.\frac{{\rm d}\boldsymbol{e}}{{\rm d}t}\right|_{\rm LK} + \left.\frac{{\rm d}\boldsymbol{e}}{{\rm d}t}\right|_{\rm SL} + \left.\frac{{\rm d}\boldsymbol{e}}{{\rm d}t}\right|_{\rm SRF} + \left.\frac{{\rm d}\boldsymbol{e}}{{\rm d}t}\right|_{\rm Tide}, \tag{2}$$

where we are including contributions from the binary companion that give rise to LK oscillations, spin-orbit coupling between the host star spin $S_\star$ and L (SL), dissipative tides (Tide) within the planet and periastron precession due to SRFs. Explicit forms for each term are given in Appendix A.

Note that the 'LK' term from the binary companion consists of two pieces: a quadrupole term, and an octupole term. The quadrupole has a characteristic time-scale for LK oscillations t_k, given by

$$\frac{1}{t_k} = \frac{M_{\rm b}}{M_{\rm tot}}\frac{a^3}{a_{b,\rm eff}^3}n = \left(\frac{2\pi}{10^6{\rm yr}}\right)\frac{\bar{M}_b\bar{a}^{3/2}}{\bar{M}_{\rm tot}^{1/2}\bar{a}_{b,\rm eff}^3}, \tag{3}$$

where $a_{b,\rm eff} \equiv a_{\rm b}\sqrt{1-e_{\rm b}^2}$, and $n = \sqrt{GM_{\rm tot}/a^3}$ is the planetary mean motion. The octupole term has a relative 'strength' $\varepsilon_{\rm oct}$ (compared to the quadrupole contribution), given by

$$\varepsilon_{\rm oct} = \frac{M_\star - M_{\rm p}}{M_\star + M_{\rm p}}\frac{a}{a_{\rm b}}\frac{e_{\rm b}}{1-e_{\rm b}^2}. \tag{4}$$

(See Table 1 for a summary of various physical quantities and their normalized forms used throughout the paper.) In terms of the unit vector $\hat{\boldsymbol{L}}$, the effect of the binary companion is to induce precession of $\hat{\boldsymbol{L}}$ around $\hat{\boldsymbol{L}}_{\rm b}$, with simultaneous nutation. The rate of change of $\hat{\boldsymbol{L}}$ due to the quadrupole potential of the binary companion is given by

$$\Omega_{\rm L} = \left|\frac{{\rm d}\hat{\boldsymbol{L}}}{{\rm d}t}\right|_{\rm LK,Quad} = \left[(\Omega_{\rm pl}\sin\theta_{\rm lb})^2 + \dot{\theta}_{\rm lb}^2\right]^{1/2}, \tag{5}$$

where $\Omega_{\rm pl} = \dot{\Omega}$, the precession rate of the classical orbital node Ω, and $\theta_{\rm lb}$ (defined as $\cos\theta_{\rm lb} = \hat{\boldsymbol{L}}\cdot\hat{\boldsymbol{L}}_{\rm b}$) is the angle between the planet orbital axis $\hat{\boldsymbol{L}}$ and the binary axis $\hat{\boldsymbol{L}}_{\rm b}$. The first term in equation (5) represents precession of $\hat{\boldsymbol{L}}$ around the binary axis $\hat{\boldsymbol{L}}_{\rm b}$, and the second term represents nutation of $\hat{\boldsymbol{L}}$. An approximate expression for $\Omega_{\rm L}$ as a function of e and $\theta_{\rm lb}$ is (see appendix)

$$\Omega_L \simeq \frac{3(1+4e^2)}{8t_k\sqrt{1-e^2}}|\sin 2\theta_{\rm lb}|. \tag{6}$$

(Note that equation (6) is exact at $e = 0$ and the maximum eccentricity.) At zero eccentricity the expression becomes

$$\Omega_{\rm L}|_{e=0} = \frac{3}{4t_k}\cos\theta_{\rm lb}\sin\theta_{\rm lb} \simeq 4.71\times10^{-6}{\rm yr}^{-1}\frac{\bar{M}_b\bar{a}^{3/2}}{\bar{M}_{\rm tot}^{1/2}\bar{a}_{b,\rm eff}^3}\cos\theta_{\rm lb}\sin\theta_{\rm lb}. \tag{7}$$

2.1 Spin evolution due to stellar quadrupole

The oblate host star has angular momentum $\boldsymbol{S}_\star = I_\star\Omega_\star\hat{\boldsymbol{S}}_\star$, where $I_\star = k_\star M_\star R_\star^2$ is the moment of inertia, with $k_\star \simeq 0.1$ for a solar-type star (Claret & Gimenez 1992), $\Omega_\star$ is the stellar spin frequency (with period $P_\star = 2\pi/\Omega_\star$), and $\hat{\boldsymbol{S}}_\star = \boldsymbol{S}_\star/S_\star$ is the unit vector along the spin axis. The stellar rotational distortion generates a quadrupole moment, thus introducing a torque between the star and planet. This results in mutual precession of $\boldsymbol{S}_\star$ and $\boldsymbol{L}$ around the total angular momentum $\boldsymbol{J} = \boldsymbol{L} + \boldsymbol{S}_\star$ (we ignore the small contribution to $\boldsymbol{J}$ due to the planet spin, see Section 3.3). The star also spins down via magnetic braking: we adopt the Skumanich law (Skumanich 1972), with ${\rm d}\Omega_\star/{\rm d}t \propto -\Omega_\star^3$. The stellar spin evolution thus has two contributions, and is given by

$$\frac{{\rm d}\boldsymbol{S}_\star}{{\rm d}t} = \left.\frac{{\rm d}\boldsymbol{S}_\star}{{\rm d}t}\right|_{\rm SL} + \left.\frac{{\rm d}\boldsymbol{S}_\star}{{\rm d}t}\right|_{\rm MB} = \Omega_{\rm ps}\hat{\boldsymbol{L}}\times\boldsymbol{S}_\star - \alpha_{\rm MB}I_\star\Omega_\star^3\hat{\boldsymbol{S}}_\star, \tag{8}$$

where the first term describes the precession of $\boldsymbol{S}_\star$ around $\boldsymbol{L}$ (SL), and the second term describes the spin-down due to magnetic braking, with the efficiency parameter $\alpha_{\rm MB}$. In this paper we set $\alpha_{\rm MB} = 1.5\times10^{-14}$ yr to model solar-mass (type G) stars, and $\alpha_{\rm MB} = 1.5\times10^{-15}$ yr to model more massive ($1.4\,{\rm M}_\odot$, type F) stars, as in Barker & Ogilvie (2009). This is consistent with observed stellar rotation periods, with massive stars spinning more rapidly on average (McQuillan, Mazeh & Aigrain 2014), and more sophisticated stellar spin-down models (see Bouvier 2013 for a review).

The precession frequency of $\boldsymbol{S}_\star$ around $\boldsymbol{L}$, $\Omega_{\rm ps}$, is given by

$$\Omega_{\rm ps} = -\frac{3\,GM_{\rm p}(I_3 - I_1)\cos\theta_{\rm sl}}{2a^3j^3S_\star} = -\frac{3}{2}\frac{k_{q\star}}{k_\star}\frac{M_{\rm p}}{M_\star}\frac{R_\star^3}{a^3}\frac{\Omega_\star}{j^3}\cos\theta_{\rm sl} \simeq -1.64\times10^{-7}{\rm yr}^{-1}\frac{\bar{k}_{q\star}\bar{M}_p\bar{R}_\star^3}{\bar{k}_\star\bar{P}_\star\bar{M}_\star\bar{a}^3}\frac{\cos\theta_{\rm sl}}{j^3}, \tag{9}$$

where the stellar spin-orbit angle $\theta_{\rm sl}$ is defined by $\cos\theta_{\rm sl} = \hat{\boldsymbol{L}}\cdot\hat{\boldsymbol{S}}_\star$, $j = \sqrt{1-e^2}$, and the stellar quadrupole moment $(I_3 - I_1)$ is related to the spin frequency via $(I_3 - I_1) = k_{q\star}M_\star R_\star^2\hat{\Omega}_\star^2$. Here $\hat{\Omega}_\star = \Omega_\star(GM_\star/R_\star^3)^{-1/2}$ is the stellar rotation rate in units of the breakup frequency, and $k_{q\star}$ is a 'rotational distortion coefficient' (we adopt the canonical value $k_{q\star} = 0.05$ in this paper; Claret & Gimenez 1992).[2] The stellar quadrupole also affects the planet's

[2] Note that $k_{q\star}$ is related to the apsidal motion constant κ, the Love number k_2 and the J_2 parameter by $k_{q\star} = 2\kappa/3 = k_2/3$ and $J_2 = k_{q\star}\hat{\Omega}_\star^2$.

Table 1. Definitions of variables, along with the canonical value used in this paper (if applicable), and dimensionless form.

Quantity	Dimensionless/normalized form
Vector quantities	
Planet orbital angular momentum $\boldsymbol{L}$	–
Planet eccentricity vector $\boldsymbol{e}$	–
Binary orbital angular momentum $\boldsymbol{L}_{\rm b}$	–
Binary eccentricity vector $\boldsymbol{e}_{\rm b}$	–
Stellar spin angular momentum $\boldsymbol{S}_\star$	–
Planetary spin angular momentum $\boldsymbol{S}_{\rm p}$	–
Physical properties	
Stellar mass $M_\star$	$\bar{M}_\star = M_\star/{\rm M}_\odot$
Stellar radius $R_\star$	$\bar{R}_\star = R_\star/{\rm R}_\odot$
Planet mass $M_{\rm p}$	$\bar{M}_p = M_{\rm p}/M_J$
Planet radius $R_{\rm p}$	$\bar{R}_p = R_{\rm p}/R_J$
Binary companion mass $M_{\rm b}$	$\bar{M}_b = M_{\rm b}/{\rm M}_\odot$
Inner binary total mass $M_{\rm tot} \equiv M_\star + M_{\rm p}$	$\bar{M}_{\rm tot} = M_{\rm tot}/{\rm M}_\odot$
Spin and structure properties	
Spin-orbit angle $\theta_{\rm sl}$ (defined by $\cos\theta_{\rm sl} = \hat{\boldsymbol{L}} \cdot \hat{\boldsymbol{S}}_\star$)	–
Stellar moment of inertia constant $k_\star$ ($I_\star = k_\star M_\star R_\star^2$)	$\bar{k}_\star = k_\star/0.1$
Planet moment of inertia constant $k_{\rm p}$ ($I_{\rm p} = k_{\rm p} M_{\rm p} R_{\rm p}^2$)	$\bar{k}_{\rm p} = k_{\rm p}/0.25$
Stellar rotational distortion coefficient $k_{q\star}$ (see Section 2.1)	$\bar{k}_{q\star} = k_{q\star}/0.05$
Planet rotational distortion coefficient k_{qp} (see Section 2.1)	$\bar{k}_{qp} = k_{qp}/0.17$
Stellar spin period $P_\star = 2\pi/\Omega_\star$	$\bar{P}_\star = P_\star/{\rm d}$
Planet spin period $P_{\rm p} = 2\pi/\Omega_{\rm p}$	$\bar{P}_{\rm p} = P_{\rm p}/{\rm d}$
Tidal properties	
Planet tidal Love number $k_{2{\rm p}}$	$\bar{k}_{2{\rm p}} = k_{2{\rm p}}/0.37$
Tidal lag time $\Delta t_{\rm L}$	–
Tidal enhancement factor χ ($\Delta t_{\rm L} = 0.1\chi\,{\rm sec}$)	–
Orbital properties	
Planet semimajor axis a	$\bar{a} = a/{\rm au}$
Planet eccentricity e	–
Planet inclination $\theta_{\rm lb}$ (relative to outer binary, defined by $\cos\theta_{\rm lb} = \hat{\boldsymbol{L}} \cdot \hat{\boldsymbol{L}}_{\rm b}$)	–
Outer binary semimajor axis $a_{\rm b}$	$\bar{a}_{\rm b} = a_{\rm b}/100{\rm au}$
Outer binary eccentricity $e_{\rm b}$	–
Effective outer binary semimajor axis $a_{b,{\rm eff}} \equiv a_{\rm b}\sqrt{1-e_{\rm b}^2}$	$\bar{a}_{b,{\rm eff}} = a_{b,{\rm eff}}/100{\rm au}$
Orbital mean motion $n = \sqrt{GM_{\rm tot}/a^3}$	–

orbit through a back-reaction torque, and precession of the pericentre (see Section 4.3 and Appendix A).

As discussed in Storch et al. (2014), qualitatively distinct types of behaviour for the stellar spin axis arise, depending on the ratio of the stellar spin precession rate $|\Omega_{\rm ps}|$ to the nodal precession rate due to the binary companion $|\Omega_{\rm L}|$ (see equations 9 and 5):

If $|\Omega_{\rm ps}| \ll |\Omega_{\rm L}|$ throughout the LK cycle, the stellar spin axis effectively precesses around the binary axis $\hat{\boldsymbol{L}}_{\rm b}$, so that the angle between $\hat{\boldsymbol{S}}_\star$ and $\hat{\boldsymbol{L}}_{\rm b}$ is nearly constant. We refer to this as the 'non-adiabatic' regime.

On the other hand, if $|\Omega_{\rm ps}| \gtrsim |\Omega_{\rm L}|$ throughout the LK cycle, the stellar spin axis is strongly coupled to the evolution of the orbital axis. Two different types of behaviour can occur in this 'adiabatic regime'. (i) The stellar spin axis $\hat{\boldsymbol{S}}_\star$ essentially follows the orbital axis $\hat{\boldsymbol{L}}$, with $\theta_{\rm sl} \sim$ constant. For systems that begin with $\hat{\boldsymbol{S}}_\star$ and $\hat{\boldsymbol{L}}$ aligned ($\theta_{\rm sl,\,0} = 0^\circ$), the spin-orbit angle remains relatively small ($\theta_{\rm sl} \lesssim 30^\circ$) throughout the evolution. (ii) The spin-orbit angle is initially small, but gradually increases towards the end of the evolution when the planet semimajor axis has decayed appreciably due to tidal dissipation. In this situation, the final misalignment angle settles to a final value $\theta_{\rm sl,f} < 90^\circ$. We term this behaviour 'adiabatic advection' and will discuss it in Section 4 (see also Storch, Lai & Anderson, 2016, submitted).

Finally, if during the LK cycle, $|\Omega_{\rm ps}| \sim |\Omega_{\rm L}|$, secular resonances develop, and overlapping resonances can lead to complex, and often chaotic behaviour of the stellar spin axis. The spin-orbit angle $\theta_{\rm sl}$ may cross 90°, and a wide distribution of final misalignment angles is possible. Note that $\theta_{\rm sl}$ can also cross 90° in the non-adiabatic regime, but the addition of secular resonances in the trans-adiabatic regime leads to much more complex evolution than the non-adiabatic regime.

To help characterize the dynamics, we introduce an 'adiabaticity parameter' $\mathcal{A}$:

$$\mathcal{A} \equiv \left|\frac{\Omega_{\rm ps}}{\Omega_{\rm L}}\right|. \tag{10}$$

This parameter will be used throughout the paper to help characterize the spin-orbit dynamics. In general, $\mathcal{A}$ is a strong function of eccentricity and time. At the start of the evolution (so that $e \approx 0$)

$$\mathcal{A}_0 \equiv \left|\frac{\Omega_{\rm ps}}{\Omega_{\rm L}}\right|_{e=0} = 0.07\frac{\bar{k}_{q\star}\bar{M}_p\bar{M}_{\rm tot}^{1/2}\bar{R}_\star^3\bar{a}_{b,{\rm eff}}^3}{\bar{k}_\star\bar{M}_\star\bar{M}_b\bar{a}^{9/2}\bar{P}_\star}\left|\frac{\cos\theta_{\rm sl,0}}{\sin 2\theta_{\rm lb,0}}\right|. \tag{11}$$

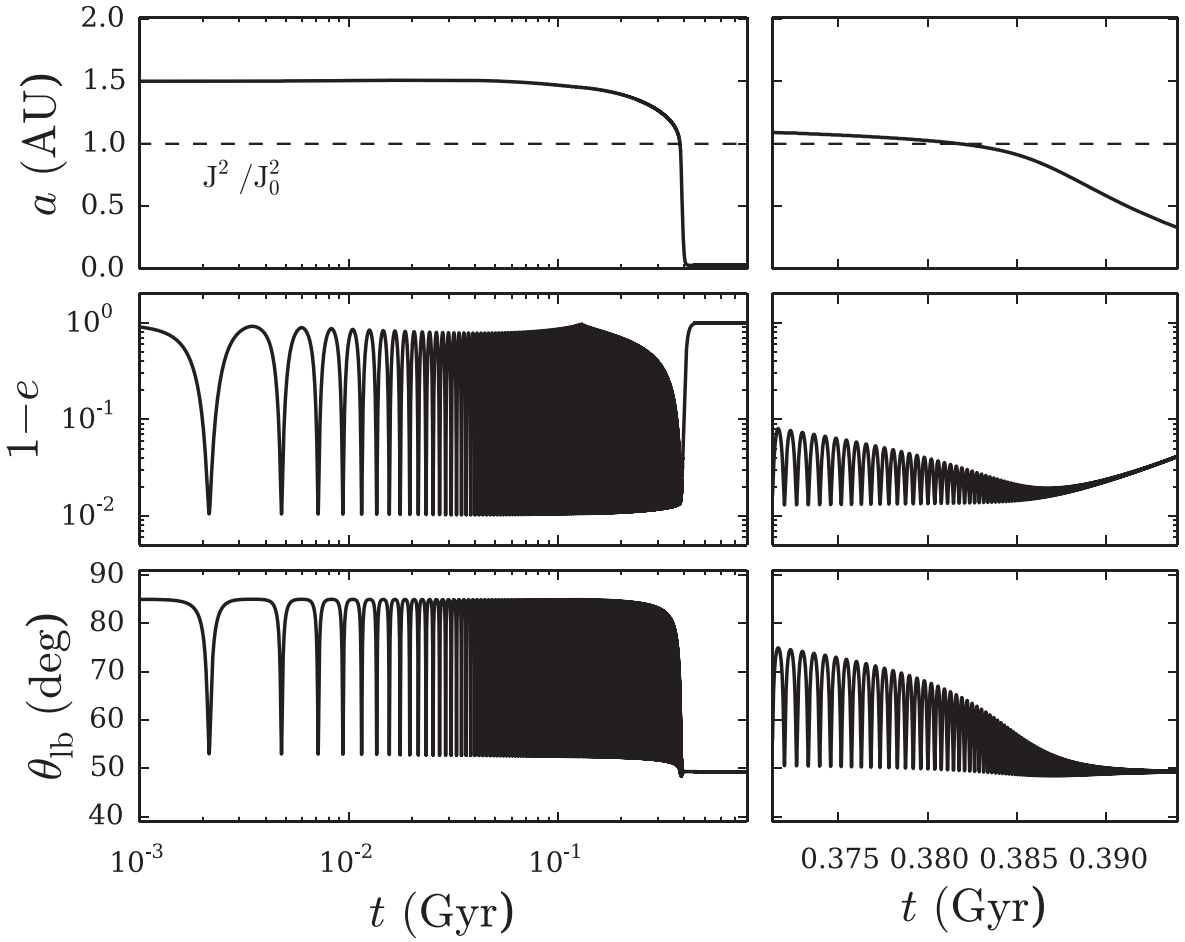

Figure 1. Semimajor axis a (top), eccentricity (middle) and inclination $\theta_{\rm lb}$ (bottom) as functions of time, showing the evolution until the planetary orbit has decayed and circularized (left-hand panels, with logarithmic scale on the x-axis), as well as a zoomed-in version showing the suppression of LK oscillations and tidal decay (right-hand panels, with linear scale on the x-axis). As the orbit decays, the maximum eccentricity of each LK cycle is approximately constant, while the minimum eccentricity steadily increases, until eventually the LK cycles are completely suppressed due to the effects of SRFs. The dashed line shows that the angular momentum projected along the binary axis $\hat{\boldsymbol{L}}_{\rm b}$ (defined by equation 20) is conserved throughout the evolution. Parameters are $M_{\rm p} = 5M_{\rm J}$, $a_0 = 1.5$ au, $a_{\rm b} = 200$ au, $e_{\rm b} = 0$, $\theta_{\rm lb,\,0} = 85^\circ$. The other parameters assume their canonical values, as defined in Table 1.

3 LK MIGRATION AND STELLAR SPIN EVOLUTION: ANALYTICAL RESULTS

Before presenting our detailed population synthesis calculations, we discuss some general properties of LK migration and stellar spin evolution. These will be useful for understanding the results of later sections. Readers interested in the full population synthesis and observational implications are referred to Section 5.

3.1 LK oscillations: range of eccentricity and freezing of oscillations

Fig. 1 gives a 'canonical' example of the formation of an HJ due to LK oscillations with tidal dissipation. For simplicity, this example neglects the feedback of the stellar spin on the orbit. Here we set the binary eccentricity $e_{\rm b} = 0$, so that the octupole-level perturbation from the binary companion vanishes. The planet starts with initial semimajor axis $a_0 = 1.5$ au, and eccentricity $e_0 = 0.01$, and then undergoes cyclic excursions to maximum eccentricity $e_{\rm max}$, with accompanying oscillations in the inclination $\theta_{\rm lb}$ (recall that $\cos\theta_{\rm lb} = \hat{\boldsymbol{L}} \cdot \hat{\boldsymbol{L}}_{\rm b}$), between the initial (maximum) $\theta_{\rm lb,\,0} = 85^\circ$ and minimum (occurring at $e = e_{\rm max}$) $\theta_{\rm lb,max} \approx 53^\circ$. Note that SRFs cause $\theta_{\rm lb,max} > 40^\circ$ here, in contrast to planets subject only to LK oscillations (without SRFs). As the planetary orbit decays, the range of eccentricity oscillations becomes smaller. The example shows that before the oscillations freeze, $e_{\rm max}$ is approximately constant in time, while the minimum eccentricity $e_{\rm min}$ steadily increases towards $e_{\rm max}$. Eventually, when a is sufficiently small, the LK oscillations freeze, and the planet undergoes 'pure' orbital decay/circularization governed by tidal dissipation, at nearly constant angular momentum.

As is well recognized in previous work (e.g. Holman, Touma & Tremaine 1997; Wu & Murray 2003; Fabrycky & Tremaine 2007; Liu, Muñoz & Lai 2015), SRFs play an important role in determining the maximum eccentricity $e_{\rm max}$ in LK cycles. The range of eccentricity oscillations during the LK migration can also be understood from the effects of SRFs, as we discuss below. As in the example depicted in Fig. 1, we ignore the stellar spin feedback on the planetary orbit, as well as octupole-level perturbations from the binary companion.

In the absence of tidal dissipation, the evolution of the planetary orbit is governed by two conservation laws. The first, which is

related to the component of the angular momentum along the binary axis, is the well-known 'Kozai constant', given by

$$K = j\cos\theta_{\rm lb}, \quad \text{where} \quad j = \sqrt{1-e^2}. \tag{12}$$

The second conserved quantity is the energy per unit mass, which in secular form is given by (e.g. Fabrycky & Tremaine 2007; Liu et al. 2015)

$$\Phi = \Phi_{\rm Quad} + \Phi_{\rm GR} + \Phi_{\rm Tide} + \Phi_{\rm Rot}, \tag{13}$$

where the subscripts 'Quad', 'GR', 'Tide' and 'Rot' denote contributions from the binary companion (to quadrupole order), General Relativity, static tidal deformation of the planet, and the rotational deformation of the planet. In terms of the planet's eccentricity (e), inclination ($\theta_{\rm lb}$) and argument of pericentre (ω), the energy (per unit mass) from the binary companion takes the form

$$\Phi_{\rm Quad} = \frac{\Phi_0}{8}\left(1 - 6e^2 - 3\,K^2 + 15e^2\sin^2\theta_{\rm lb}\sin^2\omega\right), \tag{14}$$

where

$$\Phi_0 = \frac{GM_{\rm b}a^2}{a_{b,\rm eff}^3}. \tag{15}$$

The remaining energy terms due to SRFs can be written as

$$\begin{aligned}
\Phi_{\rm GR} &= -\varepsilon_{\rm GR}\frac{\Phi_0}{j},\\
\Phi_{\rm Tide} &= -\varepsilon_{\rm Tide}\frac{\Phi_0}{15}\frac{1+3e^2+3e^4/8}{j^9},\\
\Phi_{\rm Rot} &= -\varepsilon_{\rm Rot}\frac{\Phi_0}{3j^3},
\end{aligned} \tag{16}$$

where we have defined dimensionless parameters $\varepsilon_{\rm GR}$, $\varepsilon_{\rm Tide}$ and $\varepsilon_{\rm Rot}$ that quantify the 'strengths' of the SRFs:

$$\varepsilon_{\rm GR} \equiv \frac{3GM_{\rm tot}^2 a_{b,\rm eff}^3}{M_{\rm b}a^4c^2} \simeq 0.03\frac{\bar{M}_{\rm tot}^2\bar{a}_{b,\rm eff}^3}{\bar{M}_b\bar{a}^4}, \tag{17}$$

$$\begin{aligned}
\varepsilon_{\rm Tide} &\equiv \frac{15k_{2\rm p}M_\star M_{\rm tot}a_{b,\rm eff}^3R_{\rm p}^5}{M_{\rm b}M_{\rm p}a^8}\\
&\simeq 1.47\times10^{-7}\frac{\bar{M}_\star\bar{M}_{\rm tot}\bar{a}_{b,\rm eff}^3\bar{R}_p^5}{\bar{M}_b\bar{M}_p\bar{a}^8},
\end{aligned} \tag{18}$$

$$\begin{aligned}
\varepsilon_{\rm Rot} &\equiv \frac{3k_{qp}}{2}\hat{\Omega}_{\rm p}^2\frac{M_{\rm tot}}{M_{\rm b}}\left(\frac{R_{\rm p}}{a}\right)^2\left(\frac{a_{b,\rm eff}}{a}\right)^3\\
&\simeq 8.48\times10^{-4}\bar{k}_{qp}\left(\frac{P_{\rm p}}{1\,\rm d}\right)^{-2}\frac{\bar{M}_{\rm tot}\bar{R}_p^5\bar{a}_{b,\rm eff}^3}{\bar{M}_p\bar{M}_b\bar{a}^5}.
\end{aligned} \tag{19}$$

(see Table 1 for definitions of $k_{2\rm p}$ and k_{qp}).

With tidal dissipation included, the semimajor axis is no longer constant. We expect that the first conservation law, equation (12) is replaced by

$$J = \sqrt{a(1-e^2)}\cos\theta_{\rm lb} = \sqrt{a}\,j\cos\theta_{\rm lb}. \tag{20}$$

Fig. 1 shows that J is indeed conserved to high precision throughout the LK migration. With $a \neq$ constant, the energy expression, equation (14) is no longer conserved. However, since the time-scale for tidal dissipation (see Section 3.2, equation 32) is much longer than the time-scale for LK oscillations (equation 3), the energy is very nearly constant over a single LK cycle.

As seen from Fig. 1, during the oscillatory phase of the LK migration, the maximum eccentricity of each LK cycle $e_{\rm max} \approx$ constant, while the minimum eccentricity steadily increases, so that the range of eccentricity variation narrows (see right-hand panels of Fig. 1). The inclination at maximum eccentricity, $\theta_{\rm lb,max}$, is also nearly constant. For given $e_{\rm max}$ and $\theta_{\rm lb,max}$, the minimum eccentricity $e_{\rm min}$ can be determined using the two (approximate) conservation laws, giving

$$\begin{aligned}
\frac{3}{4}e_{\rm min}^2 = \frac{3}{8}e_{\rm max}^2\left(2 - 5\sin^2\theta_{\rm lb,max}\right)\\
+\left[\frac{\varepsilon_{\rm GR}}{j} + \frac{\varepsilon_{\rm Tide}}{15j^9}\left(1+3e^2+\frac{3e^4}{8}\right) + \frac{\varepsilon_{\rm Rot}}{3j^3}\right]\Bigg|_{e_{\rm min}}^{e_{\rm max}}.
\end{aligned} \tag{21}$$

Here we have used the fact that the maximum eccentricity occurs when $\omega = \pi/2$ or $3\pi/2$, while the minimum eccentricity occurs at $\omega = 0$ or π (provided that ω is in the circulating, rather than librating regime). For reasonable values of the planetary rotation rate (see Section 3.3), the SRF effect due to the rotational bulge can be neglected compared to the tidal effect.

We can now determine the condition for the suppression (freezing) of LK oscillations. Since the freezing occurs at $e_{\rm max}$ close to 1, it is more appropriate to consider the freezing of j. For $\Delta j \equiv j_{\rm min} - j_{\rm max} = \sqrt{1-e_{\rm min}^2} - \sqrt{1-e_{\rm max}^2} \ll j_{\rm max}$, we find that

$$\frac{\Delta j}{j_{\rm max}} \approx \frac{15}{8}\sin^2\theta_{\rm lb,max}\left(\frac{\varepsilon_{\rm GR}}{j_{\rm max}} + \frac{21}{8}\frac{\varepsilon_{\rm Tide}}{j_{\rm max}^9}\right)^{-1}. \tag{22}$$

(Note that the subscript 'max' indicates the value at maximum eccentricity.) As a decreases, both $\varepsilon_{\rm GR}$ and $\varepsilon_{\rm Tide}$ increase rapidly, which leads to the decrease of Δj. The fact that $\theta_{\rm lb,max}$ is nearly constant (see Fig. 1), along with conservation of J (see equation 20), together imply that $j_{\rm max} \propto a^{-1/2}$. For $\varepsilon_{\rm GR}/j_{\rm max} \gtrsim (21/8)\varepsilon_{\rm Tide}/j_{\rm max}^9$, or

$$j_{\rm max} \gtrsim \left(\frac{21\varepsilon_{\rm Tide}}{8\varepsilon_{\rm GR}}\right)^{1/8} = 0.245\frac{\bar{R}_p^{5/8}}{\bar{M}_p^{1/8}\bar{a}^{1/2}}, \tag{23}$$

the GR term dominates, and we have

$$\frac{\Delta j}{j_{\rm max}} \simeq 0.1\frac{\bar{M}_b}{\bar{M}_\star^2\bar{a}_{b,\rm eff}^2}\left(\frac{a}{0.3\,\rm au}\right)^4\left(\frac{j_{\rm max}}{0.2}\right)\sin^2\theta_{\rm lb,max}. \tag{24}$$

When equation (23) is not satisfied, the tidal term dominates, and we have

$$\frac{\Delta j}{j_{\rm max}} \simeq 0.01\frac{\bar{M}_b\bar{M}_p}{\bar{M}_\star^2\bar{a}_{b,\rm eff}^3}\left(\frac{a}{0.5\,\rm au}\right)^8\left(\frac{j_{\rm max}}{0.2}\right)^9\sin^2\theta_{\rm lb,max}. \tag{25}$$

Fig. 2 shows $\Delta j/j_{\rm max}$ as a function of a using equation (22) (where $j_{\rm max}$ has been calculated from equation 20), for the same system parameters as depicted in Fig. 1, and three values of $\theta_{\rm lb,0}$. We see that $\Delta j/j_{\rm max}$ decreases with decreasing a, as SRFs increasingly suppress the LK oscillations.

3.2 Migration rate: upper limit and estimate

For a given a and e, the orbital decay rate (using weak friction tidal theory) takes the form (Alexander 1973; Hut 1981)

$$\left(\frac{1}{a}\frac{{\rm d}a}{{\rm d}t}\right)_{\rm Tide} = -\frac{1}{t_a}\frac{1}{j^{15}}\left[f_1(e) - j^3 f_2(e)\frac{\Omega_{\rm p}}{n}\right], \tag{26}$$

where the dimensionless functions of eccentricity f_1 and f_2 are defined in equations (A18) and (A19). The time-scale t_a is given by

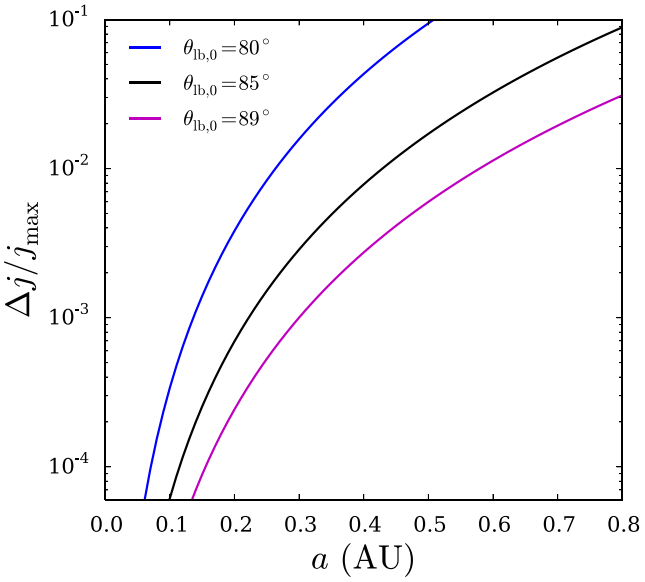

Figure 2. Condition for freezing of LK oscillations, $\Delta j/j_{\max}$ as a function of a using equation (22) (where we assumed $\Delta j/j_{\max} \ll 1$), where $j_{\max} = \sqrt{1-e_{\max}^2}$ has been calculated from equation (20), with the assumption that $\theta_{\rm lb,max} \sim \theta_{\rm lb,0}$. We have chosen three values of $\theta_{\rm lb,\,0}$, as labelled, and all other parameters the same as in Fig. 1. As a decreases (so that $\varepsilon_{\rm GR}$ and $\varepsilon_{\rm Tide}$ increase), SRFs limit the eccentricity variation, causing Δj to decrease.

$$\frac{1}{t_a} = 6k_{2\rm p}\Delta t_{\rm L}\frac{M_*}{M_{\rm p}}\left(\frac{R_{\rm p}}{a}\right)^5 n^2 \approx \frac{7.3\times10^{-21}}{\rm yr}\chi\bar{k}_{2\rm p}\frac{\bar{M}_\star\bar{M}_{\rm tot}}{\bar{M}_p}\frac{\bar{R}_p^5}{\bar{a}^8}, \quad (27)$$

where $\Delta t_{\rm L}$ is the lag time, $k_{2\rm p}$ is the tidal Love number, and we have introduced a tidal enhancement factor χ (relative to Jupiter), defined such that $\Delta t_{\rm L} = 0.1\chi$ sec. Our canonical value is $\chi = 10$. It is convenient to introduce the quantity

$$a_{\rm F} \equiv a(1-e_{\max}^2), \quad (28)$$

because $a_{\rm F}$ varies by at most ∼20 per cent during the inward migration of a planet undergoing LK cycles. Note that $a_{\rm F}$ is approximately equivalent to the final ('circularized') semimajor axis of the planet. To produce HJs, we require $a_{\rm F} \lesssim 0.05$ au (i.e. orbital periods less than ∼4 d).

For a given value of the planetary spin rate $\Omega_{\rm p}$, the maximum decay rate occurs for $e = e_{\max}$ (see Section 3.3 for a discussion of our treatment of the planetary spin). Setting $\Omega_{\rm p} \simeq 0$ for simplicity, the maximum decay rate is

$$\left|\frac{1}{a}\frac{{\rm d}a}{{\rm d}t}\right|_{\rm Tide,max} = \frac{1}{t_a}\frac{f_1(e_{\max})}{j_{\max}^{15}} \approx \frac{2.52\times10^{-9}}{\rm yr}\chi\bar{k}_{2\rm p}\frac{\bar{M}_{\rm tot}\bar{M}_\star\bar{R}_p^5}{\bar{M}_p\bar{a}^{1/2}}\left(\frac{\bar{a}_{\rm F}}{0.05}\right)^{-15/2}. \quad (29)$$

Non-zero values of the planetary spin rate $\Omega_{\rm p}$ would slightly modify the numerical coefficient in equation (29).

Equation (29) overestimates the actual LK migration rate, since the planet spends only a small fraction of time near high eccentricity during an LK cycle. We can estimate the time spent in the vicinity of $e_{\max}$ as follows. Neglecting SRFs, the planet's argument of pericentre ω evolves according to

$$\frac{{\rm d}\omega}{{\rm d}t} = \frac{3}{4t_k\sqrt{1-e^2}}\left[2(1-e^2)+5\sin^2\omega(e^2-\sin^2\theta_{\rm lb})\right]. \quad (30)$$

Near maximum eccentricity, ω centres around $\pi/2$ or $3\pi/2$, with width of $\Delta\omega \sim 1$ radian (see, e.g. Holman et al. 1997, fig. 3). Thus, the second term in equation (30) is of order unity and the first term is negligible, so that the time spent near $e_{\max}$ can be approximated by

$$\Delta t(e_{\max}) \sim t_k\sqrt{1-e_{\max}^2}. \quad (31)$$

Thus, the actual orbital decay rate during LK migration is roughly

$$\left|\frac{1}{a}\frac{{\rm d}a}{{\rm d}t}\right|_{\rm Tide,LK} \sim \left|\frac{1}{a}\frac{{\rm d}a}{{\rm d}t}\right|_{\rm Tide,max}(1-e_{\max}^2)^{1/2} \simeq \frac{5.6\times10^{-10}}{\rm yr}\chi\bar{k}_{2\rm p}\frac{\bar{M}_{\rm tot}\bar{M}_\star\bar{R}_p^5}{\bar{M}_p\bar{a}}\left(\frac{\bar{a}_F}{0.05}\right)^{-7} \quad (32)$$

(see also Petrovich 2015a for a more detailed exploration of the LK migration rate). Since the main-sequence lifetime of a solar-type star is ∼10^{10} yr, inward migration resulting in HJ formation requires that $a_{\rm F} \lesssim 0.05$ au.

3.3 Evolution of planet spin during LK cycles with tidal friction

Similar to the spin axis of the host star, the spin axis of the oblate planet $\hat{\boldsymbol{S}}_{\rm p}$ (where the spin angular momentum is $\boldsymbol{S}_{\rm p} = S_{\rm p}\hat{\boldsymbol{S}}_{\rm p}$) precesses around the orbital axis $\hat{\boldsymbol{L}}$ according to

$$\frac{{\rm d}\hat{\boldsymbol{S}}_{\rm p}}{{\rm d}t} = \Omega_{\rm prec,p}\hat{\boldsymbol{L}}\times\hat{\boldsymbol{S}}_{\rm p}, \quad (33)$$

where the precession rate $\Omega_{\rm prec,\,p}$ is given by

$$\Omega_{\rm prec,p} = -\frac{3}{2}\frac{k_{qp}}{k_{\rm p}}\frac{M_\star}{M_{\rm p}}\frac{R_{\rm p}^3}{a^3}\frac{\Omega_{\rm p}}{j^3}\cos\theta_{\rm p} \simeq -2.69\times10^{-4}{\rm yr}^{-1}\frac{\bar{k}_{qp}\bar{M}_\star\bar{R}_p^3}{\bar{k}_{\rm p}\bar{M}_p\bar{a}^3}\frac{\cos\theta_{\rm p}}{j^3}, \quad (34)$$

with $\cos\theta_{\rm p} = \hat{\boldsymbol{S}}_{\rm p}\cdot\hat{\boldsymbol{L}}$ (see Table 1 for definitions and canonical values of all other quantities). We can define a planetary 'adiabaticity parameter' $\mathcal{A}_{\rm p,0}$ (analogous to the stellar adiabaticity parameter $\mathcal{A}_0$, see equation 11), where

$$\mathcal{A}_{\rm p,0} \equiv \left|\frac{\Omega_{\rm prec,p}}{\Omega_{\rm L}}\right|_{e=0} \simeq 57.1\frac{\bar{k}_{qp}\bar{M}_\star\bar{M}_{\rm tot}^{1/2}\bar{R}_p^3\bar{a}_{b,\rm eff}^3}{\bar{k}_{\rm p}\bar{M}_p\bar{M}_b\bar{a}^{9/2}\bar{P}_p}\left|\frac{\cos\theta_{\rm p}}{\cos\theta_{\rm lb}\sin\theta_{\rm lb}}\right|. \quad (35)$$

Clearly, for all plausible parameters, $\mathcal{A}_{\rm p,0} \gg 1$, provided that the planetary obliquity $\theta_{\rm p}$ is not too close to 90°. The planetary spin axis is thus always in the adiabatic regime (see Section 2.1), with the planetary spin-orbit angle $\theta_{\rm p} \approx$ constant.

We thus treat the direction of the planetary spin axis as always being aligned with the orbital axis $\hat{\boldsymbol{L}}$, and the spin magnitude $S_{\rm p} = k_{\rm p}M_{\rm p}R_{\rm p}^2\Omega_{\rm p}$ evolves only due to tidal dissipation. After averaging over the periastron precession (e.g. Alexander 1973; Hut 1981; Correia et al. 2011), the evolution of $S_{\rm p}$ is governed by the expression

$$\left(\frac{1}{S_{\rm p}}\frac{{\rm d}S_{\rm p}}{{\rm d}t}\right)_{\rm Tide} = -\frac{1}{2t_a}\frac{L}{S_{\rm p}}\frac{1}{j^{13}}\left[j^3 f_5(e)\frac{\Omega_{\rm p}}{n} - f_2(e)\right], \quad (36)$$

where f_2 and f_5 are functions of eccentricity, defined in equations (A19) and (A22). The magnitude of the orbital angular momentum evolves according to $({\rm d}L/{\rm d}t)_{\rm Tide} = -({\rm d}S_{\rm p}/{\rm d}t)_{\rm Tide}$.

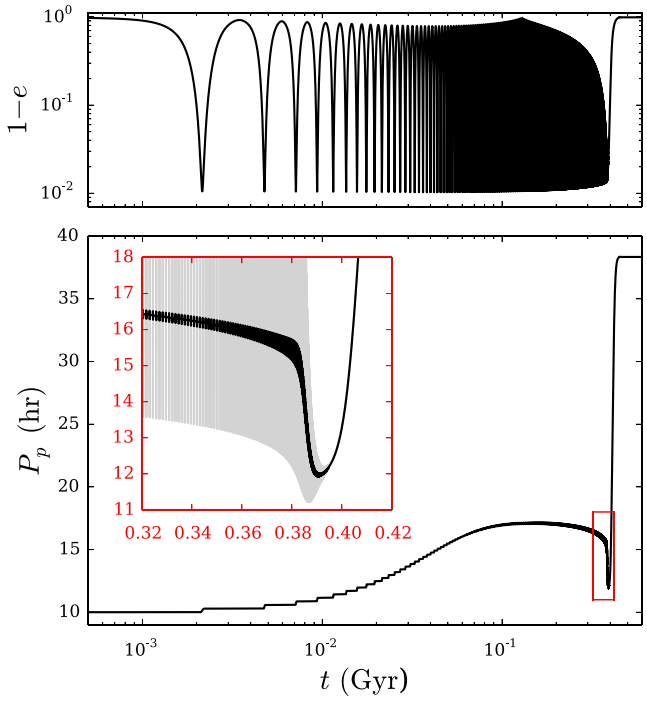

Figure 3. Planet spin period as a function of time, for the same parameters shown in Fig. 1. For reference, we also show the variation of the orbital eccentricity $1 - e$ (top panel). The planet spin remains constant during the low-eccentricity phase of each LK cycle, and undergoes a rapid 'jump' during the brief high-eccentricity phase. The bottom panel shows $P_{\rm p}$ over the entire evolution (until the LK cycles are suppressed and the semimajor axis decays to the final value), and the inset shows a zoomed-in portion of the spin evolution, as indicated by the red-boxed region ($0.32\ {\rm Gyr} \lesssim t \lesssim 0.42\ {\rm Gyr}$). On time-scales much longer than t_k, but shorter than the orbital decay time, the spin period reaches 'Kozai spin equilibrium' (see text). As the LK oscillations are suppressed (see Section 3.1), the equilibrium spin period approaches the pseudo-synchronized value (equation 38), drawn in light grey in the inset panel.

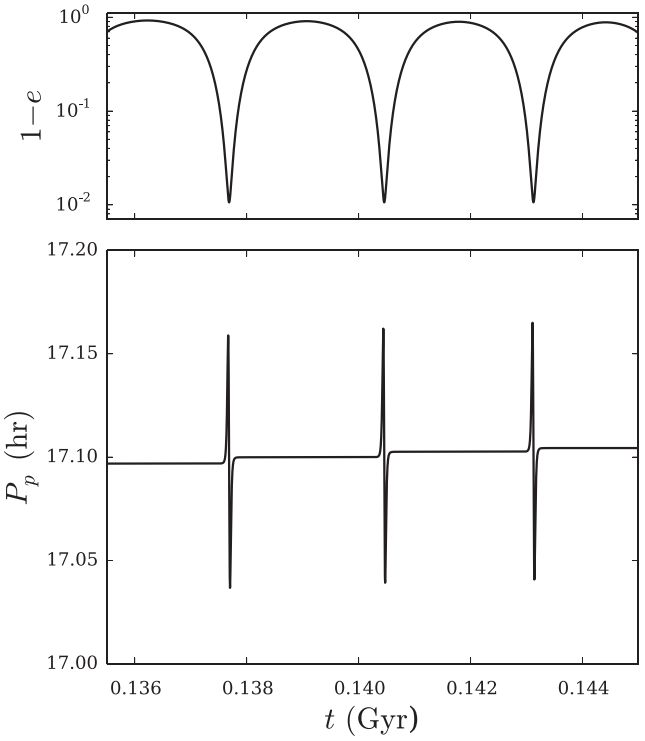

Figure 4. Same as Fig. 3, but showing only three LK cycles, once the planet spin has achieved the 'Kozai spin equilibrium' (see text).

A fiducial example of the planetary spin behaviour is shown in Fig. 3, for the same parameters as in Fig. 1. The planet spin period is initialized to $P_{\rm p} = 10$ h, and exhibits complex behaviour, as it tidally evolves while under the external forcing of the binary companion. During the low-e phase of each LK cycle, the planet spin magnitude remains nearly constant, and then undergoes a rapid 'jump' (with $|\Delta P_{\rm p}|/P_{\rm p} \ll 1$) during the high-$e$ phases. After many LK cycles, a state of near equilibrium is reached, so that the spin period at low eccentricity returns to nearly the same value after the high-e 'jump' (see Fig. 4). As the LK cycles begin to be suppressed due to orbital decay, the range of eccentricity narrows (see Section 3.1), and the spin period gradually decreases. Once the LK cycles are completely suppressed, the spin period increases and eventually settles to a final value $P_{\rm p} \simeq 38$ h, synchronized with the final orbital period of the planet.

We can understand the behaviour of the planetary spin under the influence of LK cycles as follows. The time-scale for planetary spin variation due to tidal dissipation is (see equation 36)

$$t_{\rm spin} = \left|\frac{S_{\rm p}}{\dot{S}_{\rm p}}\right| \sim \frac{S_{\rm p}}{L} t_a j^{13}$$
$$\simeq 2.9\times 10^3 {\rm yr} \frac{\bar{k}_{\rm p}}{\bar{k}_{2{\rm p}}\chi} \frac{\bar{M}_p \bar{a}^{15/2}}{\bar{M}_\star^2 \bar{M}_{\rm tot}^{1/2} \bar{R}_p^3} \left(\frac{P_{\rm p}}{1{\rm day}}\right)^{-1} \left(\frac{j}{0.1}\right)^{12}. \quad (37)$$

This is much less than the orbital decay circularization time-scale due to tides, $t_{\rm circ} \sim t_a j^{13}$, or the orbital decay time ($\sim t_a j^{15}$) for all values of a and e. Therefore, in the absence of an external perturber (i.e. when the system is governed purely by tidal dissipation), the planetary spin reaches a state of pseudo-synchronization, with

$$\Omega_{\rm p,eq} = \Omega_{p,{\rm pseudo}} = \frac{f_2(e)}{j^3 f_5(e)} n. \quad (38)$$

The situation is very different when the planet undergoes LK oscillations driven by an external perturber. The time the planet spends around eccentricity e in each LK cycle is of order $\Delta t_k \sim t_k\sqrt{1-e^2}$ (see equations 3 and 31). Note that the spin evolution time-scale $t_{\rm spin}$ (see equation 37) depends strongly on eccentricity. During the low-eccentricity phase of the LK cycle, $t_{\rm spin} \gg \Delta t_k$, so that the spin magnitude remains constant. However, during the brief high-eccentricity phase, $t_{\rm spin}$ can be comparable to Δt_k and the planetary spin magnitude undergoes a small 'jump' $\Delta\Omega_{\rm p}$. Assuming $|\Delta\Omega_{\rm p}|/\Omega_{\rm p} \ll 1$, this jump can be calculated from

$$\frac{\Delta\Omega_{\rm p}}{\Omega_{\rm p}} \simeq -\int_{-t_k/2}^{t_k/2} \frac{1}{2t_a j^{13}} \frac{L}{S_{\rm p}} \left[j^3 f_5(e)\frac{\Omega_{\rm p}}{n} - f_2(e)\right] {\rm d}t, \quad (39)$$

where $e = e(t)$, and the time integration covers a single LK cycle centred around the eccentricity maximum. On time-scales much longer than t_k but shorter than the orbital decay time, the spin rate approaches a constant value $\Omega_{p,{\rm eq}}$, the 'Kozai spin equilibrium,' such that $\Delta\Omega_{\rm p} = 0$. For 'canonical' system parameters ($M_{\rm p} = 1M_{\rm J}$, $a_0 = 1.5$au, $a_{\rm b} = 200$au), and varying initial inclination (corresponding to varying $e_{\rm max}$), we determine $\Omega_{\rm p,eq}$ by adjusting the initial planetary spin rate, integrating for a single LK cycle and iterating until $\Delta\Omega_{\rm p} = 0$ in equation (39). The results are depicted in Fig. 5. We see that the Kozai spin equilibrium differs from the pseudo-synchronized value at $e_{\rm max}$, with the ratio $\Omega_{\rm p,eq}/\Omega_{\rm p,pseudo}(e_{\rm max}) \approx 0.8$.

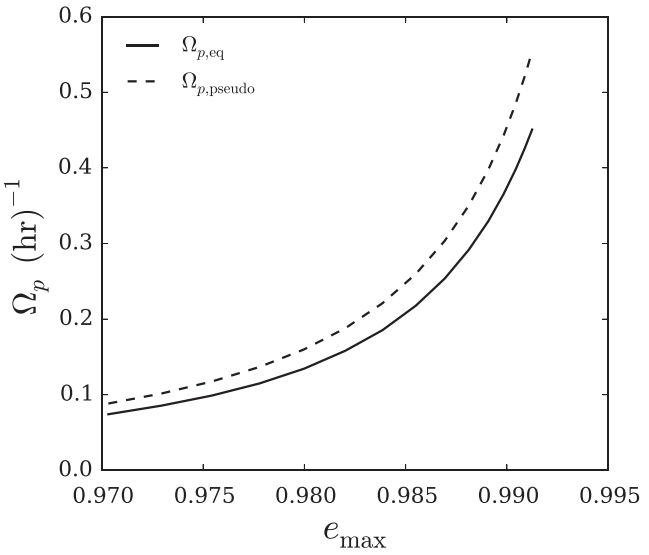

Figure 5. 'Kozai spin equilibrium rate' rate ($\Omega_{\rm p,eq}$, solid curve), as a function of $e_{\rm max}$, the maximum eccentricity attained in an LK cycle. For comparison, we also plot the pseudo-synchronized rate at $e_{\rm max}$ ($\Omega_{\rm p,pseudo}$, dashed curve). We vary the maximum eccentricity by varying the initial inclination $\theta_{\rm lb,\,0}$, and integrate a set of simplified equations for a single LK cycle (accounting for pericentre precession due to GR and static tides, but neglecting the precession due to planetary rotation). We further ignore orbital decay. Parameters are $M_{\rm p} = 1M_{\rm J}$, $a = 1.5$au, $a_{\rm b} = 200$au, $e_{\rm b} = 0$.

3.4 Limiting eccentricity and necessary conditions for planet migration and disruption

When the octupole potential from the binary companion is neglected, the maximum eccentricity $e_{\rm max}$ attained by the planet in LK cycles can be determined by the conservation laws discussed in Section 3.1. If the initial eccentricity of the planet is close to zero and the initial inclination is $\theta_{\rm lb,\,0}$, we find (Liu et al. 2015):

$$\varepsilon_{\rm GR}\left(\frac{1}{j_{\rm max}}-1\right)+\frac{\varepsilon_{\rm Tide}}{15}\left(\frac{1+3e_{\rm max}^2+\frac{3}{8}e_{\rm max}^4}{j_{\rm max}^9}-1\right)+\frac{\varepsilon_{\rm Rot}}{3}\left(\frac{1}{j_{\rm max}^3}-1\right)=\frac{9e_{\rm max}^2}{8j_{\rm max}^2}\left(j_{\rm max}^2-\frac{5}{3}\cos^2\theta_{\rm lb,0}\right). \quad (40)$$

The limiting eccentricity $e_{\rm lim}$ is achieved at $\theta_{\rm lb,\,0} = 90^\circ$. For $e_{\rm max} \simeq 1$, we have

$$\frac{\varepsilon_{\rm GR}}{j_{\rm lim}}+\frac{7\varepsilon_{\rm Tide}}{24j_{\rm lim}^9}\simeq\frac{9}{8}, \quad (41)$$

where

$$j_{\rm lim}\equiv(1-e_{\rm lim}^2)^{1/2}, \quad (42)$$

and we have neglected the effect associated with the planetary rotational bulge (since it is generally smaller than the tidal term).

When the octupole potential is included, the 'Kozai constant' K (equation 12) is no longer a constant of motion, thus equation (40) is not valid. Nevertheless, Liu et al. (2015) show that the limiting eccentricity, as determined by equation (41) still provides an upper limit to the achievable eccentricity in the LK cycles in the presence of SRFs. The effect of the octupole potential is to make the planet undergo occasional excursion into $e_{\rm lim}$ even when $\theta_{\rm lb,\,0} \neq 90^\circ$. In general, $e_{\rm lim}$ can be attained for a range of $\theta_{\rm lb,\,0}$ centred around 90°, with the range becoming wider as the octupole parameter $\varepsilon_{\rm oct}$ increases (see equation 4).

For a given set of system parameters ($M_\star$, $M_{\rm b}$, $M_{\rm p}$, $R_{\rm p}$, a, $a_{\rm b}$, $e_{\rm b}$), equation (41) determines the limiting eccentricity (or limiting periastron distance $a_{\rm p,\,lim} \equiv a[1-e_{\rm lim}]$)

$$0.021\frac{\bar{M}_\star^2\bar{a}_{b,\rm eff}^3}{\bar{M}_b\bar{a}_{\rm p,lim}^{1/2}\bar{a}^{3.5}}+1.89\times10^{-9}\frac{\bar{M}_\star^2\bar{a}_{b,\rm eff}^3\bar{R}_p^5}{\bar{M}_b\bar{M}_p\bar{a}_{\rm p,lim}^{4.5}\bar{a}^{3.5}}=\frac{9}{8}, \quad (43)$$

where we have used equations (17) and (18). For $j_{\rm lim} \gtrsim j_{{\rm lim},\,c}$, where

$$j_{{\rm lim},c}^2=\left(\frac{7\varepsilon_{\rm Tide}}{24\varepsilon_{\rm GR}}\right)^{1/4}=3.46\times10^{-2}\frac{\bar{R}_p^{5/4}}{\bar{M}_p^{1/4}\bar{a}}, \quad (44)$$

the GR effect dominates SRFs, and we have

$$j_{\rm lim}^2=1-e_{\rm lim}^2=7.1\times10^{-4}\left(\frac{\bar{M}_\star^2\bar{a}_{b,\rm eff}^3}{\bar{M}_b\bar{a}^4}\right)^2. \quad (45)$$

For $j_{\rm lim} \lesssim j_{{\rm lim},\,c}$, tides dominate the SRF, and we have

$$j_{\rm lim}^2=1-e_{\rm lim}^2=2.25\times10^{-2}\left(\frac{\bar{M}_\star^2\bar{R}_p^5\bar{a}_{b,\rm eff}^3}{\bar{M}_b\bar{M}_p\bar{a}^8}\right)^{2/9}. \quad (46)$$

As discussed in Section 3.2, for a planet to migrate, its pericentre distance $a_{\rm p}$ must be sufficiently small, so that tidal dissipation can damp and circularize the orbit within a few Gyr. We therefore require $a_{\rm p,lim} \lesssim a_{\rm p,crit}$, where $a_{\rm p,crit}$ is the maximum pericentre distance needed to circularize the orbit within a specified time frame. Note that $a_{\rm p,crit}$ depends on the tidal dissipation strength, and therefore is a fuzzy number. However, for reasonable tidal dissipation strengths, and circularization times of a few Gyr or less, $a_{\rm p,crit} \simeq 0.025$ au (so that $a_{\rm F} \lesssim 0.05$ au). Setting $a_{\rm p,lim} \lesssim a_{\rm p,crit}$, a necessary condition for LK migration is

$$\bar{a}_{b,\rm eff}\lesssim2.03\,\bar{a}^{7/6}\left(\frac{a_{\rm p,crit}}{0.025{\rm au}}\right)^{1/6}\left(\frac{\bar{M}_b}{\bar{M}_\star^2}\right)^{1/3}\times\left[1+0.23\frac{\bar{R}_p^5}{\bar{M}_p}\left(\frac{a_{\rm p,crit}}{0.025{\rm au}}\right)^{-4}\right]^{-1/3}. \quad (47)$$

Note that this is a necessary, but not sufficient condition, because as discussed above, the outer binary must be sufficiently inclined in order for a planet to achieve $e_{\rm lim}$.

The planet is tidally disrupted if the planet's periastron distance is less than the tidal radius (e.g. Guillochon, Ramirez-Ruiz & Lin 2011)

$$r_{\rm Tide}=2.7fR_{\rm p}\left(\frac{M_\star}{M_{\rm p}}\right)^{1/3}, \quad (48)$$

where $f \sim 1$ (we set $f = 1$ for all calculations in this paper). Setting $a_{\rm p,\,lim} \leq r_{\rm Tide}$, we obtain a necessary condition for tidal disruption:

$$\bar{a}_{b,\rm eff}\leq1.81\,\bar{a}^{7/6}(f\bar{R}_p)^{1/6}\left(\frac{\bar{M}_\star}{\bar{M}_p}\right)^{1/18}\left(\frac{\bar{M}_b}{\bar{M}_\star^2}\right)^{1/3}\times\left(1+\frac{3.54\bar{R}_p\bar{M}_p^{1/3}}{f^4\bar{M}_\star^{4/3}}\right)^{-1/3}. \quad (49)$$

Note that since the tidal disruption radius (equation 48) is not a precisely defined quantity (the coefficient f has uncertainties, and it depends on the planetary mass–radius relation, which can vary widely for giant planets), there are associated uncertainties in the disruption condition in equation (49).

Fig. 6 delineates the parameter space in terms of the initial planet semimajor axis a_0 and effective binary separation $a_{\rm b,eff}$ for migration and disruption, as determined from equations (47) and (49) for

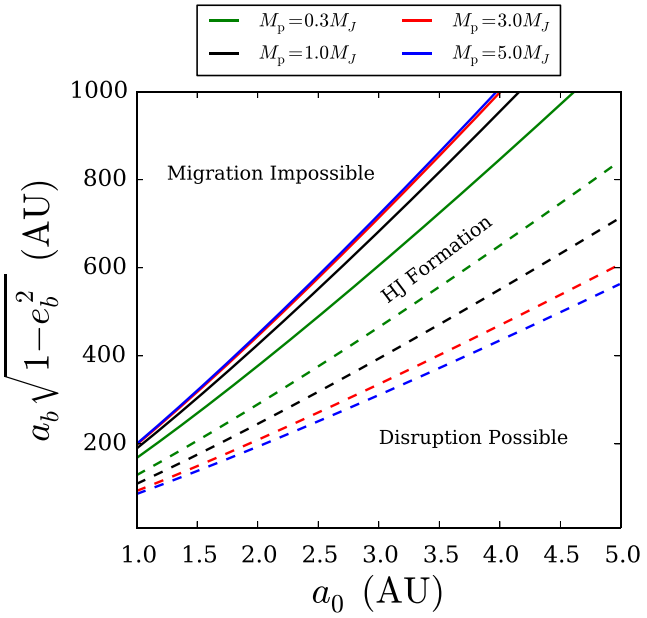

Figure 6. Boundaries in $(a_0, a_{\rm b,eff})$ parameter space for migration (solid lines), and tidal disruption (dashed lines). The migration and disruption boundaries are determined by equation (47) (with $a_{\rm p,crit} = 0.025$ au) and equation (49) (with $f = 1$) for several planet masses (as indicated by the colour). For each planet mass, migration is impossible (for all initial planet-outer binary inclinations) above the solid line, and tidal disruption is impossible above the dashed line. Below the solid (dashed) line, migration (disruption) is possible (depending on the binary inclination), but not guaranteed. HJ formation only occurs below the solid line, and is usually, but not always, confined to the region between the solid and dashed lines.

various planetary masses. For a given planet mass, the parameter space can be divided into a 'Migration Impossible' zone, an 'HJ Formation' zone, and a 'Disruption Possible' zone. Migration is possible below the solid line when the planet is sufficiently inclined relative to the binary, while below the dashed line, tidal disruption is possible. The 'HJ Formation' zone, the region between the solid and dashed lines, narrows substantially with decreasing planet mass, implying that HJ production efficiency should decline with decreasing planet mass. Finally, note that while HJs are never able to form above the solid line, they do occasionally form below the dashed line, for systems where the mutual inclination is not high enough to result in tidal disruption. Therefore, while the upper boundary (solid line) of the HJ formation zone is robust, the lower boundary is somewhat uncertain. However, the vast majority of HJs will reside in the region between the solid and dashed lines.

Further discussion of the planet migration and disruption fractions can be found in Section 5.4.1.

3.5 Freezing of spin-orbit angle

The evolution of the spin-orbit angle $\theta_{\rm sl}$ is complex. Here we examine how $\theta_{\rm sl}$ is frozen into its final value near the end of the LK migration. As shown in Storch & Lai (2015, hereafter SL15), the dynamics of the stellar spin axis $\hat{\boldsymbol{S}}_\star$ relative to the planet's orbital axis $\hat{\boldsymbol{L}}$ depends on three dimensionless ratios

$$\epsilon\beta = -\frac{\Omega_{\rm pl}}{\alpha}\sin\theta_{\rm lb}, \tag{50}$$

$$\epsilon\gamma = \frac{\dot{\theta}_{\rm lb}}{\alpha}, \tag{51}$$

$$\epsilon\psi = -\frac{\Omega_{\rm pl}}{\alpha}\cos\theta_{\rm lb}, \tag{52}$$

where we have defined the function α via

$$\Omega_{\rm ps} = -\alpha\cos\theta_{\rm sl}, \tag{53}$$

and the dimensionless parameter ϵ is defined by

$$\epsilon = \left|\frac{\Omega_{\rm pl}}{\alpha}\right|_{e=0}. \tag{54}$$

The parameter ϵ is related to the 'adiabaticity parameter' $\mathcal{A}_0$ (see equation 11) by $\epsilon = \mathcal{A}_0^{-1}|\cos\theta_{\rm sl,0}/\sin\theta_{\rm lb,0}|$. In general β, γ, ψ are strong functions of time, with the period given by the LK period of the eccentricity variation (when neglecting the feedback effect of the stellar spin on the orbit and the dissipative effect). They can be decomposed into various Fourier components, each giving rise to a resonance (see SL15). Near the end of LK migration, the amplitude of the eccentricity oscillation becomes small (see Section 3.1). So when $\theta_{\rm sl}$ begins to freeze, the dynamics of $\hat{\boldsymbol{S}}_\star$ is dominated by the $N = 0$ (time-independent) components ($\bar{\beta}$ and $\bar{\psi}$, with $\bar{\gamma} = 0$). Thus, the effective Hamiltonian for the stellar spin axis is (see equation 53 of SL15)

$$H = -\frac{1}{2}p^2 + \epsilon\,\bar{\psi}\,p - \epsilon\sqrt{1-p^2}\,\bar{\beta}\cos\phi, \tag{55}$$

where $p = \cos\theta_{\rm sl}$ and ϕ (the phase of precession of $\hat{\boldsymbol{S}}_\star$ around $\hat{\boldsymbol{L}}$) are the conjugate canonical variables. Since H is time-independent, the range of variation of p can be derived from energy conservation. Suppose $p = p_F$ at $\phi = \pi/2$. For $\epsilon \ll 1$, we find

$$p \simeq p_{\rm F} - \frac{\epsilon\bar{\beta}\sqrt{1-p_{\rm F}^2}}{p_{\rm F}}\cos\phi. \tag{56}$$

Thus the spread (full width) of $\theta_{\rm sl}$ as ϕ circulates between 0 and 2π is

$$\Delta\theta_{\rm sl} \simeq \frac{2\epsilon\bar{\beta}}{|\cos\theta_{\rm sl,F}|} = \frac{2}{\mathcal{A}_{\rm F}}, \tag{57}$$

where

$$\mathcal{A}_{\rm F} \equiv \frac{\langle|\Omega_{\rm pl}|\rangle}{\langle|\Omega_{\rm pl}\sin\theta_{\rm lb}|\rangle}. \tag{58}$$

The bracket $\langle ...\rangle$ in equation (58) indicates time averaging over the small 'residual' LK oscillations. If the eccentricity variation is 'frozen' or has small amplitude, then the averaging is unnecessary and $\mathcal{A}_{\rm F}$ is the same as $\mathcal{A}$ defined in equation (10). Thus, in order for the spin-orbit angle to freeze at $\theta_{\rm sl,\,F}$ to within $\Delta\theta_{\rm sl}$ (e.g. 2°) requires

$$\mathcal{A} \gtrsim 60\left(\frac{\Delta\theta_{\rm sl}}{2^\circ}\right)^{-1}. \tag{59}$$

4 PATHS TOWARDS MISALIGNMENT

In this section we present a series of numerical experiments to illustrate various paths of spin-orbit evolution during LK migration. These will be useful for understanding our population synthesis results of the final spin-orbit angles for HJs in Section 5. The theoretical basis for these different evolutionary paths is presented in Storch et al. (2016, submitted).

4.1 Effects of varying stellar spin rate

To isolate the effects of the stellar spin dynamics, and highlight the importance of the stellar spin properties on the final spin-orbit angle,

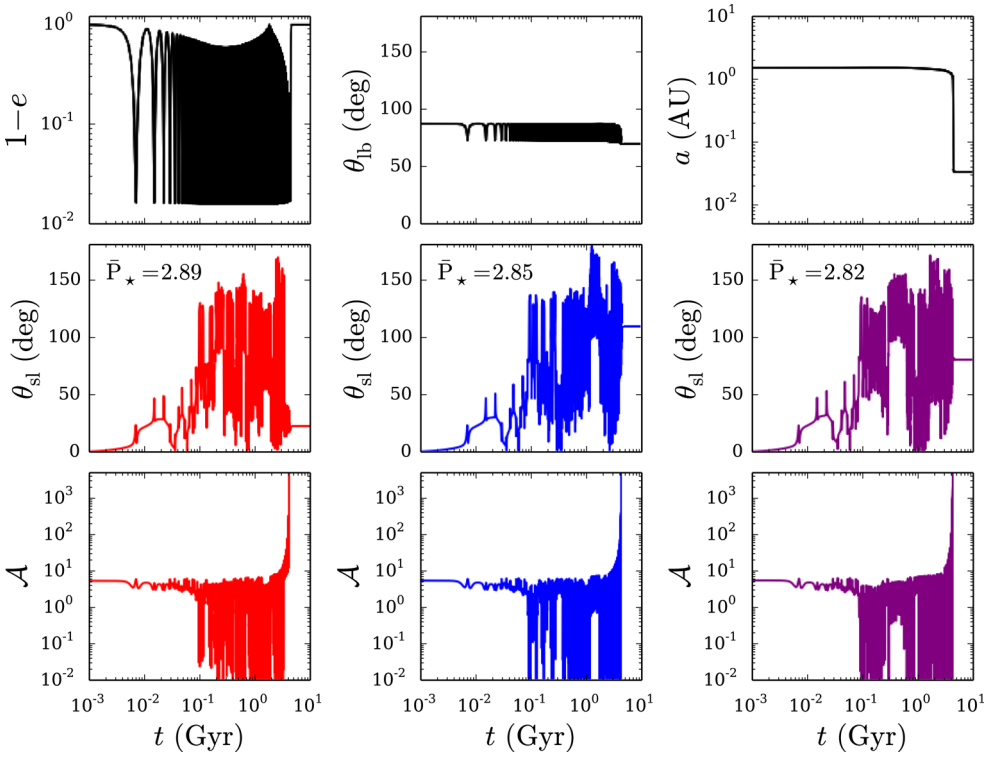

Figure 7. Examples of chaotic evolution for three values of the stellar spin period (in d) as labelled, neglecting the feedback torque from the stellar quadrupole on the orbit. Without feedback, the orbital evolution for each system is identical (shown in the top panels), while the spin-orbit angle settles to a final value that is highly sensitive to the initial conditions. The adiabaticity parameter $\mathcal{A}$ is defined in equation (10). Parameters are $M_{\rm p} = 5M_{\rm J}$, $a_0 = 1.5$ au, $a_{\rm b} = 300$ au, $e_{\rm b} = 0$, $\theta_{\rm lb,\,0} = 87^\circ$.

we first ignore the feedback of the stellar spin on the planetary orbit (thus ignoring the mutual precession of $\boldsymbol{S}_\star$ and $\boldsymbol{L}$). Possible types of evolution are illustrated in Figs 7 and 8. In both figures, we vary the stellar spin period while keeping all other system parameters constant. Fig. 7 presents an example of chaotic spin evolution: three closely spaced values of the stellar spin period result in very different spin evolutions and final spin-orbit misalignments. Fig. 8 presents three different types of non-chaotic spin evolution, only two of which are able to generate spin-orbit misalignment.

The leftmost panel (with $P_\star = 30$ d) of Fig. 8 (with $\theta_{\rm sl}$ in the middle row) shows an example of non-adiabatic spin behaviour. Here, the spin-orbit misalignment angle $\theta_{\rm sl}$ evolves slowly, with step-like changes corresponding to LK eccentricity maxima, during which the spin evolves the most rapidly. Since the planet orbit changes much faster than the spin can respond, the spin axis effectively precesses about the time average of the planet orbital angular momentum vector.

On the opposite end of the spectrum, the middle panel of Fig. 8 (with $P_\star = 7.07$ d) is an example of adiabatic spin behaviour. Here, the stellar spin axis evolves quickly enough that it easily 'keeps up' with the planet angular momentum vector, and hence $\theta_{\rm sl}$ is approximately conserved, making it difficult to generate misalignment.

The rightmost panel of Fig. 8 (with $P_\star = 1.67$ d) shows a more complicated variation of the adiabatic evolution, which we term 'adiabatic advection'. As discussed in detail in SL15, the adiabatic regime of stellar spin evolution is governed by a set of resonances between the time-averaged spin precession rate and the mean LK oscillation rate. Under certain conditions, it is possible for a trajectory to become trapped inside one of the resonances. As tidal dissipation acts to make the system even more adiabatic, the resonance moves in phase space, dragging the trajectory with it and thus generating misalignment. We discuss and clarify the mechanism of this phenomenon in Storch et al. (2016, submitted).

Fig. 9 presents final spin-orbit angles $\theta_{\rm sl,\,f}$ for many different values of the stellar spin period, for three different orbital evolutions (characterized by different initial inclinations $\theta_{\rm lb,\,0}$). This illustrates the role of the adiabaticity parameter $\mathcal{A}_0$ (see equation 11) in determining which of the four types of evolution the spin-orbit angle undergoes. For low values of $\mathcal{A}_0$, chaotic and regular non-adiabatic behaviours are prevalent. For intermediate values, e.g. $10 \lesssim \mathcal{A}_0 \lesssim 100$ in the rightmost panel, adiabatic advection dominates, with each of the striated lines corresponding to adiabatic advection by resonances of different orders (Storch et al. 2016, submitted). For $\mathcal{A}_0 \gtrsim 100$, stationary adiabatic behaviour prevails. Thus, $\mathcal{A}_0$ can be used as an indicator for the behaviour of a system with a particular set of initial conditions.

4.2 Effects of varying inclination

In this subsection we take a different tack and examine the effect of varying the initial planet orbit inclination $\theta_{\rm lb}$, for different values of the stellar spin period and the planet mass. As before, we continue to ignore the back-reaction torque the star exerts on the planet orbit. Fig. 10 demonstrates that changing the initial inclination effectively changes $\mathcal{A}_0$, and thus systems with different initial inclinations can also exhibit the different behaviours shown in Figs 7 and 8 of Section 4.1. In particular, the three columns of Fig. 10 correspond to chaotic evolution (left-hand panels), adiabatic advection (middle panels), and an extreme case of stationary adiabatic evolution (right-hand panels).

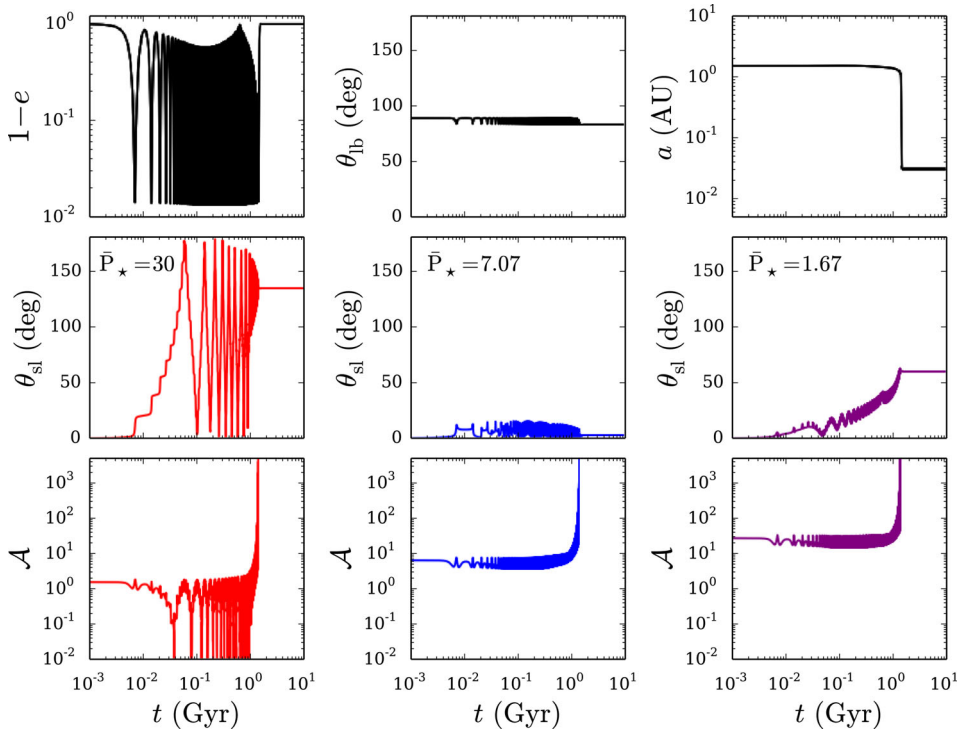

Figure 8. Examples of possible non-chaotic evolution of the spin-orbit angle, depending on the stellar spin rate. As in Fig. 7, feedback has been neglected, so that the orbital evolution, shown in the top row, is identical for all three examples: Non-adiabatic with $P_\star = 30$ d (left), stationary adiabatic with $P_\star = 7.07$ d (middle) and adiabatic advection with $P_\star = 1.67$ d (right). Parameters are $M_\mathrm{p} = 5M_\mathrm{J}$, $a_0 = 1.5$, $a_\mathrm{b} = 300$ au, $e_\mathrm{b} = 0$, $\theta_{\mathrm{lb},0} = 89^\circ$.

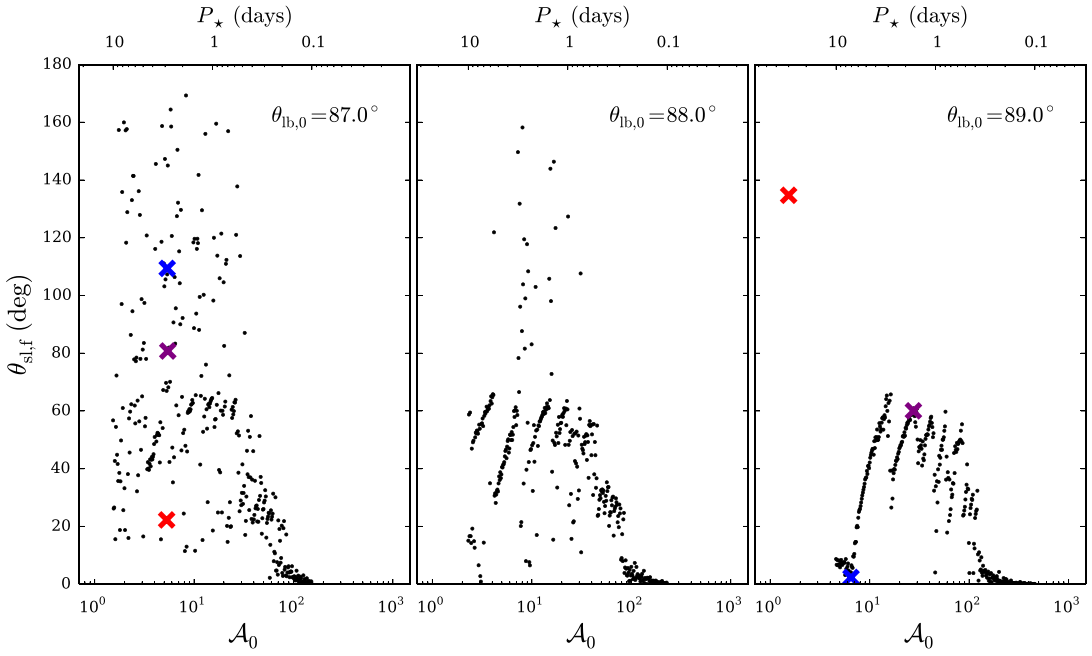

Figure 9. The final spin-orbit angle $\theta_{\mathrm{sl,f}}$ (for systems with planets that undergo inward migration to produce HJs) as a function of the adiabaticity parameter $\mathcal{A}_0$. Here, we vary $\mathcal{A}_0$ by varying $P_\star = 0.1$–10 d (as depicted on the upper x-axis). Results are shown for initial inclinations $\theta_{\mathrm{lb},0} = 87^\circ$ (left), 88° (middle) and 89° (right). The coloured marks correspond to the time evolution presented in Figs 7 and 8. As the initial inclination increases, the adiabaticity parameter $\mathcal{A}_0$ increases, leading to systems with a smaller spread in $\theta_{\mathrm{sl,f}}$. Parameters are $M_\mathrm{p} = 5M_\mathrm{J}$, $a_0 = 1.5$, $a_\mathrm{b} = 300$ au, $e_\mathrm{b} = 0$, no feedback.

In Fig. 11 we show the dependence of the final spin-orbit misalignment angle on the initial inclination, for several combinations of planet mass and stellar spin period. As expected, chaotic behaviour occurs mainly at lower initial inclinations (less adiabatic – see the right two panels of Fig. 11). We note, however, that despite spanning approximately the same range of $\mathcal{A}_0$, heavier planets are much more likely to produce chaotic behaviour than lower mass planets – this implies that $\mathcal{A}_0$ is not the only parameter governing

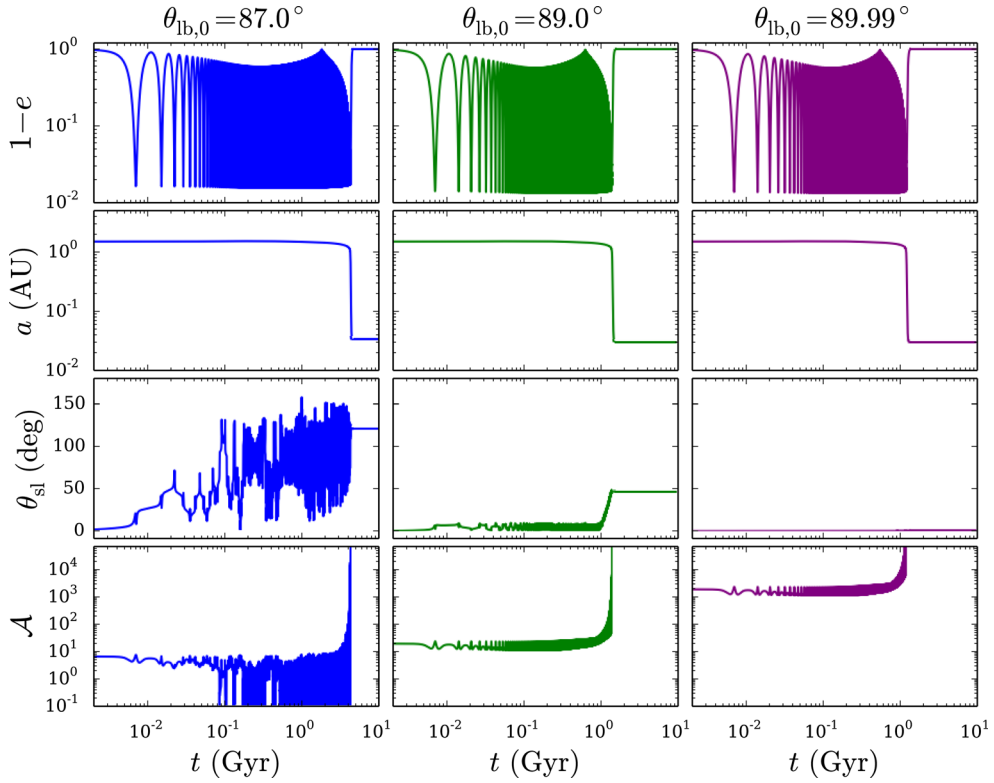

Figure 10. Examples of possible evolution of the spin-orbit angle, depending on the initial inclination. All examples have $M_{\rm p} = 5M_{\rm J}$, $a_0 = 1.5$ au, $a_{\rm b} = 300$ au, $P_\star = 2.3$ d, and the feedback torque from the stellar quadrupole has been neglected. The system with $\theta_{\rm lb,\,0} = 87^\circ$ (left-hand panels) has $\mathcal{A}_0 \lesssim 10$, sufficiently low to generate large spin-orbit misalignments. The system with $\theta_{\rm lb,\,0} = 89^\circ$ (middle panels) has $\mathcal{A}_0 \gtrsim 10$, sufficiently high to preserve the initially low misalignment, but eventually undergoes adiabatic advection (see text). The extreme example shown on the right with $\theta_{\rm lb,\,0} = 89.99^\circ$ has $\mathcal{A}_0 \gtrsim 10^3$, so that $\theta_{\rm sl}$ is very nearly constant for all time.

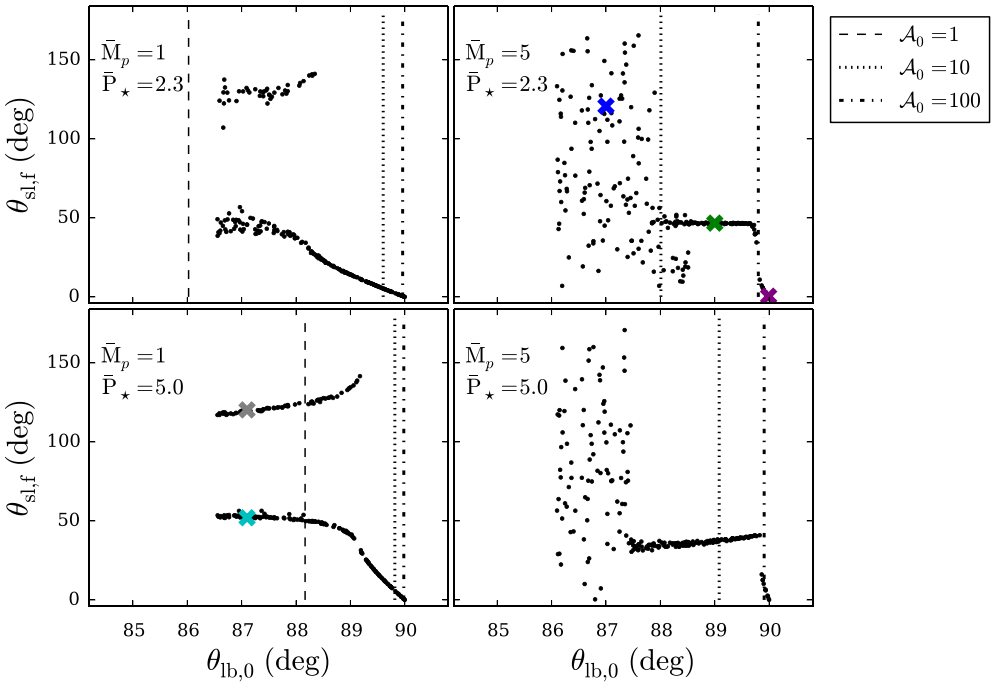

Figure 11. Final spin-orbit misalignments as a function of the initial inclination, for various combinations of planet mass and (constant) stellar spin period, as labelled. In this example, we neglect the feedback torque from the stellar quadrupole on the planetary orbit. We indicate various benchmark values of $\mathcal{A}_0$ by the vertical lines. The coloured crosses correspond to the time evolution presented in Fig. 10 (upper right panel), and Fig. 12 (lower left panel). Parameters are $a_0 = 1.5$ au, $a_{\rm b} = 300$ au, $e_{\rm b} = 0$.

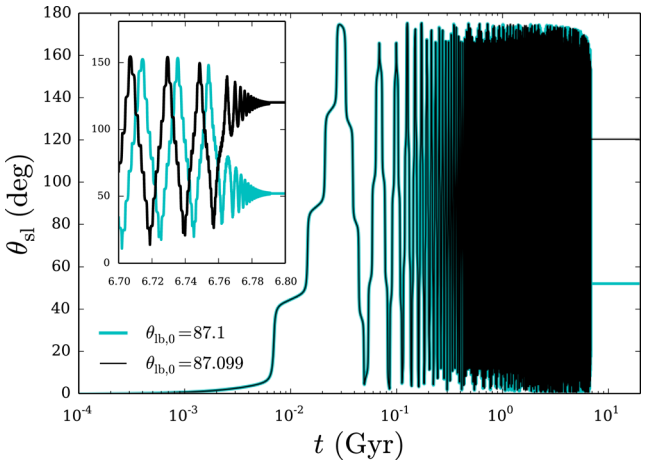

Figure 12. Time evolution for two systems with very similar initial inclinations, illustrating the bimodality in the final misalignment angle, as depicted in the lower left panel of Fig. 11. Parameters are $M_p = 1M_J$, $P_\star = 5$ d, $a_b = 300$ au, no feedback. Nearly identical initial inclinations accumulate some phase difference over the course of the evolution, which at the moment of transition to the adiabatic regime, give rise to different final angles, with $\theta_{lb,f} \approx 52^\circ$ and 120°.

the evolution of θ_{sl} (Storch et al. 2016, submitted). Stationary adiabatic behaviour manifests here as the 'tail' of the distributions at higher initial inclinations, e.g. between 88.5° and 90° in the top-left panel, and near 90° in the bottom-right panel. The long stretches of nearly constant $\theta_{sl,f}$ present in the higher mass (more adiabatic) panels are due to adiabatic advection.

The non-adiabatic behaviour regime shown in Fig. 8 (left-hand panels) manifests here as a bimodal split in $\theta_{sl,f}$ (see the left two panels of Fig. 11). This bimodality is the result of a bifurcation phenomenon that occurs at the moment the system transitions from being non-adiabatic to being adiabatic (due to the orbital decay from tidal dissipation). Before the transition, the system undergoes wide 0°–180° degree oscillations in θ_{sl}; after the transition, the system must evolve adiabatically and be confined either above or below $\theta_{sl} = 90^\circ$. The transition between these two states is akin to a bifurcation. We illustrate this in Fig. 12 by showing the time evolution of two trajectories with nearly identical initial conditions. Unlike the previous chaotic examples shown (with positive Lyapunov exponents) the trajectories in Fig. 12 do not quickly diverge, but rather remain qualitatively similar while accumulating some phase difference. This phase difference, if pronounced enough, leads to a bifurcation in the final spin-orbit angle. We discuss this phenomenon in detail in Storch et al. (2016, submitted).

In summary, the evolution of the spin-orbit misalignment angle can proceed in four distinct ways. (i) *Chaotic*. Neighbouring spin trajectories diverge exponentially and $\theta_{sl,f}$ is very sensitive to initial conditions. (ii) *Regular non-adiabatic*. θ_{sl} initially undergoes wide, regular 0°–180° oscillations. After significant semimajor axis decay has occurred, the evolution of θ_{sl} undergoes a bifurcation and becomes confined either above or below 90°. This leads to the bimodality seen in Fig. 11 (left-hand panels). (iii) *Stationary adiabatic*. θ_{sl} is approximately conserved and no misalignment can be generated. (iv) *Adiabatic advection*. The phase space trajectory becomes trapped in a resonance and advected to higher misalignments. $\theta_{sl,f}$ depends sensitively on the stellar spin period (Fig. 9, right-hand panel), but only weakly on the initial inclination (Fig. 11, right-hand panels).

4.3 Effects of the back-reaction torque from the stellar quadrupole on the orbit

All examples in Sections 4.1 and 4.2 have neglected the back-reaction torque from the stellar quadrupole on the planet's orbit, in order to simplify the analysis of the spin-orbit dynamics. However, under some conditions, the back-reaction torque can significantly affect the evolution of the spin-orbit misalignment. In the following discussion, we show how including this torque affects (and complicates) the dynamics, and delineate the parameter space where this torque can compete with the torque from the binary companion in changing the orbital axis.

The stellar quadrupole has two effects on the planetary orbit. First, it changes the direction of the angular momentum axis $\hat{\boldsymbol{L}}$ at the rate given by

$$\left.\frac{d\hat{\boldsymbol{L}}}{dt}\right|_{SL} = \Omega_{ps}\frac{S_\star}{L}\hat{\boldsymbol{S}}_\star \times \hat{\boldsymbol{L}} \propto M_\star^{-1/2} R_\star^5 \Omega_\star^2. \tag{60}$$

Secondly, it causes the eccentricity vector $\boldsymbol{e}$ to precess around $\hat{\boldsymbol{L}}$,

$$\left.\frac{d\boldsymbol{e}}{dt}\right|_{SL,rot} = \frac{\dot{\omega}_\star}{2}(5\cos^2\theta_{sl} - 1)\hat{\boldsymbol{L}} \times \boldsymbol{e} \tag{61}$$

where

$$\dot{\omega}_\star = -\frac{S_\star}{L}\frac{\Omega_{ps}}{\cos\theta_{sl}}. \tag{62}$$

The subscript 'rot' in equation (61) implies that the time derivative is done in the frame rotating with the nodal precession of the orbit (at the rate $\Omega_{ps}S_\star/L$), so that $\hat{\boldsymbol{L}}$ is fixed in space (compare equation 61 with equation A7). The effect of the stellar quadrupole on the eccentricity vector does not introduce any new features in the orbital evolution, but simply contributes to the rate of pericentre precession due to other SRFs (GR, tidal and rotational distortions of the planet). By contrast, the effect on the orbital axis $\hat{\boldsymbol{L}}$ does directly change θ_{lb}, thereby influencing the evolution of the spin-orbit angle.

Consider now the change in θ_{lb} due to the back-reaction torque of the stellar quadrupole (equation 60). The maximum possible change is

$$\begin{aligned}(\Delta\theta_{lb})_{max} &\sim \left(\frac{S_\star}{L}\right)_{e_{max}} \\ &\simeq 0.12\frac{\bar{k}_\star \bar{M}_{tot}^{1/2}\bar{R}_\star^2}{\bar{M}_p}\left(\frac{\bar{a}_F}{0.05}\right)^{-1/2}\left(\frac{P_\star}{30d}\right)^{-1},\end{aligned} \tag{63}$$

assuming $L \gtrsim S_\star$. The actual change of θ_{lb} in an LK cycle can be obtained by integrating equation (60) through time t_k around the eccentricity maximum, yielding

$$\begin{aligned}(\Delta\theta_{lb})_{actual} &\sim \left(\left|\frac{d\hat{\boldsymbol{L}}}{dt}\right|\Delta t\right)_{e_{max}} \\ &\sim \left(|\Omega_{ps}|\frac{S_\star}{L}\right)_{e_{max}} t_k\sqrt{1-e_{max}^2} \\ &\simeq 0.1\frac{\bar{k}_q \bar{R}_\star^5 \bar{M}_{tot}\bar{a}_{b,eff}^3}{\bar{M}_b \bar{M}_\star \bar{a}^{7/2}}\left(\frac{\bar{a}_F}{0.05}\right)^{-3/2}\left(\frac{P_\star}{6d}\right)^{-2}\end{aligned} \tag{64}$$

where we have used equation (31) for $\Delta t(e_{max})$. Note that $(\Delta\theta_{lb})_{actual}$ is also approximately equal to the ratio between $|d\hat{\boldsymbol{L}}/dt|_{SL}$ and $|d\hat{\boldsymbol{L}}/dt|_{LK}$. equation (64) assumes $\Delta\theta_{lb,actual} \lesssim \Delta\theta_{lb,max}$. That is, the actual change in θ_{lb} due to the back-reaction torque is given by equation (63) or equation (64), whichever is smaller.

We have already seen from Fig. 11 that the final spin-orbit misalignment can depend strongly on $\theta_{lb,0}$. We expect that the

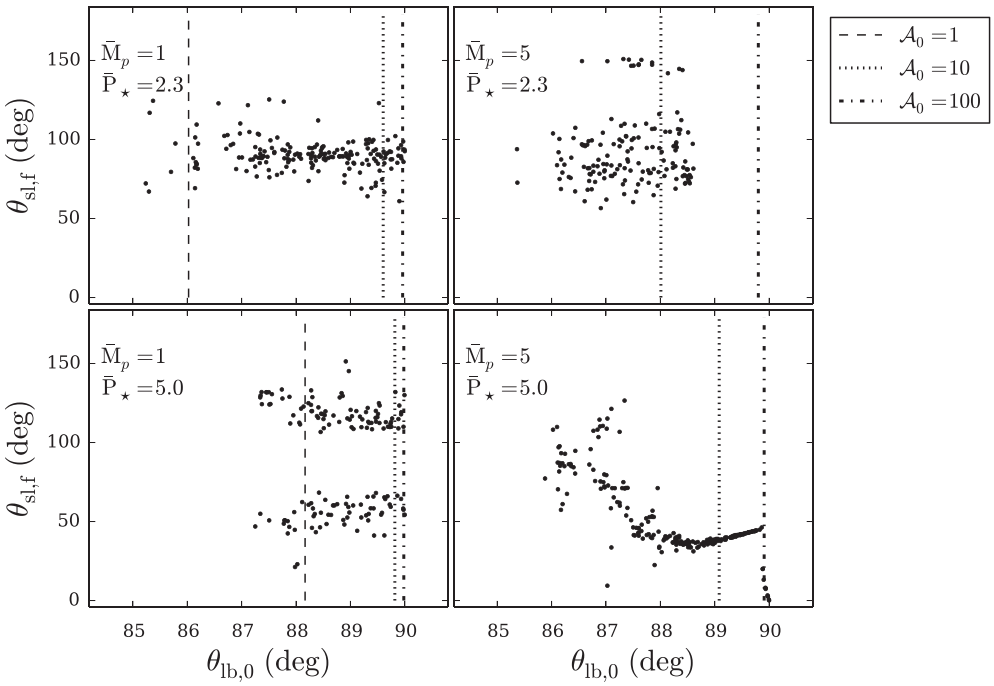

Figure 13. Same as Fig. 11, but including feedback from the stellar quadrupole on the orbit.

back-reaction torque will significantly affect $\theta_{\rm sl,f}$ when $(\Delta\theta_{\rm lb})_{\rm actual} \gtrsim 0.1$. Equations (63) and (64) indicate that this condition is satisfied for $P_\star \lesssim$ a few days, depending on various parameters (such as $a_{b,\rm eff}$ and $M_{\rm p}$). Fig. 13 shows $\theta_{\rm sl,f}$ as a function of $\theta_{\rm lb,\,0}$ for several values of $P_\star$ and $M_{\rm p}$, with the back-reaction torque included in the calculations (cf. Fig. 11, which neglects the back-reaction torque).

Comparing Figs 11 and 13 reveals the main effects of the back-reaction torque on the final spin-orbit angle. Systems with the lowest planet mass and shortest spin period ($M_{\rm p} = 1M_{\rm J}$, $P_\star = 2.3$ d, top left) are most strongly affected by feedback, and the clean bimodality present in $\theta_{\rm sl,f}$ in Fig. 11 is erased, and replaced by clustering near $\theta_{\rm sl,f} \sim 90^\circ$. The results for the large planet mass and short spin period ($M_{\rm p} = 5M_{\rm J}$, $P_\star = 2.3$ d, top right) are also significantly affected, due to planets becoming tidally disrupted at high inclinations. The systems with longer stellar spin periods (bottom panels) are less affected by feedback, and the general structure found in Fig. 11 is partially preserved.

5 POPULATION SYNTHESIS

5.1 Setup and computational procedure

In this section we perform a detailed parameter space survey for giant planets undergoing LK migration, exploring the dependence of the final spin-orbit misalignment angle distribution on the planet mass and stellar spin properties. We focus on two types of host stars: a solar-mass ($M_\star = 1\,{\rm M}_\odot$, spectral type G) star, and a massive ($M_\star = 1.4\,{\rm M}_\odot$, spectral type F) star. The initial spin period of both types of stars is set to $P_\star = 2.3$ d, corresponding to 5 per cent of breakup for the G star; both stars subsequently spin-down according to the Skumanich law (see Section 2.1). The G (F) star is calibrated to reach a spin period of 28 (9) d after 5 Gyr, to account for the fact that massive stars are observed to rotate more rapidly at a given age (e.g. McQuillan et al. 2014). The stellar radius is set to $R_\star = 1\,{\rm R}_\odot$ for G-type stars, and $R_\star = 1.26\,{\rm R}_\odot$ for F-type stars. We consider four planet masses ($M_{\rm p} = 0.3$, 1, 3 and $5M_{\rm J}$), all having a radius $R_{\rm p} = 1R_{\rm J}$. Note that this is a simplification, as some observed close-in gas giant planets are found to be inflated in size, while others are more compact (e.g. Laughlin, Crismani & Adams 2011).

We integrate the full equations of motion for the planetary orbit, including the octupole terms from the stellar companion, feedback torque from the host stellar spin, and all SRFs, together with evolution equations for the host stellar spin, and the planetary spin rate (due to tidal dissipation). As in previous population studies (Naoz et al. 2012; Petrovich 2015a), systems that do not obey the stability condition (Mardling & Aarseth 2001)

$$\frac{a_{\rm b}}{a} > 2.8\left(1+\frac{M_{\rm b}}{M_{\rm tot}}\right)^{2/5}\frac{(1+e_{\rm b})^{2/5}}{(1-e_{\rm b})^{6/5}}\left[1-0.3\frac{\theta_{\rm lb,0}}{180^\circ}\right] \quad (65)$$

are discarded. To increase the efficiency of the parameter survey, for each integration we adopt the following stopping conditions.

(i) If after 500 LK time-scales (equation 3) the pericentre distance has never reached $r_{\rm p} = a(1-e) < 0.07$ au, we terminate the calculation to avoid unnecessary integrations, and classify the planet as non-migrating. The time needed for such planets to undergo significant orbital decay is greater than $\sim 10^{11}$ yr (see Section 3.2, equation 32). This is far too long to allow significant migration within the lifetime of the host star.[3]

[3] Note that with the octupole terms from the binary companion included, the planet can achieve extreme values of eccentricity $e_{\rm lim}$ when $\theta_{\rm lb,\,0}$ is sufficiently large (see Section 3.4). Although these octupole extreme eccentricities are nearly always achieved sooner than $500t_k$ (depending on $\varepsilon_{\rm oct}$, see Liu et al. 2015), the possibility of the planet achieving such a high eccentricity cannot be ruled out for $t > 500t_k$. We therefore run the risk of terminating systems that might later undergo orbital decay. However, note that in such cases, the eccentricity usually becomes so high that the planet would be tidally disrupted, and removed from the sample of HJs. We have tested this stopping criterion and found that the approximation causes a very small

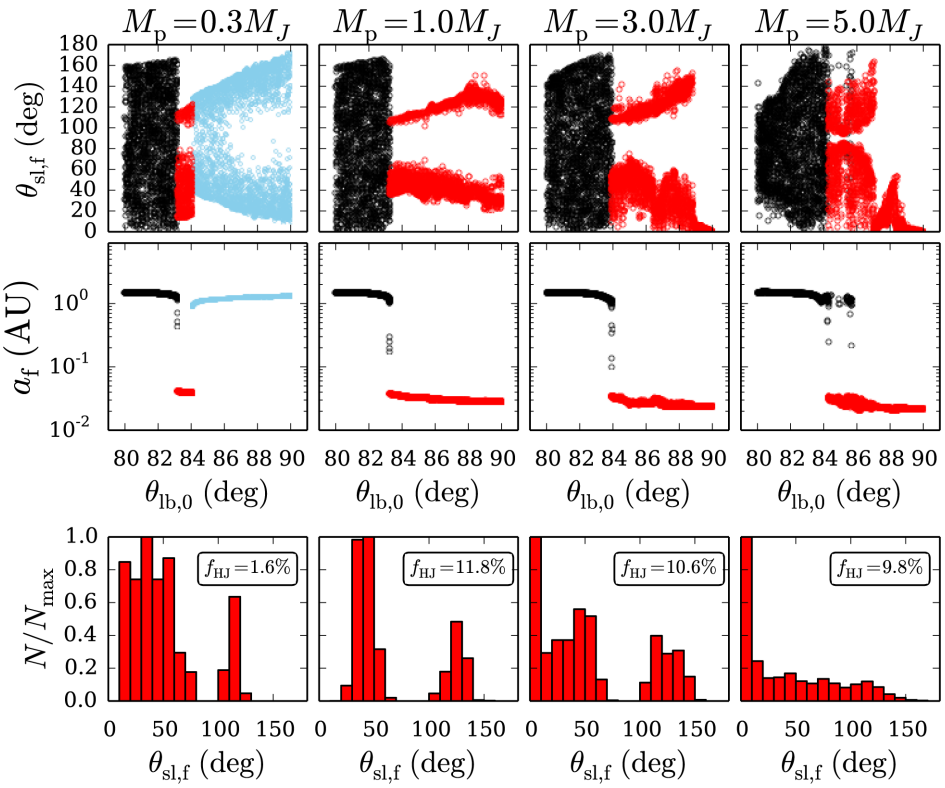

Figure 14. Final spin-orbit angle $\theta_{sl,f}$ (top panels) and semimajor axis a_f (middle panels) as a function of $\theta_{lb,0}$, for planet masses $M_p = 0.3$, 1, 3 and $5\,M_J$ (from left to right, as labelled). Bottom panels show distributions of the final spin-orbit misalignments for the systems that circularized (HJs). All systems have $M_\star = 1\,M_\odot$, $a = 1.5$ au, $a_b = 200$ au, $e_b = 0$. Black points: non-migrating planets. Blue points: tidally disrupted planets. Red points: HJs. Note that the values of $\theta_{sl,f}$ and a_f for the disrupted planets are simply the values at the time-step before tidal disruption is achieved, and thus have no particular observational significance. Tidal disruptions only occur here when $M_p = 0.3 M_J$, because the condition for disruption (Section 3.4, equation 49) is not satisfied for the other planet masses. See Table 2 for further information on the outcomes of the simulations. The distribution of $\theta_{sl,f}$ is distinctly bimodal for $M_p = 1 M_J$, with a preference for prograde orbits. As the planet mass increases, the adiabaticity parameter $\mathcal{A}_0$ increases (see Section 3), and for $M_p = 5 M_J$, the peak of the distribution occurs at low obliquities $\theta_{sl,f} = 0^\circ - 10^\circ$.

(ii) If at any point the pericentre distance $r_p = a(1-e) < r_{Tide}$, where r_{Tide} is the tidal disruption radius, given in equation (48), we terminate the integration, and classify the planet as tidally disrupted.

(iii) If the semimajor axis has decayed to $a < 0.1$ au, we terminate the integration and classify the planet as a HJ. In such cases, the spin-orbit angle has always safely reached the adiabatic regime (so that the adiabaticity parameter $\mathcal{A}$ has become sufficiently large), with $\hat{\boldsymbol{S}}_\star$ and $\hat{\boldsymbol{L}}$ undergoing mutual precession, and θ_{sl} is nearly constant, varying by less than 1°. At this point, LK oscillations from the binary companion are completely suppressed (see Section 3.1), and the planet will continue to undergo pure tidal evolution at nearly constant angular momentum, with final semimajor axis $a_f \simeq a(1-e^2)$, where a and e are evaluated at the point at which the integration is stopped.

(iv) If none of these conditions are satisfied during the integration, we terminate the integration at $t = 5$ Gyr and classify the planet as non-migrating.

For each set of system parameters, we begin by integrating the full equations of motion. However, in situations where the planet experiences sufficient orbital decay, the LK oscillations become suppressed so that the range of eccentricity variation narrows, and the stellar spin axis enters the adiabatic regime where $\theta_{sl} \approx$ constant (see Sections 3.1 and 3.5). In such cases, the eccentricity vector $\boldsymbol{e}$ precesses much more rapidly compared to the tidal decay rate. Resolving this rapid precession is computationally expensive, but does not influence the final result. Therefore, once the LK eccentricity oscillations and spin-orbit angle have both 'frozen' we stop following the eccentricity precession (i.e. by neglecting the SRF and LK terms in the planet's equations of motion), and allow the orbit to evolve purely under tidal dissipation.[4]

We assume that the initial planet orbital axis $\hat{\boldsymbol{L}}$ is isotropically distributed with respect to $\hat{\boldsymbol{L}}_b$. In principle, the initial inclination should be sampled over the entire range ($\theta_{lb,0} = [0^\circ, 90^\circ]$).[5] In practice however, we explore a limited range of $\theta_{lb,0}$ to avoid unnecessary computation for planets that have no chance of migrating.

fraction of tidally disrupted planets to be misclassified as non-migrating, but the fraction of HJs is unaffected.

[4] In practice, we consider the e-oscillations to have frozen when $\varepsilon_{GR} > 30$, and θ_{sl} to have settled to its final value when the adiabaticity parameter satisfies $\mathcal{A}_0 \sin 2\theta_{lb} > 5$ (see Sections 3.1 and 3.5). We have tested both conditions extensively and find they are extremely conservative estimates, so that the LK oscillations and variation in θ_{sl} are always safely quenched at the point when the SRF and LK terms are neglected in the equations of motion.

[5] Since $M_p \ll M_\star, M_b$, the triple systems considered here exhibit symmetry around $\theta_{lb,0} = 90^\circ$, so that $90^\circ \le \theta_{lb,0} \le 180^\circ$ need not be considered (e.g. Liu et al. 2015).

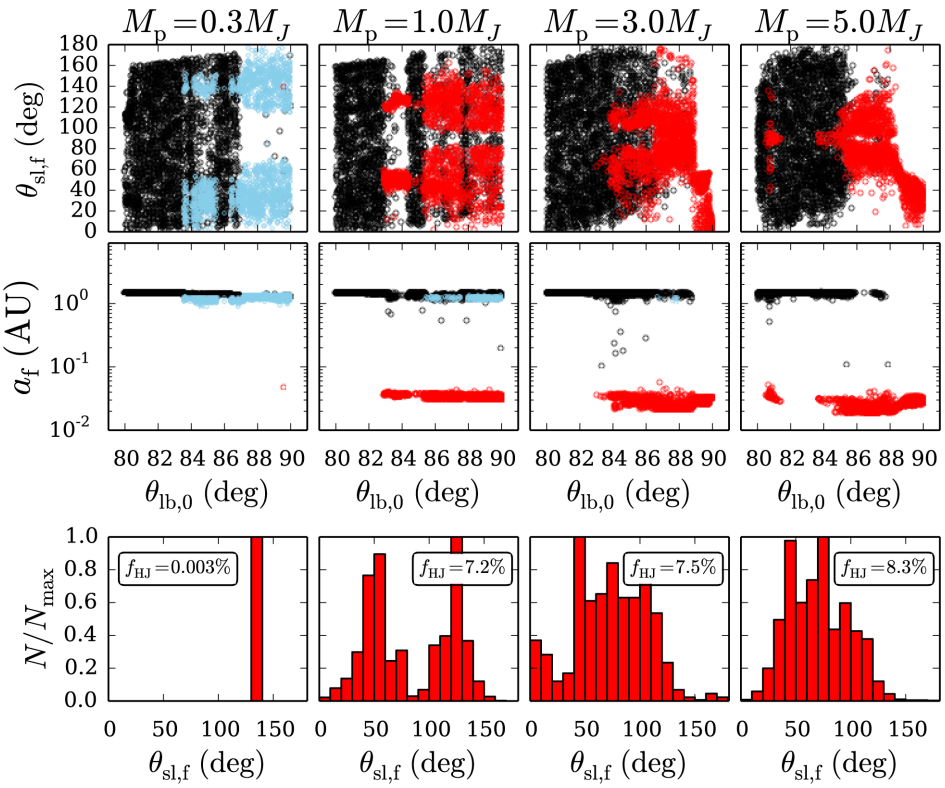

Figure 15. Same as Fig. 14, except for an F-type host star, with $M_\star = 1.4\,M_\odot$, $R_\star = 1.26\,R_\odot$ and corresponding spin properties (see text). Note that the histogram for $M_p = 0.3M_J$ has only one data point. When $M_p = 1M_J$, the distributions of $\theta_{sl,f}$ are similar to those for the G star, but are broadened. When $M_p = 5M_J$, however, the strong peak near low obliquities ($\theta_{sl,f} = 0°-10°$) observed for planets around G stars has vanished. We attribute these differences to the increased torque from the stellar quadrupole on the planetary orbit, as well as stronger periastron precession from SRFs.

Note that systems with inclinations $\theta_{lb,0} \lesssim 40°$ (the critical 'Kozai angle') can be safely excluded, because they do not undergo large excursions in eccentricity. We find empirically that systems with $\theta_{lb,0} \lesssim 65°$ rarely reach sufficiently high eccentricities to induce tidal migration. In the rare cases where migration occurs, the system always results in tidal disruption, rather than HJ formation. We therefore restrict the inclination to lie in the range $65° \leq \theta_{lb,0} \leq 90°$.

Of primary interest in this paper is the fraction of total systems that result in the production of an HJ or tidal disruption, for fixed planet mass and stellar type, and considering the full possible ranges of ($\theta_{lb,0}$, a, a_b, e_b). For a given combination of host star properties and planet mass, we run N_{run} trials (typically ∼9000) by repeatedly sampling the inclination randomly from the restricted range ($65° \leq \theta_{lb,0} \leq 90°$).[6] The fractions of HJ formation and tidal disruption can be obtained from $f_{HJ} = \cos 65° N_{HJ}/N_{run}$ and $f_{dis} = \cos 65° N_{dis}/N_{run}$, where N_{HJ} and N_{dis} are the number of systems among N_{run} runs that resulted in HJs and tidal disruptions.

The ultimate goals of this section are to present distributions of final stellar spin-orbit angles, and obtain the fractions of total systems that result in HJs and disruptions for a given planet mass and stellar type, sampling over the entire possible ranges of a, a_b, e_b. However, we begin by fixing $e_b = 0$, thereby eliminating complications introduced by octupole terms. Section 5.2 shows results for fixed binary separation a_b and planet semimajor axis a, in order to isolate and highlight the effects of changing the planet mass and stellar mass/spin properties. Next, Section 5.3 presents results for non-zero binary eccentricity (with fixed a_b and a), thus showing how the octupole term in the disturbing potential of the binary companion can affect the results. Finally, in Section 5.4, we randomly sample over a wide range in (a, a_b, e_b) parameter space, and present results appropriate for comparison with the observational sample of close-in giant planets.

[6] The only exception is in Section 5.2, where we explore initial inclinations in the range $80° \leq \theta_{lb,0} \leq 90°$, since the parameters considered there never produce migrating planets when $\theta_{lb,0} \lesssim 80°$.

5.2 Quadrupole results

To start, we fix the initial planet semimajor axis $a_0 = 1.5$ au, binary separation $a_b = 200$ au and binary eccentricity $e_b = 0$ (so that the octupole contributions vanish). We consider planet masses $M_p = 0.3$, 1.0, 3.0 and $5.0M_J$, and run a fine grid of initial inclinations, selected randomly from an isotropic distribution (uniform in $\cos\theta_{lb,0}$). The argument of pericentre ω and orbital node Ω are randomly sampled uniformly in $[0, 2\pi]$. The results are shown in Figs 14 (G star) and 15 (F star), where we plot the final spin-orbit angle $\theta_{sl,f}$ and semimajor axis a_f versus the initial inclination $\theta_{lb,0}$, as well as the distributions of $\theta_{sl,f}$ for the systems that resulted in HJs (with final semimajor axis $a_f < 0.1$ au).

5.2.1 G star

The dynamics considered in this section are considerably more complicated than the idealized analysis presented in Section 4, since the effects of stellar spin-down ($S_\star \neq$ constant) and the back-reaction torque from the oblate host star on the planetary orbit are now

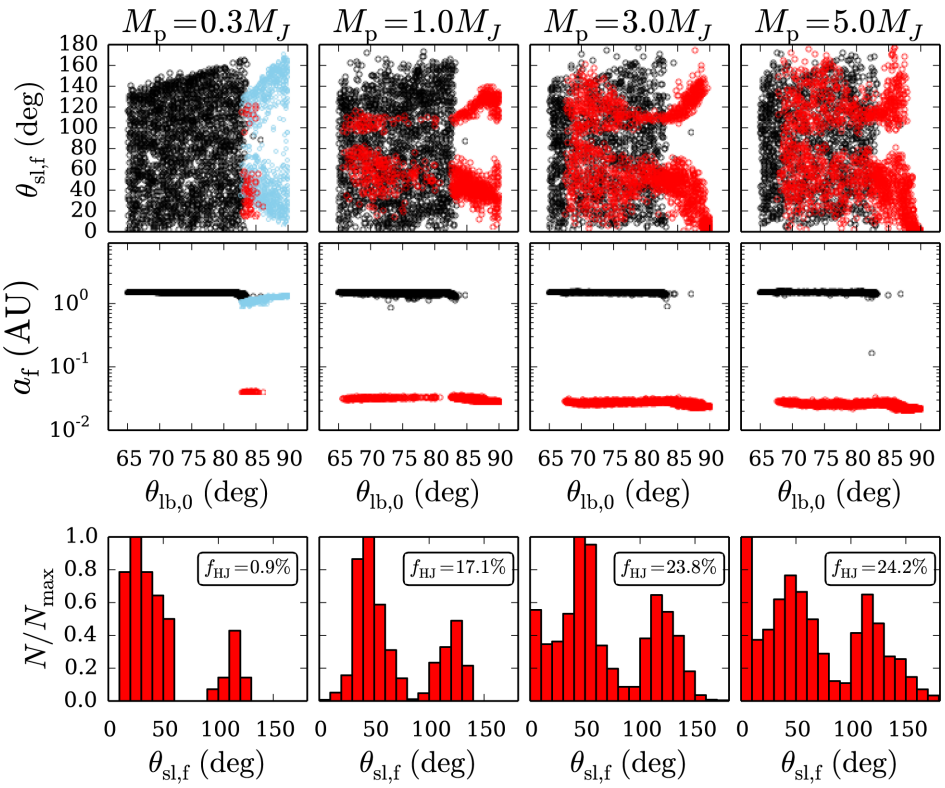

Figure 16. Same as Fig. 14, except that $e_b = 0.8$, and $a_b = 333.33$ au (so that $a_{b,eff} = 200$ au and $\varepsilon_{oct} \approx 0.01$). For $M_p = 0.3 M_J$, the results are nearly unchanged (compared to Fig. 14), because pericentre precession from SRFs is higher for low-mass planets (see text), and the effects of the octupole (e.g. extreme high eccentricities) are more easily suppressed. For $M_p \geq 1 M_J$, the HJ production fraction is increased. In terms of $\theta_{sl,f}$, the main effect of the octupole is to add HJs with a primarily bimodal distribution, thereby increasing the fraction of significantly misaligned planets.

Table 2. Input parameters and results of the calculations presented in Sections 5.2 and 5.3. Each line is the result of N_{run} trials with initial inclination $\theta_{lb,0}$ randomly sampled from an isotropic distribution in the range 65°–90° (the only exception are the first eight rows, with $e_b = 0$, where $\theta_{lb,0}$ is sampled in $80° - 90°$). Each set of trials has a fixed a_b and e_b, as indicated, and $a_0 = 1.5$ au, and tidal enhancement factor $\chi = 10$. The initial spin-orbit angle is set to $\theta_{lb,0} = 0°$. We display the 'migration fraction ' $f_{mig} \equiv f_{HJ} + f_{dis}$, as well as the 'prograde fraction' f_{prog} i.e. the fraction of HJ systems with final obliquities $\theta_{sl,f} < 90°$. We also include relevant figure numbers in the rightmost column. Note that the stellar radius is set to $R_\star = 1$ R$_\odot$ when $M_\star = 1$ M$_\odot$, and $R_\star = 1.26$ R$_\odot$ when $M_\star = 1.4$ M$_\odot$.

$M_\star$ (M$_\odot$)	M_p (M_J)	a_b (au)	e_b	N_{run}	f_{HJ} (per cent)	f_{dis} (per cent)	f_{mig} (per cent)	f_{prog} per cent	Figure
Section 5.2									
1.0	0.3	200.0	0.0	5000	1.6	10.3	12.0	84.3	14, 17
1.0	1.0	200.0	0.0	5000	11.8	0.0	11.8	71.2	14, 17
1.0	3.0	200.0	0.0	5000	10.6	0.0	10.6	72.0	14, 17
1.0	5.0	200.0	0.0	5000	9.8	0.0	9.8	82.6	14
1.4	0.3	200.0	0.0	5000	0.003	7.8	7.8	0.0	15
1.4	1.0	200.0	0.0	5000	7.2	0.9	8.2	54.5	15
1.4	3.0	200.0	0.0	5000	7.5	0.0	7.5	66.8	15
1.4	5.0	200.0	0.0	5000	8.3	0.0	8.3	74.0	15
Section 5.3									
1.0	0.3	218.22	0.4	3000	1.3	10.8	12.2	89.5	17
1.0	1.0	218.22	0.4	3000	12.2	0.0	12.2	68.1	17
1.0	3.0	218.22	0.4	3000	12.4	0.0	12.4	73.4	17
1.0	5.0	218.22	0.4	3000	12.9	0.0	12.9	78.6	17
1.0	0.3	333.33	0.8	3000	0.9	11.4	12.3	82.5	16, 17
1.0	1.0	333.33	0.8	3000	17.1	0.0	17.1	70.4	16, 17
1.0	3.0	333.33	0.8	3000	23.8	0.0	23.8	65.7	16, 17
1.0	5.0	333.33	0.8	3000	24.2	0.0	24.2	66.3	16, 17

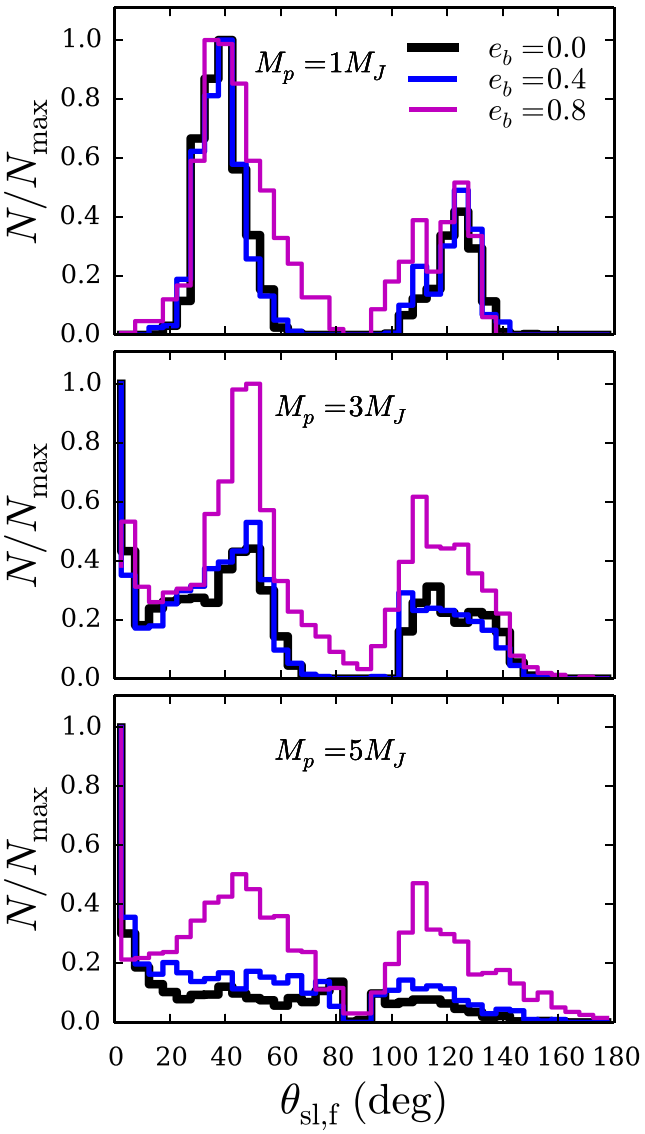

Figure 17. Distributions of $\theta_{\rm sl,f}$ for various binary eccentricities, $e_{\rm b} = 0, 0.4, 0.8$, as labelled, and showing planet masses $M_{\rm p} = 1, 3, 5M_{\rm J}$ (from top to bottom). Binary separations have been chosen such that $a_{b,\rm eff} = a_{\rm b}\sqrt{1-e_{\rm b}^2} = 200$ au. As a result, the quadrupole LK time-scale t_k is identical, so that the results depicted in each panel would be identical to quadrupole order. This illustrates the role of the octupole in generating spin-orbit misalignment.

included. None the less, many of the general features remain for the G star (Fig. 14). The distribution of $\theta_{\rm sl,f}$ for planets with mass $M_{\rm p} = 1M_{\rm J}$ is distinctly bimodal with peaks at $\theta_{\rm sl,f} \sim 40^\circ$ and 120° (compare with Figs 11 and 13 in Section 4). As $M_{\rm p}$ increases, the systems with larger initial inclinations ($\theta_{\rm lb,\,0}$) show a preference for alignment due to their higher adiabaticity parameters, with $\mathcal{A}_0 \propto M_{\rm p}/\cos\theta_{\rm lb,0}$ (see equation 11). The largest mass planets ($M_{\rm p} = 5M_{\rm J}$) tend to settle into low obliquity states ($\theta_{\rm sl,f} \lesssim 10^\circ$), although high misalignments still remain possible. Note that the cases with $M_{\rm p} = 5M_{\rm J}$ and $\theta_{\rm lb,\,0} \sim 88^\circ$ (in the top, rightmost plot in Fig. 14) have undergone adiabatic advection (see Section 4).

For the lowest mass planets ($M_{\rm p} = 0.3M_{\rm J}$), most systems result either in non-migrating planets or tidal disruptions, with very few 'hot Saturns' produced. Tidal disruptions for low-mass planets are more common because of the larger tidal disruption radius (see equation 48). When $M_{\rm p} = 0.3M_{\rm J}$, $r_{\rm Tide} \approx 4\,{\rm R}_\odot$, whereas when $M_{\rm p} = 5M_{\rm J}$, $r_{\rm Tide} \approx 1.6\,{\rm R}_\odot$. As a result, with $M_{\rm p} = 0.3M_{\rm J}$ and the fixed values of $(a, a_{\rm b}, e_{\rm b})$ that we consider in this subsection, there is only a very narrow range of initial inclinations that lead to pericentre distances that are small enough to induce orbital decay, but large enough to prevent tidal disruption (see Fig. 14, left-hand panels). For $a_0 = 1.5$ au, $a_{\rm b} = 200$ au and $e_{\rm b} = 0$, systems with $M_{\rm p} \geq 1M_{\rm J}$ never result in tidal disruptions, because the condition for disruption to be possible, derived in Section 3.4 (see Fig. 6 and equation 49) is never satisfied. However, note that these results depend on the assumed tidal disruption radius (equation 48). The exact tidal radius is somewhat uncertain, and depends on the assumed planetary mass–radius relation, which can vary for close-in giant planets.

5.2.2 *F star*

The results of identical calculations for the F star are shown in Fig. 15. The HJ fractions are consistently lower compared to the G star, for all planet masses, but most noticeably for $M_{\rm p} = 0.3M_{\rm J}$, with only a single HJ produced in ∼5000 trials. For planet mass $M_{\rm p} = 1M_{\rm J}$, the distribution of $\theta_{\rm sl,f}$ remains bimodal, but with larger spread. For $M_{\rm p} = 5M_{\rm J}$, the distributions of $\theta_{\rm sl,f}$ are strikingly different between the F and G stars. The peak of the distribution occurs at $\theta_{\rm sl,f} \approx 70^\circ - 80^\circ$, i.e. producing many HJs in near polar orbits with respect to the stellar spin axis. This contrasts strongly with results for the G star, where the peak occurs at $\theta_{\rm sl,f} = 0^\circ - 10^\circ$. These differences between the G star (Fig. 14) and F star (Fig. 15) arise for two reasons. First, the larger stellar mass and radius affect the net rate of pericentre precession from SRFs, $\dot{\omega}$. The contributions to $\dot{\omega}$ from general relativity and the planetary tidal deformation are higher for more massive stars, which lead to a lower maximum achievable eccentricity and tend to reduce HJ production fractions (however, note that the contribution to $\dot{\omega}$ from the oblate host star has the opposite sign, and can, under come circumstances, cancel the increases in $\dot{\omega}$ from GR and tidal distortion). Secondly, the larger stellar radius and spin frequency (compared to the G star) both lead to a more pronounced torque on the planetary orbit from the stellar quadrupole, since $(d\boldsymbol{L}/dt)_{\rm SL} \propto R_\star^5\Omega_\star^2$; see Section 4.3, equation 60). The increased stellar radius alone leads to an increase in the back-reaction torque of the stellar quadrupole on the orbit by a factor of ∼3, with a further increase due to higher $\Omega_\star$.

Both the wider spread in the bimodal distributions (when $M_{\rm p} = 1M_{\rm J}$), and peak near $\theta_{\rm sl,f} \sim 90^\circ$ (when $M_{\rm p} = 5M_{\rm J}$) can be understood from the results of Section 4, where we presented final spin-orbit angles for varying initial inclinations, both with and without feedback included. Comparing the lower left panels of Figs 11 and 13 shows that in some cases, including feedback causes the bimodality to be partially preserved, but with significant broadening. Similarly, comparing the upper left panels of Figs 11 and 13 shows that in other cases, including feedback completely erases the bimodality, causing $\theta_{\rm sl,f}$ to instead cluster around ∼90°. Thus, we attribute the qualitative differences in $\theta_{\rm sl,f}$ between the G and F star to enhanced feedback from the oblate F star on the orbit.

5.3 Octupole results: fixed binary eccentricity and separation

Having demonstrated results for binary companions with zero eccentricity, we now consider binaries with non-zero eccentricity, so that the octupole terms can contribute to the dynamics. We limit the discussion in this section to the solar-type (G) star, and present one example of fixed non-zero binary eccentricity (see Section 5.4 for

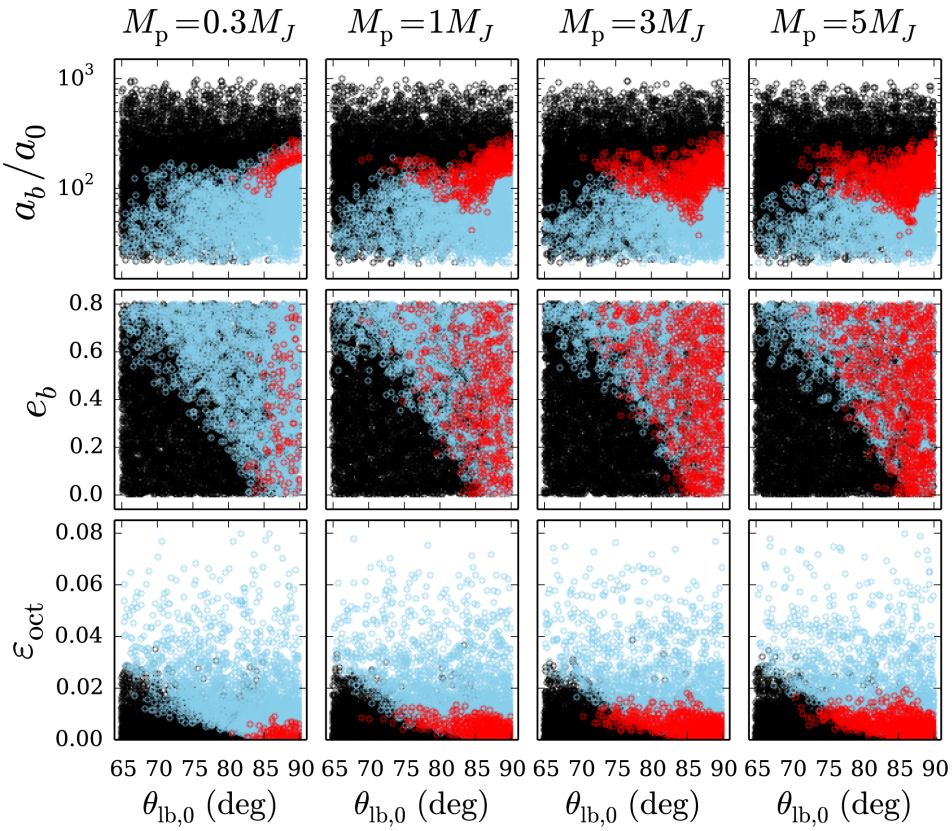

Figure 18. Parameter space producing HJs (red), tidally disrupted planets (blue), and non-migrating planets (black), around G stars. Top panels: initial binary separation ratio (a_b/a_0) versus the initial inclination $\theta_{lb,0}$. Middle panels: binary eccentricity e_b. Bottom panels: 'octupole strength' ε_{oct}. Results are separated into columns by planet mass, as labelled. HJs are able to be produced over the full range of $e_b = [0, 0.8]$, but only in a relatively narrow range of a_b/a_0. As a result, the range of ε_{oct} capable of producing HJs is limited, with $\varepsilon_{oct} \lesssim 0.01 - 0.02$.

general combinations of a_b and e_b). For a straightforward comparison with the results from Section 5.2, and to illustrate the role of the octupole, we choose the parameters so that the quadrupole LK time-scale t_k (equation 3) is unchanged (since t_k depends only on the combination $a_{b,\rm eff} = a_b\sqrt{1-e_b^2}$). We thus specify the binary eccentricity e_b and choose the separation a_b such that the quantity $a_{b,\rm eff} = 200$ au. Fig. 16 shows results for $e_b = 0.8$, $a_b = 333$ au, corresponding to $\varepsilon_{oct} \approx 0.01$. Additional results with $e_b = 0.4$, $a_b = 218$ au, so that $\varepsilon_{oct} \approx 0.003$ are included in Table 2. Recall that ε_{oct} quantifies the 'strength' of the octupole potential; see equation (4).

Without the octupole terms, the limiting eccentricity e_{lim} during an LK cycle is achieved at $\theta_{lb,0} = 90^\circ$. One effect of the octupole term is to allow this limiting eccentricity to be realized at $\theta_{lb,0} < 90^\circ$ (Liu et al. 2015), so that migration becomes possible for a wider range of inclinations, thereby increasing the production efficiency (Naoz et al. 2012).

Comparing Figs 14 and 16 allows the role of the octupole terms to be identified, since they would produce identical results to quadrupole order. Low-mass planets are affected by the octupole potential less than high-mass planets, because the rate of pericentre precession due to tidal distortion of the planet has the dependence $\dot{\omega}_{\rm Tide} \propto M_p^{-1}$ (see equation A11). This precession can act to suppress the extreme octupole dynamics, such as increased eccentricities and orbit flipping. Thus for the lowest mass planets ($0.3M_J$) the results do not differ significantly from the pure quadrupole case. More massive planets ($M_p = 1$–$5M_J$) are affected more strongly, with the production fraction of HJs increasing with the octupole strength ε_{oct} (see Section 5.4.1 for further discussion of HJ and disruption fractions).

In terms of the final obliquity $\theta_{sl,f}$, one effect of the octupole is to increase the number of significantly misaligned $5M_J$ planets, as demonstrated in Fig. 17. There are two possible reasons for this. First, the octupole allows close-in planets to be produced at lower inclinations, with lower adiabaticity parameters ($\mathcal{A}_0 \propto 1/\cos\theta_{lb,0}$). Since the degree of misalignment depends on $\mathcal{A}_0$, systems with low inclinations have a tendency to settle to larger obliquities, and exhibit bimodality. Secondly, the chaos induced in the orbit due to the octupole terms may act to disrupt the tendency for alignment found for the pure quadrupole calculations. Despite these effects, for $5M_J$ planets with the octupole included, the strong peak near zero obliquity observed for the pure quadrupole results ($e_b = 0$, Fig. 14) is partially preserved.

5.4 General results for a range of binary separations, eccentricities and planet semimajor axes

We now survey the parameter space in (a_0, a_b, e_b), sampling the initial planet semimajor axis a_0 uniformly in the range $a_0 = 1$–5 au, the binary separation $a_b = 100$–1000 au (uniform in $\log a_b$), and the binary eccentricity uniformly in $e_b = 0$–0.8. This choice of eccentricity distribution is highly approximate, as the actual eccentricity distribution of wide binaries is uncertain (see Tokovinin & Kiyaeva 2015). Moreover, planet formation at a few au may be quenched by the presence of a highly eccentric binary companion (when $a_b(1-e_b)$ is not sufficiently larger than a_0). As in previous

Table 3. Same format as Table 2, but showing results for the full population synthesis calculations in Sections 5.4–5.6. We vary a_0, a_b and e_b uniformly in the ranges $a_0 = (1–5)$ au, $a_b = (100–1000)$ au (note that a_b is sampled uniformly in $\log a_b$), and $e_b = (0–0.8)$. $\theta_{lb,0}$ is sampled isotropically in the range 65°–90°. The other parameters and notation are the same as in Table 2.

$M_\star$ ($M_\odot$)	M_p (M_J)	$\theta_{sl,0}$ (◯)	χ	N_{run}	f_{HJ} (per cent)	f_{dis} (per cent)	f_{mig} (per cent)	f_{prog} per cent	Figure
Section 5.4									
1.0	0.3	0.0	10.0	8988	0.5	12.3	12.8	70.4	18, 20
1.0	1.0	0.0	10.0	8991	2.4	11.0	13.4	78.3	18, 20
1.0	3.0	0.0	10.0	8996	3.8	9.3	13.1	72.0	18, 20
1.0	5.0	0.0	10.0	8994	4.7	8.4	13.0	74.1	18, 20
1.4	0.3	0.0	10.0	8993	0.0	12.3	12.3	100.0	21
1.4	1.0	0.0	10.0	8994	1.4	10.9	12.3	64.9	21
1.4	3.0	0.0	10.0	8998	3.0	9.8	12.8	67.7	21
1.4	5.0	0.0	10.0	8997	3.6	9.1	12.6	69.4	21
Section 5.5									
1.0	0.3	0.0	1.0	8998	0.0	11.8	11.8	0.0	23, 24
1.0	1.0	0.0	1.0	8991	0.7	11.1	11.8	75.6	23, 24
1.0	3.0	0.0	1.0	8997	2.3	9.6	11.9	69.6	23, 24
1.0	5.0	0.0	1.0	8993	3.1	9.5	12.5	70.9	23, 24
1.4	0.3	0.0	1.0	8997	0.0	10.9	10.9	0.0	25
1.4	1.0	0.0	1.0	8995	0.4	10.6	10.9	52.0	25
1.4	3.0	0.0	1.0	8996	1.5	10.4	11.8	58.1	25
1.4	5.0	0.0	1.0	8998	1.9	9.9	11.8	61.9	25
1.0	0.3	0.0	100.0	8995	2.4	11.6	14.0	61.6	23, 24
1.0	1.0	0.0	100.0	8997	4.1	9.7	13.8	68.7	23, 24
1.0	3.0	0.0	100.0	8994	6.4	5.9	12.4	71.8	23, 24
1.0	5.0	0.0	100.0	8994	7.8	4.1	12.0	71.0	23, 24
1.4	0.3	0.0	100.0	8997	1.5	11.7	13.2	65.5	25
1.4	1.0	0.0	100.0	8996	3.3	9.9	13.2	65.0	25
1.4	3.0	0.0	100.0	8994	6.3	6.2	12.5	66.3	25
1.4	5.0	0.0	100.0	8999	7.6	4.1	11.6	66.7	25
Section 5.6									
1.0	0.3	30.0	10.0	8995	0.3	12.8	13.1	67.2	26
1.0	1.0	30.0	10.0	8996	2.6	10.6	13.1	62.1	26
1.0	3.0	30.0	10.0	8986	4.0	9.5	13.5	61.1	26
1.0	5.0	30.0	10.0	8995	4.8	8.8	13.6	70.6	26
1.0	0.3	60.0	10.0	8993	0.4	12.8	13.2	52.4	26
1.0	1.0	60.0	10.0	8995	2.6	11.2	13.8	47.5	26
1.0	3.0	60.0	10.0	8993	4.4	10.0	14.5	49.3	26
1.0	5.0	60.0	10.0	8993	4.9	9.4	14.3	54.5	26

subsections, the initial inclination $\theta_{lb,0}$ is sampled isotropically in the range 65°–90°. We fix the tidal enhancement factor at $\chi = 10$ in this section; we explore the effects of varying χ in Section 5.5.

5.4.1 HJ and disruption fractions

Fig. 18 depicts the outcomes of our simulations for planets around G stars, where we plot the initial semimajor axis ratio a_b/a_0 and binary eccentricity e_b versus the initial inclination $\theta_{lb,0}$. The final outcome of each integration is indicated by the colour (HJ, disrupted planet, or non-migrating). Results for planets around F stars are qualitatively similar, and are omitted. See Table 3 for further information, including the HJ and disruption fractions.

Fig. 18 shows that HJs are produced for a relatively narrow range of the ratio a_b/a_0. Planets with $a_b/a_0 \lesssim 60$ are always either tidally disrupted or non-migrating, while those with $a_b/a_0 \gtrsim 300$ never undergo migration. This result places constraints on the requirements for stellar companions to induce migration without destroying the planet (see also Section 3.4 for a discussion of the conditions that must be satisfied for migration and tidal disruption). In the bottom panels of Fig. 18, we plot the values of ε_{oct} versus $\theta_{lb,0}$. We find that systems with $\varepsilon_{oct} \gtrsim 0.03$ always lead to tidal disruptions, and that no HJs are produced for $\varepsilon_{oct} \gtrsim 0.01 - 0.02$. This finding can be understood by examining Fig. 19, where we plot the initial conditions in terms of $(a_{b,eff}, a_0)$ for the $1M_J$ planets that resulted in tidal disruptions and HJs, along with the criteria for migration (disruption) to occur, shown as solid red (blue) curves (see also Fig. 6). We see that the migration/disruption conditions derived in Section 3.4 are in good agreement with our numerical calculations.

Also plotted in Fig. 19 are curves of constant $\varepsilon_{oct} = 0.015$ (dashed black curves, with $e_b = 0.4$, 0.6, 0.8, from bottom to top). The uppermost dashed line, with $e_b = 0.8$, nearly coincides with the tidal disruption boundary, so that $\varepsilon_{oct} \gtrsim 0.015$ can only be achieved for combinations of $(a_{b,eff}, a_0)$ that are located in the 'disruption zone' i.e. below the solid blue curve, where systems are likely to result in tidal disruption, rather than HJs. Since we consider a range of binary eccentricities uniform in $e_b = [0, 0.8]$, all of our systems with $\varepsilon_{oct} \gtrsim 0.015$ reside in the disruption zone, thereby explaining the lack of circularized planets in our calculations with $\varepsilon_{oct} \gtrsim 0.015$.

Planets with mass $M_p = 1–3M_J$ around G stars have HJ production fractions f_{HJ} in the range 2.4–3.8 per cent, and f_{HJ} for planets around F stars is somewhat lower (1.4–3 per cent). For both stellar types, the fraction of HJs produced increases with

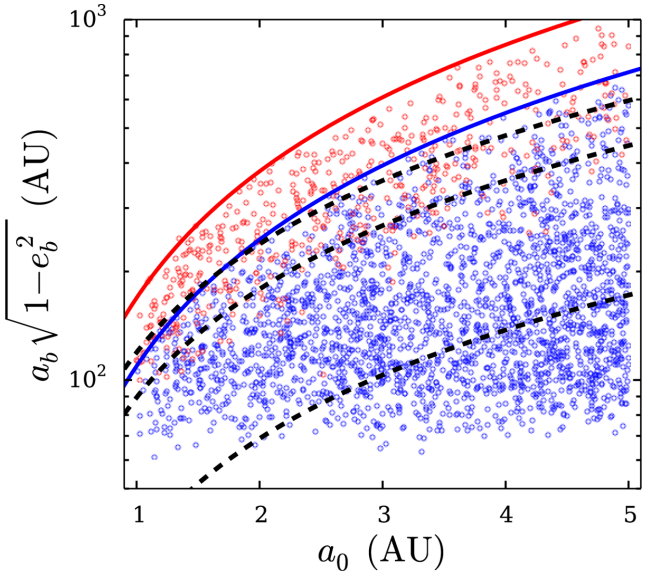

Figure 19. Parameter space producing tidally disrupted planets (blue points) and HJs (red points) for the calculations presented in Fig. 18 with $M_p = 1M_J$. The red solid curve shows the maximum value of $a_{b,eff} = a_b\sqrt{1-e_b^2}$ for migration to be possible, as a function of a_0 (equation 47 with $a_{p,crit} = 0.025$ au), and the blue solid curve shows the maximum value of $a_{b,\,eff}$ for tidal disruption to be possible (equation 49, with $f = 1$). If a given combination of (a_0, $a_{b,\,eff}$) is located below the red (blue) curve, migration (disruption) is possible, but not guaranteed. See also Fig. 6. The dashed lines depict curves of constant $\varepsilon_{oct} = 0.015$ in ($a_{b,\,eff}$, a_0) space, with $e_b = 0.8$, 0.6 and 0.4 (from top to bottom). The region above the top black dashed curve cannot have $\varepsilon_{oct} > 0.015$, unless $e_b > 0.8$. Since the location of this black curve coincides with the tidal disruption limit (blue curve), there is very little parameter space with $\varepsilon_{oct} > 0.015$ capable of inducing planet migration, without tidal disruption.

planet mass (see also Table 3, and the discussion in Section 5.3). This arises from our tidal disruption criterion (equation 48), with $r_{Tide} \approx 4\,R_\odot$ for the sub-Jupiter mass planet ($M_p = 0.3M_J$), and $r_{Tide} \approx 1.6\,R_\odot$ for $M_p = 5M_J$. Low-mass planets are therefore much more susceptible to tidal disruption, and are more readily removed from the sample of surviving planets. We find that the fraction of 'hot Saturns' ($M_p = 0.3M_J$) produced is especially low, with $f_{HJ}(0.3M_J) \approx 0.5$ per cent and 0.02 per cent for the G and F stars, respectively.

Comparing the results of Sections 5.2 and 5.3 (see Table 2), and this subsection (Table 3), we see that although certain combinations of (a_0, a_b, e_b) can lead to HJ fractions of $f_{HJ} \sim 24$ per cent (specifically when the octupole effect is included; see also Naoz et al. 2012), when ranges of (a_0, a_b, e_b) are considered, the overall HJ fraction is always less than a few per cent for planets with mass $M_p = 1M_J$.

Inspection of Table 3 reveals that the 'migration fraction' $f_{mig} \equiv f_{HJ} + f_{dis} \approx 12$–13 per cent is nearly constant for all planet masses and stellar types, varying by only $\sim$1 per cent. Given the complicated interplay between the various ingredients in our system (SRFs, octupole-level dynamics, tidal dissipation), and the dependence of these physical processes on planet and stellar mass, this result is not necessarily expected, but can be qualitatively understood from the discussion in Section 3.4. To achieve planet migration (either HJ formation or tidal disruption) within the lifetime of the host star, two conditions must be satisfied. (i) The planet must attain a sufficiently large eccentricity ($\sim e_{lim}$) so that the corresponding periastron distance $a(1 - e_{lim})$ is less than a critical value ($\simeq$0.025 au). This translates into a necessary condition for migration as given by equation (47). (ii) For systems that satisfy this condition, whether or not migration actually occurs depends on the initial inclination $\theta_{lb,\,0}$. As discussed in Section 3.4, without the octupole effect, e_{lim} is achieved very close to $\theta_{lb,\,0} = 90^\circ$. With octupole, e_{lim} can be achieved for initial inclinations $\theta_{lb,\,0}$ in the range $\theta_{lb,crit} \le \theta_{lb,0} \le 90^\circ$, where $\theta_{lb,crit}$ (the minimum inclination that can lead to $e_{max} = e_{lim}$) is determined by $\varepsilon_{oct} \simeq a e_b / a_b(1 - e_b^2)$, with no dependence on planet or stellar mass (see Liu et al. 2015). The fact that the 'window of extreme eccentricity' ($\theta_{lb,crit} \le \theta_{lb,0} \le 90^\circ$) is independent of M_p and $M_\star$, combined with the weak dependence of equation (47) on M_p and $M_\star$ explains the nearly constant migration fraction observed in our calculations. Note however that the migration fraction does depend on the assumed distributions of the planetary and binary orbital properties (a_0, a_b, e_b, $\theta_{lb,0}$), and alternate choices for these distributions would yield different migration fractions. A semi-analytic calculation of the migration/disruption fractions, based on the idea discussed here, is presented in Muñoz et al. (2016, submitted).

Regardless of the reason, the fact that $f_{mig} \approx$ constant is a useful finding. Recall that the disruption fractions quoted herein depend on the disruption condition, which depends on the planetary mass–radius relation, and is somewhat uncertain. However, noting that $f_{mig} \approx$ constant allows us to estimate an upper limit on the possible HJ fraction for any giant planet mass, by setting $f_{dis} \to 0$, so that $f_{mig} \to f_{HJ,\,max} \sim 13$ per cent.

5.4.2 *Final HJ orbital periods and spin-orbit misalignments*

Figs 20 and 21 show the final orbital periods and spin-orbit misalignments versus the initial inclination $\theta_{lb,\,0}$ for the HJs produced in our calculations. Note that we have removed the systems that resulted in tidal disruptions and non-migrating planets for clarity.

We see that the distribution of the final stellar obliquities are distinctly bimodal for $M_p = 1$–$3M_J$ around both G and F host stars, with peaks around 30°–40°, and 120°–130°. As planet mass increases, greater differences emerge between the results for G and F stars. For the G-type host star, massive planets tend to settle to lower obliquities. When $M_p = 5M_J$, the peak of the histogram occurs in the first bin ($\theta_{sl,f} = 0^\circ - 10^\circ$), with an underlying bimodal distribution of larger misalignments (Fig. 20). Thus, the tendency for spin-orbit alignment for massive planets presented in Section 5.3 and in Storch et al. (2014) is partially preserved when sampling over arbitrary binary eccentricities and separations. By contrast, the results for massive planets ($5M_J$) around the F-type host star (Fig. 21) show a greater degree of misalignment, with the peak of the distribution at $\theta_{sl,f} \sim 45^\circ$. This is in qualitative agreement with the pure quadrupole calculations in Section 5.2 (see Fig. 15).

We find that all combinations of stellar type and planet mass lead to a greater fraction of prograde ($\theta_{sl,f} \le 90^\circ$), rather than retrograde ($\theta_{sl,f} \ge 90^\circ$) configurations (see Table 3). However, the percentage of prograde planets around F stars is consistently lower than around G stars. For example, we find that for $M_p = 1M_J$, the prograde percentage is $\approx$78 per cent for the G star, and $\approx$65 per cent for the F star.

The bimodal $\theta_{sl,f}$ distributions for Jupiter-mass planets around G stars shown in Fig. 20 is quite different from those obtained by Naoz et al. (2012) and Petrovich (2015a). These authors find much broader $\theta_{sl,f}$ distributions, with no apparent 'gap' at $\theta_{sl,f} \sim 90^\circ$. A key reason for this difference is that the previous works considered

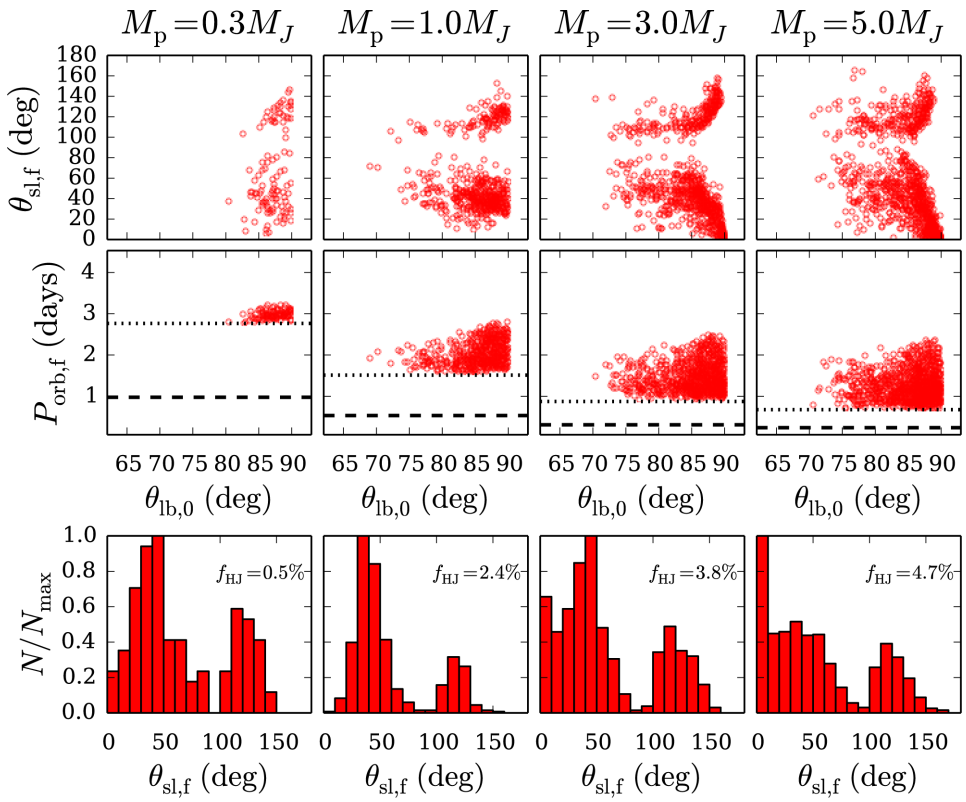

Figure 20. Final stellar obliquities $\theta_{sl,f}$ and orbital periods $P_{orb,f}$ for the systems shown in Fig. 18 that resulted in HJs. Parameters are $M_\star = 1.0\,M_\odot$ (the G-type star), and a_0, a_b, e_b, $\theta_{lb,0}$ randomly sampled over wide ranges, as described in the text, and indicated in Table 3. Top and middle panels depict the final spin-orbit angle $\theta_{sl,f}$ and orbital period $P_{orb,f}$ versus $\theta_{lb,0}$. The dashed lines, included for reference, indicate the orbital period at the tidal disruption radius, and the dotted lines indicate the minimum achievable orbital period, defined by $a_f \geq 2R_{tide}$. Bottom panels show histograms of $\theta_{sl,f}$, with a bin width $\Delta\theta_{sl,f} = 10°$.

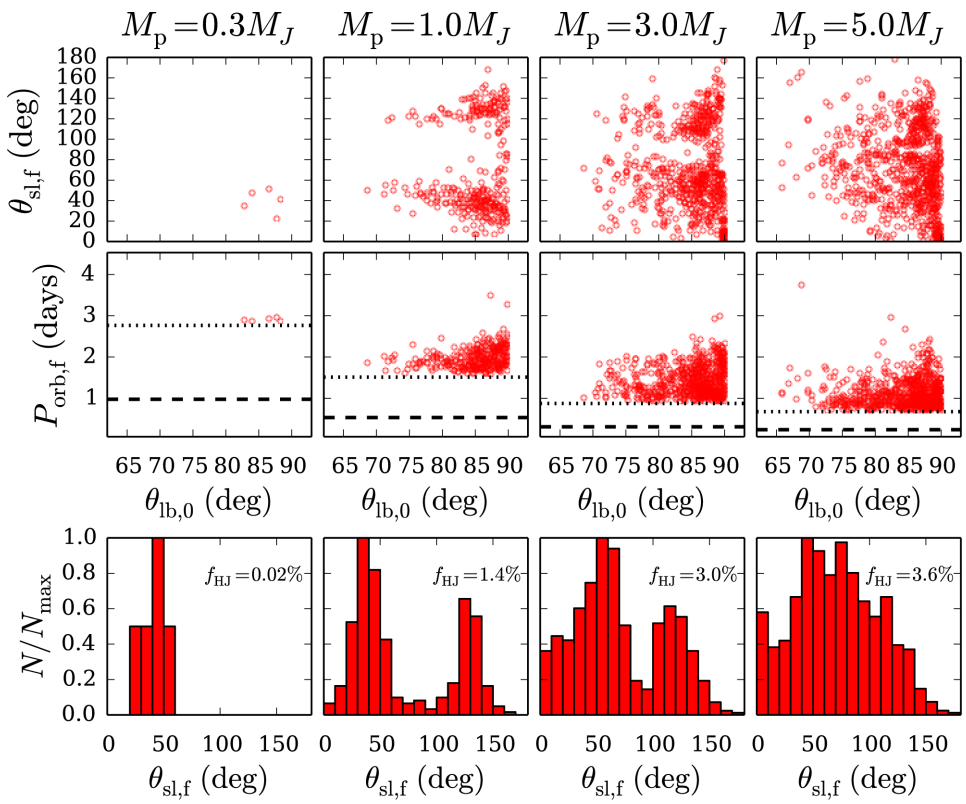

Figure 21. Same as Fig. 20, but showing results for planets around F stars.

slowly-rotating host stars (and non-evolving spin rates), which have weak spin-orbit couplings.

Also depicted in Figs 20 and 21 are the final orbital periods $P_{\rm orb,\,f}$ as a function of initial inclination. After the LK oscillations are suppressed, the tidal evolution occurs at nearly constant angular momentum, so that all planets settle to a final semimajor axis $a_{\rm f} \gtrsim 2r_{\rm Tide}$. Since $r_{\rm Tide}$ depends inversely on planet mass, high-mass planets are able to achieve shorter final orbital periods than low-mass planets. As a result, the lowest mass planets ($M_{\rm p} = 0.3M_{\rm J}$) reside farthest from their host stars, and exhibit the smallest spread in $P_{\rm orb,\,f}$. All calculations result in extremely close-in planets, with $P_{\rm orb,\,f} \lesssim 3$ d. This lack of longer period HJs produced by the LK mechanism is in agreement with calculations by Petrovich (2015a).

5.4.3 *Migration time*

For the subset of planets that undergo migration (resulting in either HJ formation or tidal disruption), it is useful to examine the migration time $t_{\rm mig}$. For systems that result in HJs, we define $t_{\rm mig}$ as the moment when the semimajor axis has decayed to $a < 0.1$ au, so that the planet is classified as an HJ (this is also the time at which we stop our integrations). For disrupted planets, $t_{\rm mig}$ is the point at which the planet crosses the tidal radius.

Fig. 22 shows cumulative distributions of the migration time $t_{\rm mig}$ for HJs and disrupted planets obtained from our simulation with G-type host stars (as in Figs 18 and 20). Two trends are apparent: First, most tidal disruptions occur early, with more than 75 per cent occurring within 0.1 Gyr. Secondly, the range of the HJ formation time varies with planet mass. For $5M_{\rm J}$ planets, $2{\rm Myr} \lesssim t_{\rm mig} \leq 5{\rm Gyr}$. In contrast, the HJ formation time for $0.3M_{\rm J}$ planets lies in the much more restricted range $2{\rm Gyr} \lesssim t_{\rm mig} \leq 5{\rm Gyr}$. The minimum migration time for low-mass planets thus differs significantly for low-mass planets.

The cause behind the lengthier HJ formation times for low-mass ($M_{\rm p} = 0.3M_{\rm J}$) planets is as follows. Recall that the orbital decay rate for planets undergoing LK migration (equation 32) has the dependence

$$\left|\frac{1}{a}\frac{{\rm d}a}{{\rm d}t}\right|_{\rm Tide,LK} \propto M_{\rm p}^{-1}a_{\rm F}^{-7} \quad \text{where} \quad a_{\rm F} = a(1-e_{\rm max}^2), \tag{66}$$

so that the tidal decay time-scale $t_{\rm Tide} \propto M_{\rm p}a_{\rm F}^7$. Since systems that produce surviving planets must satisfy $a_{\rm F}/2 \geq r_{\rm Tide}$, for each planet mass there is a minimum tidal decay time-scale

$$t_{\rm Tide,min} \propto M_{\rm p}r_{\rm Tide}^7 \propto M_{\rm p}^{-4/3}. \tag{67}$$

The minimum decay time needed to produce a surviving HJ thus increases for lower mass planets, as we find in our numerical calculations.

Finally, we note that LK migration is often attributed to need a long time to operate, usually $\sim 0.1 - 1$ Gyr time-scales, in contrast with disc-driven migration, which must occur before the gas dispersal time of a few Myr. While we confirm that this is indeed the case for Jupiter and sub-Jupiter mass planets, we find that massive planets ($M_{\rm p} \sim 3$–$5M_{\rm J}$) can migrate more quickly, within tens or occasionally even a few Myr, much more comparable to the time-scale for disc-driven migration.

5.5 Dependence on tidal dissipation strength

All results presented thus far adopt the tidal dissipation strength $\chi = 10$, corresponding to tidal lag time $\Delta t_{\rm L} = 1$ s. We now examine the effect of varying dissipation rate, by considering tidal

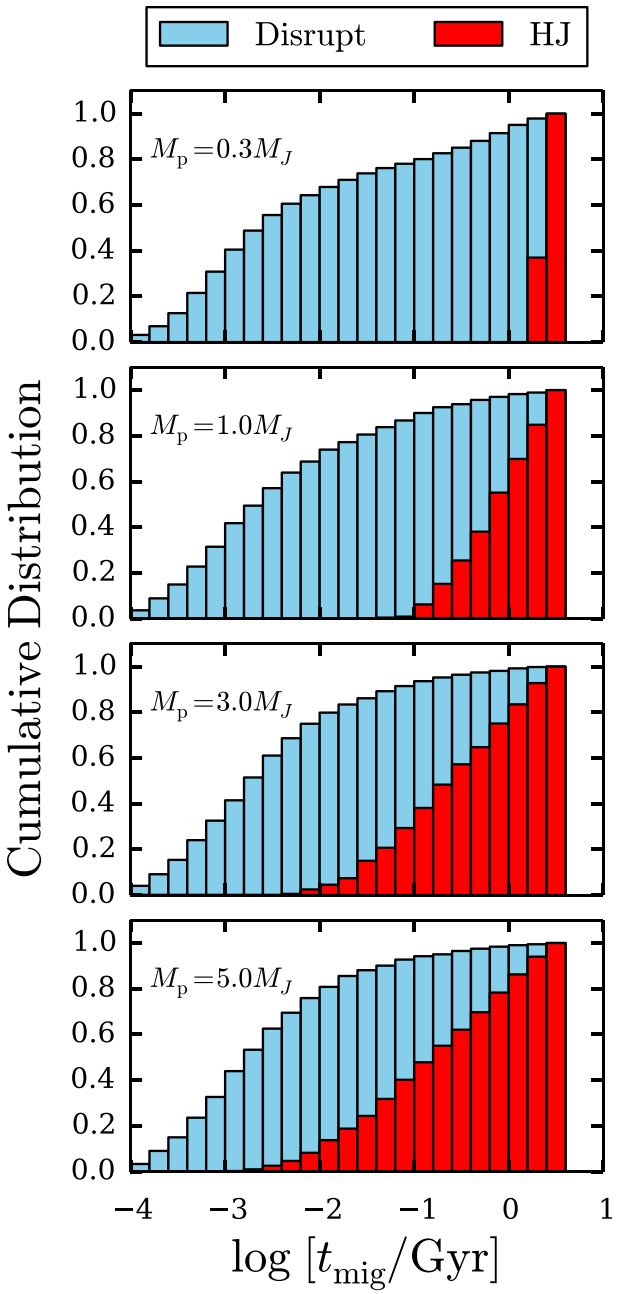

Figure 22. Cumulative distributions of migration times $t_{\rm mig}$, defined as the time at which the planet crosses the tidal radius (for the disrupted planets), or the time at which the semimajor axis decreases below 0.1 au (for the HJs). The results shown are the same set of simulations as depicted in Figs 18 and 20. Most tidal disruptions occur relatively early, with $\gtrsim$75 per cent occurring within 0.1 Gyr. The minimum time needed to produce an HJ depends on planet mass, and is $\sim$2 Gyr for $0.3M_{\rm J}$ planets, but $\sim$2 Myr for $5M_{\rm J}$ planets.

enhancement factors $\chi = 1$ and $\chi = 100$, so that $\Delta t_{\rm L} = 0.1$ and 10 s, respectively. All simulations presented in Section 5.4 were repeated with these values of χ; see Table 3.

Fig. 23 shows distributions of the HJ final orbital periods $P_{\rm orb,\,f}$ around the G star for each tidal dissipation strength (note that the corresponding results for the F star are nearly identical, and are not shown). The distributions for $\chi = 1$ are narrow, and concentrated towards low orbital periods, with $P_{\rm orb,\,f} \lesssim 2$ d across all planet

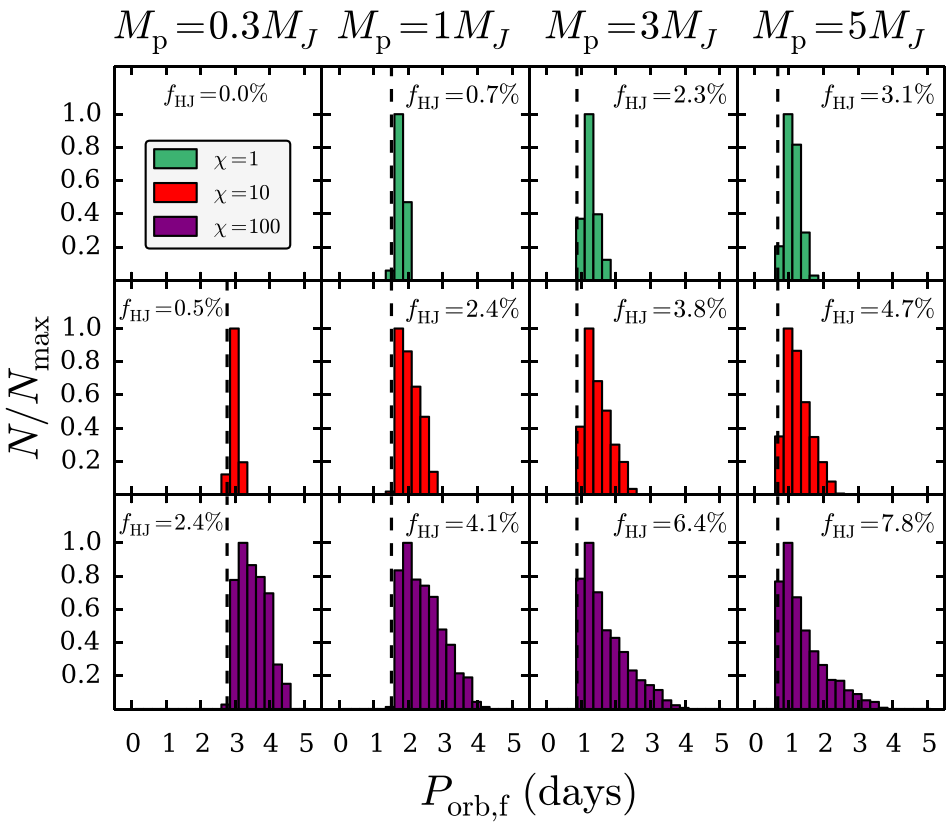

Figure 23. Effects of varying tidal dissipation strength χ on the distribution of final HJ orbital periods $P_{\rm orb,\,f}$ for planets around G stars. We show $\chi = 1$ (green, top row), $\chi = 100$ (purple, bottom row), along with our canonical value $\chi = 10$ (red, middle row). The distributions shown are the result of $N_{\rm run} \sim 9000$ total trials, out of which a fraction $f_{\rm HJ}$ resulted in HJ formation (see also Table 3). Each column shows a different planet mass, as labelled. The vertical dashed lines, included for reference, indicate the minimum achievable orbital period, at $a_{\rm f} = 2R_{\rm Tide}$. For $M_{\rm p} = 0.3$, 1, 3, $5M_{\rm J}$ respectively, the number of data points $N_{\rm HJ}$ in each histogram are as follows: top row, $\chi = 1$, $N_{\rm HJ} = 0$, 156, 490, 650; middle row, $\chi = 10$, $N_{\rm HJ} = 108$, 502, 811, 990; bottom row, $\chi = 100$, $N_{\rm HJ} = 513$, 875, 1370, 1670. Note that no close-in planets were produced for the combination $M_{\rm p} = 0.3M_{\rm J}$, $\chi = 1$.

masses. As χ increases, the distributions widen, since the enhanced tidal dissipation strength allows planets with larger pericentres to migrate inwards within 5 Gyr (see equation 32). However, note that regardless of the tidal dissipation strength, no HJs with final orbital periods $P_{\rm orb,\,f} \gtrsim 4.6$ d were produced. This lack of longer period HJs is consistent with previous calculations of HJ formation via the LK mechanism (Petrovich 2015a).

Not surprisingly, the HJ fraction $f_{\rm HJ}$ increases as χ increases. However, the migration fraction $f_{\rm mig} = f_{\rm HJ} + f_{\rm dis}$ remains roughly constant, varying by only a few per cent across all combinations of planet mass, stellar type, and dissipation strength, between ∼11and14 per cent. This is consistent with the discussion in Section 5.4.1 (see last two paragraphs of that subsection). Most of the migrating planets originate from systems where the octupole effect plays an important role, and the 'window of extreme eccentricity' (needed for achieving migration) is independent of $M_{\rm p}$, $M_\star$ and χ. On the other hand, most HJs originate from systems with low $\varepsilon_{\rm oct}$ and high $\theta_{\rm lb,\,0}$ (see Figs 18 and 19), where the octupole effect is not essential for migration. For these systems, enhanced tidal dissipation allows planets with larger periastron distances to migrate (see equation 32), leading to a larger $f_{\rm HJ}$.

Figs 24 and 25 compare the effects of varying χ on the distribution of $\theta_{\rm sl,\,f}$ for planets around G and F stars. Increasing χ generally leads to broader distributions, with a greater fraction of planets at relatively low obliquities ($\theta_{\rm sl,\,f} \lesssim 30^\circ$), but has little effect on the overall shape. In particular, the bimodality observed previously for (1–3)$M_{\rm J}$ planets is preserved.

5.6 Primordial misalignment

Finally, we present HJ stellar obliquity distributions for systems in which the initial stellar spin-orbit angle is misaligned, i.e. $\theta_{\rm sl,\,0} \neq 0$. Such initially misaligned configurations are relevant because various works (e.g. Bate et al. 2010; Lai et al. 2011; Batygin 2012; Batygin & Adams 2013; Lai 2014) have suggested the possibility of 'primordial misalignments' in which the protoplanetary disc becomes tilted relative to the stellar spin axis. We limit the discussion to planets around G stars, and the canonical tidal dissipation strength $\chi = 10$. We fix $\theta_{\rm sl,\,0}$, and integrate a series of systems with the initial phase of $\hat{\boldsymbol{S}}_\star$ around $\hat{\boldsymbol{L}}$ (i.e. $\phi_{\rm sl,\,0}$, where $\phi_{\rm sl,\,0}$ is the azimuthal angular coordinate in the frame where $\hat{\boldsymbol{L}}$ is along the z-axis) randomly sampled uniformly in $[0, 2\pi]$.

Fig. 26 shows results for $\theta_{\rm sl,\,0} = 30^\circ$ and 60°, along with the canonical $\theta_{\rm sl,\,0} = 0^\circ$ case shown previously in Fig. 20. When $\theta_{\rm sl,\,0} = 30^\circ$, the distributions of $\theta_{\rm sl,f}$ are bimodal for all planet masses, including planets with $M_{\rm p} = 5M_{\rm J}$. For $\theta_{\rm sl,\,0} = 60^\circ$, the bimodality has vanished, and the distributions are roughly symmetric around 90°. We conclude that non-zero initial obliquities can affect the final spin-orbit misalignment, such that the bimodal peaks present for $\theta_{\rm sl,\,0} = 0^\circ$ tend to merge as $\theta_{\rm sl,\,0}$ increases.

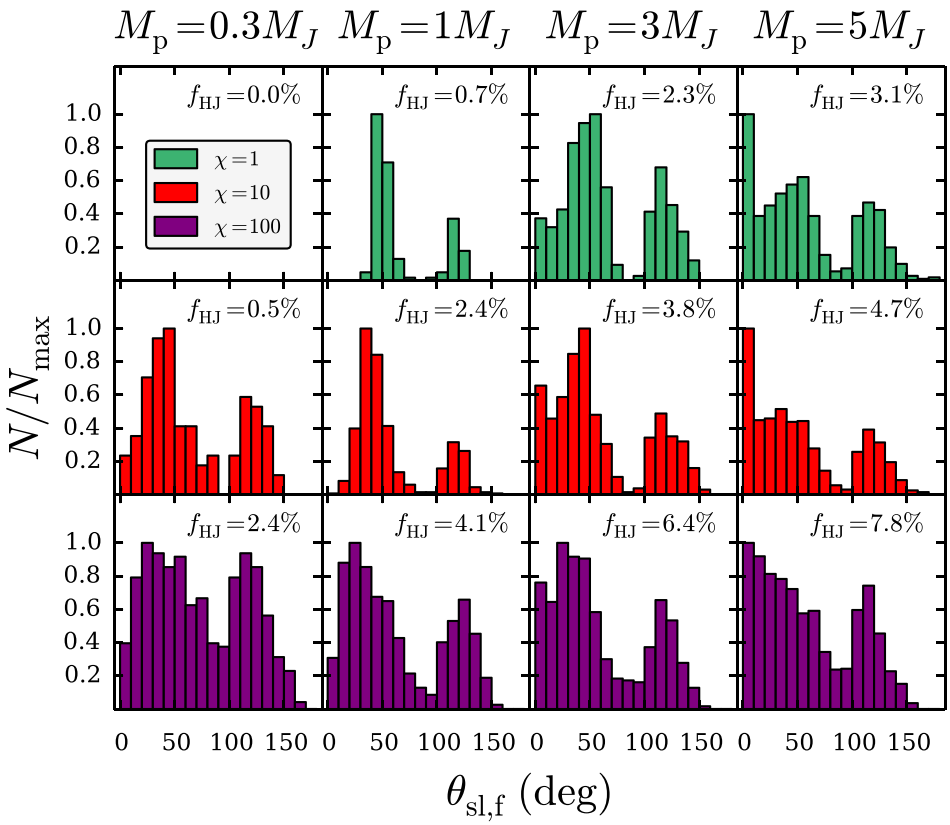

Figure 24. Effects of varying tidal dissipation strength χ on the distributions of $\theta_{sl,f}$ for HJs around G stars (the same sample as in Fig. 23). We show $\chi = 1$ (green, top row), $\chi = 100$ (purple, bottom row), along with our canonical value $\chi = 10$ shown previously in Fig. 20 (red, middle row). For $M_p = 0.3$, 1, 3, $5M_J$ respectively, the number of data points N_{HJ} in each histogram are as follows: top row (from left to right), $\chi = 1$, $N_{HJ} = 0$, 156, 490, 650; middle row, $\chi = 10$, $N_{HJ} = 108$, 502, 811, 990; bottom row, $\chi = 100$, $N_{HJ} = 513$, 875, 1370, 1670. Note that no close-in planets were produced for $M_p = 0.3M_J$, $\chi = 1$. For most planet masses, increasing χ broadens the distribution of $\theta_{sl,f}$, but the overall shape (usually bimodal) remains unchanged. Increasing χ leads to more planets with low obliquities ($\theta_{sl,f} \lesssim 20^\circ$).

6 CONCLUSION

6.1 Summary of results

The main goal of this paper is to conduct a thorough population synthesis of the production of misaligned close-in giant planets (HJs) in stellar binaries by the mechanism of LK oscillations with tidal dissipation, examining the previously unexplored dependence on planet mass, and stellar type and spin properties. The complex evolution of the stellar spin axis in systems with planets undergoing LK oscillations poses a rich dynamical problem (see also Storch et al. 2014; Storch & Lai 2015), and can affect the final distributions of spin-orbit misalignments. We have calculated the HJ production fractions and planet tidal disruption fractions for a wide variety of systems, exploring their dependence on planet mass, stellar properties and tidal dissipation rate. We have also presented a number of semi-analytical calculations, which are useful in understanding the results of our population synthesis. Our main results can be summarized as follows.

(i) Planet mass is important in determining the HJ formation and tidal disruption fractions (see Table 3). The fraction of systems resulting in HJs (f_{HJ}) increases with planet mass, due to fewer tidal disruptions. For Jupiter-mass planets, we find that $f_{HJ} \approx 0.5$–4 per cent depending on the assumed tidal dissipation rate and host star mass. In general f_{HJ} increases with the tidal dissipation rate and decreases with stellar mass. For more massive ($5M_J$) planets, we find a higher fraction, with $f_{HJ} \approx 3$ per cent $-$ 7.5 per cent. The fraction of systems resulting in 'hot Saturns' ($M_p \sim 0.3M_J$) are low, especially around massive ($M_\star = 1.4\,M_\odot$, spectral type F) stars. As a result, hot Saturns around massive stars are unlikely to be produced by LK migration in binaries, unless the tidal dissipation strength in the planet is high (with $\chi \gtrsim 100$, corresponding to $\Delta t_L \gtrsim 10$ sec).

(ii) We find that the 'migration fraction,' defined as the sum of the HJ and disruption fractions, $f_{mig} = f_{HJ} + f_{dis}$, has a rather weak dependence on planet mass, stellar type and tidal dissipation rate, and is always in the range of 11–14 per cent (see Table 3). This behaviour can be qualitatively understood from analytical migration criteria (see Sections 3.4 and 5.4.1, particularly equation (47). Since the tidal disruption fraction for lower mass planets is higher (due to the increased tidal radius), a constant migration fraction implies that f_{HJ} should decrease with planet mass, as described above.

(iii) HJs are produced only in systems when the ratio of the binary semimajor axis a_b and the initial planet semimajor axis a_0 lies in the range $60 \lesssim a_b/a_0 \lesssim 300$ (see Figs 18 and 19). In addition, no HJs are produced for systems with the dimensionless octupole parameter (see equation 4) $\varepsilon_{oct} \gtrsim 0.01 - 0.02$, where the range depends on the planet mass (see Figs 18 and 19). These place constraints on the types of binary properties and initial planet semimajor axes that are able to induce migration without causing tidal disruption.

(iv) The distribution of final spin-orbit misalignment angles depends on planet mass and the spin history of host stars (see Figs 24

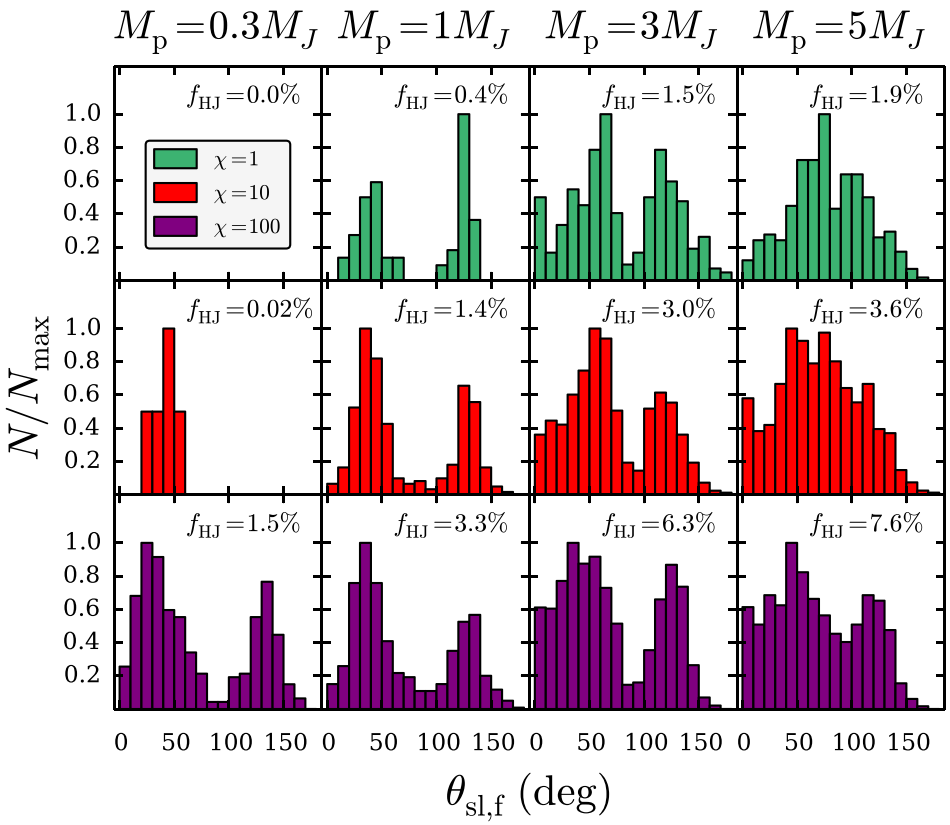

Figure 25. Same as Fig. 24, but showing results for planets around F stars. The distributions shown are the result of $N_{run} \sim 9000$ total trials, out of which a fraction f_{HJ} resulted in HJ formation (see also Table 3). For $M_p = 0.3$, 1, 3, $5M_J$, respectively, the number of data points N_{HJ} in each histogram are as follows: top row, $\chi = 1$, $N_{HJ} = 0$, 75, 310, 394; middle row, $\chi = 10$, $N_{HJ} = 5$, 305, 640, 764; bottom row, $\chi = 100$, $N_{HJ} = 330$, 711, 1339, 1609.

and 25). For $M_p = (1–3)M_J$, the distributions are always bimodal, with peaks near $\theta_{sl,f} \approx 40^\circ$ and 130°. This bimodality is independent of stellar type. For solar-type stars, higher mass planets ($M_p = 5M_J$) exhibit a preference for low final obliquities, with $\theta_{sl,f} < 10^\circ$ (see Figs 20 and 24), although misalignment still remains possible. By contrast, for F stars, the $\theta_{sl,f}$ distributions for massive planets are broad, with no clear bimodality (see Fig. 25). We attribute the higher degree of misalignment around F stars to the stronger torque from the (more rapidly rotating) host star acting on the orbit, thereby erasing the tendency towards alignment observed for $5M_J$ planets around G stars. In general, the back-reaction torques from the stellar quadrupole on the planet's orbit, as well as the octupole effect from the binary companion, give rise to a variety of evolutionary paths towards spin-orbit misalignments during LK migration (Section 4), and result in a complicated dependence of the $\theta_{sl,f}$-distribution on planet mass and stellar type.

(v) The final stellar obliquity distribution does not depend significantly on tidal dissipation rate within the planet, although higher rates of dissipation do tend to broaden the distributions.

(vi) While most of the calculations in this paper assume initial alignment between the stellar spin and planet's orbit axis ($\theta_{sl,0} = 0^\circ$), we also explore the effect of an initial ('primordial') misalignment. We find that the bimodality present when $\theta_{sl,0} = 0^\circ$ begins to merge as $\theta_{sl,0}$ increases (see Fig. 26). For modest initial misalignments ($\theta_{sl,0} = 30^\circ$), the final $\theta_{sl,f}$ distribution remains bimodal across all planet masses, with the peaks slightly shifted towards 90°. For higher initial misalignment ($\theta_{sl,0} = 60^\circ$) the bimodality has nearly vanished, and the distribution is broadly distributed and centred near $\theta_{sl,f} \sim 70^\circ–80^\circ$.

6.2 Discussion

Previous studies of HJ production in stellar binaries that include the octupole potential (Naoz et al. 2012; Petrovich 2015a) focused on a single planet mass and initial planet semimajor axis ($M_p = 1M_J$, $a_0 = 5$ au), and a single host star type ($M_\star = 1\,M_\odot$, with constant spin rate). This paper has expanded upon these previous works by exploring a range of giant planet masses and orbital separations ($M_p = 0.3 - 5M_J$, $a_0 = 1–5$ au) and two host stellar types ($M_\star = 1$, $1.4\,M_\odot$), with each stellar type governed by differing magnetic braking laws. We also consider systems with 'primordial misalignment' where the initial stellar obliquity $\theta_{sl,0} \neq 0$.

In terms of HJ production fractions (f_{HJ}), our results are in good agreement with Petrovich (2015a). We find $f_{HJ} \sim$ a few per cent typically, except for sub-Jupiter mass planets which can have much lower fractions ($f_{HJ} \lesssim 1$ per cent). In terms of tidal disruptions, Petrovich (2015a) finds a much higher disruption fraction, with $f_{dis} \sim 25$ per cent, in part because he places all planets initially at $a_0 = 5$ au from the host star, whereas we vary the initial semimajor axis uniformly in the range $a_0 = 1–5$ au. Planets that begin at larger orbital separations experience stronger forcing from the binary and less pericentre precession due to SRFs, and thus can achieve sufficiently high eccentricities such that the pericentre distance $a_p = a(1 - e_{max})$ is smaller, resulting in more disruptions (see Fig. 6). Another reason for the higher disruption fraction quoted in Petrovich (2015a) lies in the choice of binary eccentricity range (he chooses a maximum $e_b = 0.9 - 0.95$, in contrast with 0.8 assumed in this work). As noted before (see the beginning of Section 5.4, the actual eccentricity distribution of stellar binaries

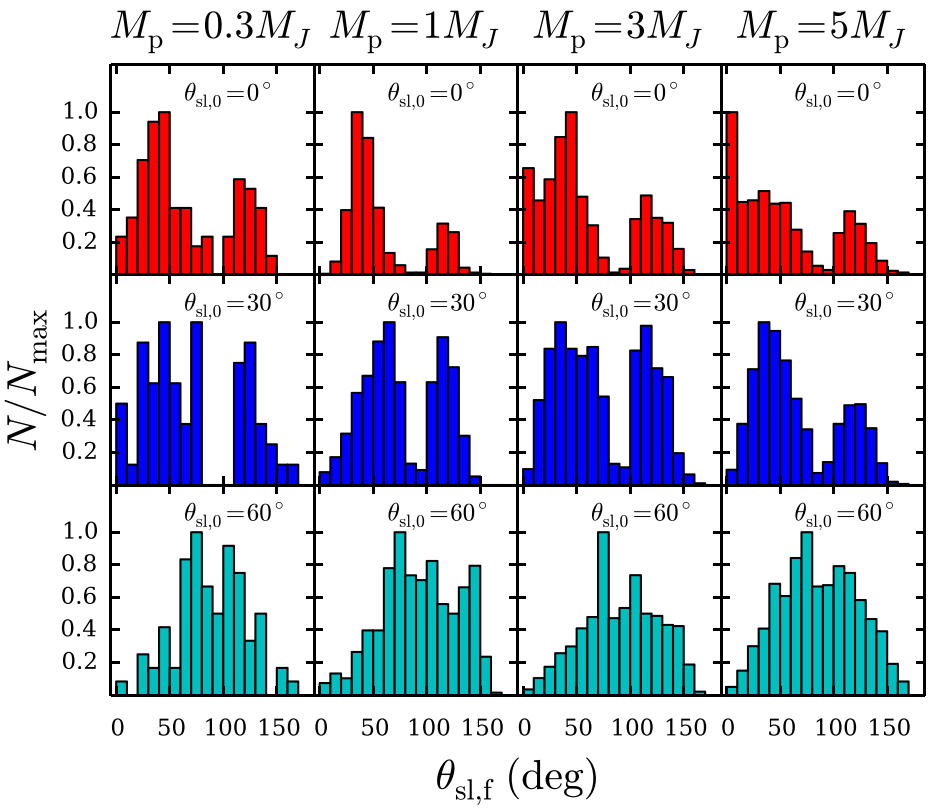

Figure 26. The effect of primordial misalignment ($\theta_{\rm sl,\,0} \neq 0$) on distributions of $\theta_{\rm sl,\,f}$. We show results for planets around G stars, with the canonical dissipation strength $\chi = 10$. Top row (red): $\theta_{\rm sl,\,0} = 0^\circ$, as shown previously in Fig. 20. Middle row (blue): $\theta_{\rm sl,\,0} = 30^\circ$. Bottom row (cyan): $\theta_{\rm sl,\,0} = 60^\circ$. For $M_{\rm p} = 0.3$, 1, 3, $5M_{\rm J}$ respectively, the number of data points $N_{\rm HJ}$ in each histogram are as follows: top row (from left to right), $\theta_{\rm sl,\,0} = 0^\circ$, $N_{\rm HJ} = 108$, 502, 811, 990. Middle row, $\theta_{\rm sl,\,0} = 30^\circ$, $N_{\rm HJ} = 61$, 544, 844, 1021. Bottom row, $\theta_{\rm sl,\,0} = 60^\circ$, $N_{\rm HJ} = 82$, 556, 943, 1037. See Table 3 for further information.

(especially those that allow planet formation) is very uncertain. Also, including binaries with $e_{\rm b} \gtrsim 0.9$ may result in over-populating systems close to the stability limit (with small $a_{\rm b}(1 - e_{\rm b})/a_0$). Our HJ fractions (for $M_{\rm p} = 1\,M_{\rm J}$ around solar-type stars) are lower than those found in Naoz et al. (2012), who give $f_{\rm HJ} \sim 15$ per cent. One major reason for the difference is that Naoz et al. (2012) use the tidal radius equation (48), but set $f \simeq 0.6$, whereas we use $f = 1$. Note that since the migration fraction $f_{\rm mig} = f_{\rm HJ} + f_{\rm dis}$ is always in range of 11-14 per cent regardless of planet mass and stellar type (see Section 5.4.1 and Table 3), in the extremely unlikely event that all of our tidally disrupted planets actually survived as HJs, the maximum possible HJ production fraction from our simulations is $f_{\rm HJ,\,max} = f_{\rm mig} \sim 13$ per cent.

Observations constrain the HJ occurrence rate around solar-type stars to be ∼1 per cent (e.g. Wright et al. 2012). Since the observed stellar companion fraction in HJ systems is $\lesssim$50 per cent (Ngo et al. 2015), our calculations imply that LK migration from stellar companions can probably explain around ∼15 per cent of observed HJs (using $f_{\rm HJ} = 3$ per cent, and assuming a giant planet occurrence rate of 10 per cent).

The calculations presented in this paper never produce HJs with final orbital periods $P_{\rm orb,\,f} \gtrsim 4.5$ d, with typical periods in the range of 1–3 d, depending on planet mass and tidal dissipation strength (see Fig. 23). More massive planets tend to have shorter periods (sometimes $\lesssim$1 d) because they can survive tidal disruption during the high-eccentricity periastron passage. Thus, it is clear that LK migration in stellar binaries cannot explain the observed population of HJs with periods greater than 4 d (see also Petrovich 2015a for an in-depth discussion of the tendency for LK migration to produce an excess of 'Very Hot Jupiters' compared to observations.) In addition, for both types of stars, our calculations yield very few planets in the process of migration. In particular, very few 'warm Jupiters' are produced with $0.1 \lesssim a \lesssim 0.5$ au after evolving the system for 5 Gyr (see also Petrovich 2015a).

In the absence of primordial misalignment (so that $\theta_{\rm sl,\,0} = 0^\circ$), our calculations always predict, for planet masses $M_{\rm p} = 1$–$3M_{\rm J}$, a bimodal distribution of final stellar spin-orbit misalignments, with peaks at $\theta_{\rm sl,f} \approx 40^\circ$ and 130°, and a dearth around 90°. This result is independent of host stellar type and tidal dissipation strength (see Figs 24 and 25). Such bimodality results from the stellar spin evolution transitioning from the non-adiabatic to fully adiabatic regime (Storch et al. 2016, submitted), and thus may be interpreted as a clear signature of HJ formation from LK oscillations with tidal dissipation. However, for $M_{\rm p} = 5M_{\rm J}$ planets, the shape of the distribution of $\theta_{\rm sl,f}$ differs substantially, and for planets around F stars, nearly polar orbits ($\theta_{\rm sl,f} \sim 90^\circ$) are commonly produced (see Fig. 25, right-hand panels).

On the other hand, when significant primordial misalignments are present, with $\theta_{\rm sl,\,0} \gtrsim 60^\circ$ (see Section 5.6), the bimodality of the final misalignment distribution disappears, and planets on polar orbits are easily produced (see Fig. 26, bottom row). Observationally, the distribution of HJ spin-orbit misalignments does not exhibit a clear bimodal structure (e.g. Albrecht et al. 2012b) and a handful of observed systems have nearly polar orbits, such as WASP-1b (Simpson et al. 2011), WASP-7b (Albrecht et al. 2012a), and WASP-79b (Addison et al. 2013) (these systems mostly have $M_{\rm p} \sim 1M_{\rm J}$ and host star mass $M_\star \approx 1.2$–$1.5\,{\rm M}_\odot$). Thus, without substantial primordial misalignments, LK migration in stellar binaries cannot

explain the observed $\theta_{\rm sl,f}$ distribution of HJs. This again suggests that the majority (∼85 per cent) of HJs are probably formed by other mechanisms (e.g. disc-driven migration).

One physical effect not included in this paper is tidal dissipation in the host stars. This can in principle affect the semimajor axis of very close-in giant planets, and change the spin-orbit misalignment angle, as studied in numerous papers (e.g. Barker & Ogilvie 2009; Jackson, Barnes & Greenberg 2009; Winn et al. 2010; Matsumura, Peale & Rasio 2010; Lai 2012; Rogers & Lin 2013; Valsecchi, Rasio & Steffen 2014; Xue et al. 2014). We neglect stellar tidal dissipation on purpose in this paper because, compared to tidal dissipation in planets, stellar tides play a negligible role in circularizing high-eccentricity planets undergoing LK oscillations. Moreover, the stellar tidal dissipation rate is highly uncertain, and likely depends on the stellar type and planet mass (see Ogilvie 2014 for a review); it is also possible that the tidal process and time-scale for spin-orbit alignment are different from those for orbital decay (Lai 2012). Once an HJ has formed through high-eccentricity migration, it is straightforward to examine the effect of stellar tides (using parametrized tidal models) on the subsequent evolution of the system.

ACKNOWLEDGEMENTS

We thank Diego Muñoz and Smadar Naoz for useful discussions, and especially Cristobal Petrovich for useful discussion and comments on the manuscript. This work has been supported in part by NSF grant AST-1211061, and NASA grants NNX14AG94G and NNX14AP31G. KRA is supported by the NSF Graduate Research Fellowship Program under Grant No. DGE-1144153.

REFERENCES

Addison B. C., Tinney C. G., Wright D. J., Bayliss D., Zhou G., Hartman J. D., Bakos G. Á., Schmidt B., 2013, ApJ, 774, L9
Albrecht S., Winn J. N., Butler R. P., Crane J. D., Shectman S. A., Thompson I. B., Hirano T., Wittenmyer R. A., 2012a, ApJ, 744, 189
Albrecht S. et al., 2012b, ApJ, 757, 18
Alexander M. E., 1973, ASS, 23, 459
Barker A. J., Ogilvie G. I., 2009, MNRAS, 395, 2268
Bate M. R., Lodato G., Pringle J. E., 2010, MNRAS, 401, 1505
Batygin K., 2012, Nature, 491, 418
Batygin K., Adams F. C., 2013, ApJ, 778, 169
Beaugé C., Nesvorný D., 2012, ApJ, 751, 119
Becker J. C., Vanderburg A., Adams F. C., Rappaport S. A., Schwengeler H. M., 2015, ApJ, 812, L18
Bouvier J., 2013, EAS Publ. Ser., 62, 143
Chatterjee S., Ford E. B., Matsumura S., Rasio F. A., 2008, ApJ, 686, 580
Claret A., Gimenez A., 1992, A&AS, 96, 255
Correia A. C. M., Laskar J., Farago F., Boué G., 2011, Celest. Mech. Dyn. Astron., 111, 105
Dawson R. I., Murray-Clay R. A., 2013, ApJ, 767, L24
Dawson R. I., Murray-Clay R. A., Johnson J. A., 2015, ApJ, 798, 66
Eggleton P. P., Kiseleva-Eggleton L., 2001, ApJ, 562, 1012
Fabrycky D., Tremaine S., 2007, ApJ, 669, 1298
Feng Y. K., Wright J. T., Nelson B., Wang S. X., Ford E. B., Marcy G. W., Isaacson H., Howard A. W., 2015, ApJ, 800, 22
Fielding D. B., McKee C. F., Socrates A., Cunningham A. J., Klein R. I., 2015, MNRAS, 450, 3306
Ford E. B., Rasio F. A., 2008, ApJ, 686, 621
Ford E. B., Kozinsky B., Rasio F. A., 2000, ApJ, 535, 385
Foucart F., Lai D., 2011, MNRAS, 412, 2799
Guillochon J., Ramirez-Ruiz E., Lin D., 2011, ApJ, 732, 74
Hébrard G. et al., 2008, A&A, 488, 763
Holman M., Touma J., Tremaine S., 1997, Nat, 386, 254
Hut P., 1981, A&A, 99, 126
Innanen K. A., Zheng J. Q., Mikkola S., Valtonen M. J., 1997, AJ, 113, 1915
Jackson B., Barnes R., Greenberg R., 2009, ApJ, 698, 1357
Jurić M., Tremaine S., 2008, ApJ, 686, 603
Knutson H. A. et al., 2014, ApJ, 785, 126
Kozai Y., 1962, AJ, 67, 591
Lai D., 2012, MNRAS, 423, 486
Lai D., 2014, MNRAS, 440, 3532
Lai D., Foucart F., Lin D. N. C., 2011, MNRAS, 412, 2790
Laughlin G., Crismani M., Adams F. C., 2011, ApJ, 729, LL7
Lidov M. L., 1962, Planet. Space Sci., 9, 719
Liu B., Muñoz D. J., Lai D., 2015, MNRAS, 447, 751
McQuillan A., Mazeh T., Aigrain S., 2014, ApJS, 211, 24
Mardling R. A., Aarseth S. J., 2001, MNRAS, 321, 398
Matsumura S., Peale S. J., Rasio F. A., 2010, ApJ, 725, 1995
Mazeh T., Shaham J., 1979, A&A, 77, 145
Moutou C. et al., 2011, A&A, 533, A113
Muñoz D. J., Lai D., Liu B., 2016, submitted
Nagasawa M., Ida S., Bessho T., 2008, ApJ, 678, 498
Naoz S., Fabrycky D. C., 2014, ApJ, 793, 137
Naoz S., Farr W. M., Rasio F. A., 2012, ApJ, 754, LL36
Narita N., 2009, PASJ, 61, 991
Neveu-VanMalle M. et al., 2015, preprint (arXiv:1509.07750)
Ngo H. et al., 2015, ApJ, 800, 138
Ogilvie G. I., 2014, ARA&A, 52, 171
Petrovich C., 2015a, ApJ, 799, 27
Petrovich C., 2015b, ApJ, 805, 75
Raghavan D. et al., 2010, ApJS, 190, 1
Rasio F. A., Ford E. B., 1996, Science, 274, 954
Rogers T. M., Lin D. N. C., 2013, ApJ, 769, L10
Simpson E. K. et al., 2011, MNRAS, 414, 3023
Skumanich A., 1972, ApJ, 171, 565
Socrates A., Katz B., Dong S., Tremaine S., 2012, ApJ, 750, 106
Spalding C., Batygin K., 2014, ApJ, 790, 42
Storch N. I., Lai D., 2015, MNRAS, 448, 1821 (SL15)
Storch N. I., Anderson K. R., Lai D., 2014, Science, 345, 1317
Storch N. I., Lai D., Anderson K. R., 2016, submitted
Thies I., Kroupa P., Goodwin S. P., Stamatellos D., Whitworth A. P., 2011, MNRAS, 417, 1817
Tokovinin A., Kiyaeva O., 2015, preprint (arXiv:1512.00278)
Triaud A. H. M. J. et al., 2010, A&A, 524, A25
Valsecchi F., Rasio F. A., Steffen J. H., 2014, ApJ, 793, L3
Wang J., Fischer D. A., Horch E. P., Xie J.-W., 2015, ApJ, 806, 248
Winn J. N., Johnson J. A., Albrecht S., Howard A. W., Marcy G. W., Crossfield I. J., Holman M. J., 2009, ApJ, 703, L99
Winn J. N., Fabrycky D., Albrecht S., Johnson J. A., 2010, ApJ, 718, L145
Wright J. T., Marcy G. W., Howard A. W., Johnson J. A., Morton T. D., Fischer D. A., 2012, ApJ, 753, 160
Wu Y., Lithwick Y., 2011, ApJ, 735, 109
Wu Y., Murray N., 2003, ApJ, 589, 605
Wu Y., Murray N. W., Ramsahai J. M., 2007, ApJ, 670, 820
Xue Y., Suto Y., Taruya A., Hirano T., Fujii Y., Masuda K., 2014, ApJ, 784, 66

APPENDIX A: EQUATIONS

In this appendix we present the secular equations of motion governing the planetary orbit and stellar spin axis. The reader is referred to Table 1 for a concise summary of the notation used in this paper.

A1 LK oscillations

The hierarchical triple systems studied in this paper consist of an inner binary $M_\star$ (host star) and $M_{\rm p}$ (planet), with total mass $M_{\rm tot} = M_\star + M_{\rm p}$, with an outer stellar mass binary companion $M_{\rm b}$. The planet has semimajor axis a and eccentricity e, and the binary companion has semimajor axis $a_{\rm b}$ and eccentricity $e_{\rm b}$. The inner

binary is characterized by the unit vectors $\hat{\boldsymbol{L}}$ and $\hat{\boldsymbol{e}}$, where $\hat{\boldsymbol{L}}$ is in the direction of the orbital angular momentum vector $\boldsymbol{L}$, and $\hat{\boldsymbol{e}}$ is in the direction of the eccentricity vector $\boldsymbol{e}$. Similarly, the outer binary is characterized by the unit vectors $\hat{\boldsymbol{L}}_{\rm b}$ and $\hat{\boldsymbol{e}}_{\rm b}$. Since we are considering systems in the regime $M_{\rm p} \ll M_{\rm b}$, the effect of the planet on the outer binary is negligible, and $\hat{\boldsymbol{L}}_{\rm b}$ and $\hat{\boldsymbol{e}}_{\rm b}$ are held constant. The inclination of the planetary orbit relative to the outer binary is specified by $\cos\theta_{\rm lb} = \hat{\boldsymbol{L}} \cdot \hat{\boldsymbol{L}}_{\rm b}$. If the outer binary companion has inclination $\theta_{\rm lb} \gtrsim 40^\circ$, the planet undergoes periodic variations in its orbital eccentricity and inclination (Kozai 1962; Lidov 1962), denoted in this paper as LK oscillations. The secular equations of motion for $\boldsymbol{L}$ and $\boldsymbol{e}$ are, to octupole order in the disturbing potential of the binary (Liu et al. 2015, see also Petrovich 2015b),

$$\begin{aligned}\left.\frac{{\rm d}\boldsymbol{L}}{{\rm d}t}\right|_{\rm LK} &= \left.\frac{{\rm d}\boldsymbol{L}}{{\rm d}t}\right|_{\rm LK,\,quad} + \left.\frac{{\rm d}\boldsymbol{L}}{{\rm d}t}\right|_{\rm LK,\,oct} \\ &= \frac{3}{4}\frac{L}{t_k(1-e^2)^{1/2}}\left[(\mathbf{j}\cdot\hat{\boldsymbol{L}}_{\rm b})\mathbf{j}\times\hat{\boldsymbol{L}}_{\rm b} - 5(\boldsymbol{e}\cdot\hat{\boldsymbol{L}}_{\rm b})\boldsymbol{e}\times\hat{\boldsymbol{L}}_{\rm b}\right] \\ &\quad - \frac{75}{64}\frac{\varepsilon_{\rm oct}L}{t_k(1-e^2)^{1/2}}\left\{\left[2\left[(\boldsymbol{e}\cdot\hat{\boldsymbol{L}}_{\rm b})(\mathbf{j}\cdot\hat{\boldsymbol{L}}_{\rm b})\right.\right.\right. \\ &\quad \left.\left. + (\boldsymbol{e}\cdot\hat{\boldsymbol{L}}_{\rm b})(\mathbf{j}\cdot\hat{\boldsymbol{e}}_{\rm b})\right]\mathbf{j} + 2\left[(\mathbf{j}\cdot\hat{\boldsymbol{e}}_{\rm b})(\mathbf{j}\cdot\hat{\boldsymbol{L}}_{\rm b})\right. \right. \\ &\quad \left.\left. - 7(\boldsymbol{e}\cdot\hat{\boldsymbol{L}}_{\rm b})(\boldsymbol{e}\cdot\hat{\boldsymbol{L}}_{\rm b})\right]\boldsymbol{e}\right]\times\hat{\boldsymbol{L}}_{\rm b} \\ &\quad + \left[2(\boldsymbol{e}\cdot\hat{\boldsymbol{L}}_{\rm b})(\mathbf{j}\cdot\hat{\boldsymbol{L}}_{\rm b})\mathbf{j} + \left[\frac{8}{5}e^2 - \frac{1}{5}\right.\right. \\ &\quad \left.\left. - 7(\boldsymbol{e}\cdot\hat{\boldsymbol{L}}_{\rm b})^2 + (\mathbf{j}\cdot\hat{\boldsymbol{L}}_{\rm b})^2\right]\boldsymbol{e}\right]\times\hat{\boldsymbol{e}}_{\rm b}\Bigg\}, \end{aligned} \tag{A1}$$

and

$$\begin{aligned}\left.\frac{{\rm d}\boldsymbol{e}}{{\rm d}t}\right|_{\rm LK} &= \left.\frac{{\rm d}\boldsymbol{e}}{{\rm d}t}\right|_{\rm LK,\,quad} + \left.\frac{{\rm d}\boldsymbol{e}}{{\rm d}t}\right|_{\rm LK,\,oct} \\ &= \frac{3}{4t_k}\left[(\mathbf{j}\cdot\hat{\boldsymbol{L}}_{\rm b})\boldsymbol{e}\times\hat{\boldsymbol{L}}_{\rm b} + 2\mathbf{j}\times\boldsymbol{e} - 5(\boldsymbol{e}\cdot\hat{\boldsymbol{L}}_{\rm b})\mathbf{j}\times\hat{\boldsymbol{L}}_{\rm b}\right] \\ &\quad - \frac{75\varepsilon_{\rm oct}}{64t_k}\left\{\left[2(\boldsymbol{e}\cdot\hat{\boldsymbol{L}}_{\rm b})(\mathbf{j}\cdot\hat{\boldsymbol{L}}_{\rm b})\boldsymbol{e}\right.\right. \\ &\quad \left.\left. + \left[\frac{8}{5}e^2 - \frac{1}{5} - 7(\boldsymbol{e}\cdot\hat{\boldsymbol{L}}_{\rm b})^2 + (\mathbf{j}\cdot\hat{\boldsymbol{L}}_{\rm b})^2\right]\mathbf{j}\right]\times\hat{\boldsymbol{e}}_{\rm b}\right. \\ &\quad + \left[2\left[(\boldsymbol{e}\cdot\hat{\boldsymbol{e}}_{\rm b})(\mathbf{j}\cdot\hat{\boldsymbol{L}}_{\rm b}) + (\boldsymbol{e}\cdot\hat{\boldsymbol{L}}_{\rm b})(\mathbf{j}\cdot\hat{\boldsymbol{e}}_{\rm b})\right]\boldsymbol{e}\right. \\ &\quad \left.\left. + 2\left[(\mathbf{j}\cdot\hat{\boldsymbol{L}}_{\rm b})(\mathbf{j}\cdot\hat{\boldsymbol{e}}_{\rm b}) - 7(\boldsymbol{e}\cdot\hat{\boldsymbol{L}}_{\rm b})(\boldsymbol{e}\cdot\hat{\boldsymbol{e}}_{\rm b})\right]\mathbf{j}\right]\times\hat{\boldsymbol{L}}_{\rm b}\right. \\ &\quad \left. + \frac{16}{5}(\boldsymbol{e}\cdot\hat{\boldsymbol{e}}_{\rm b})\mathbf{j}\times\boldsymbol{e}\right\}, \end{aligned} \tag{A2}$$

where we have defined $\mathbf{j} = \sqrt{1-e^2}\,\hat{\boldsymbol{L}}$. The terms in braces describe the octupole-level perturbation of the binary companion, where the relative 'strength' of the octupole term is quantified through the parameter $\varepsilon_{\rm oct}$, defined by equation (4). Note that in equations (A1) and (A2) we have introduced a characteristic (quadrupole) timescale for LK oscillations t_k, given by equation (3). Focusing only on the quadrupole terms, we note that the binary companion induces simultaneous precession and nutation of the orbital axis $\hat{\boldsymbol{L}}$ at a rate $\Omega_{\rm L} \equiv |d\hat{\boldsymbol{L}}/dt_{\rm quad}| = [(\Omega_{\rm pl}\sin\theta_{\rm lb})^2 + \dot{\theta}_{\rm lb}^2]^{1/2}$, see equation (5). From the standard equations for LK oscillations (in terms of orbital elements) to quadrupole order (e.g. Innanen et al. 1997),

$$\begin{aligned}\Omega_{\rm pl}\sin\theta_{\rm lb} &= \frac{3}{8t_k}\sin 2\theta_{\rm lb}\frac{(5e^2\cos^2\omega - 4e^2 - 1)}{\sqrt{1-e^2}} \\ \dot{\theta}_{\rm lb} &= -\frac{15}{16t_k}e^2\frac{\sin 2\theta_{\rm lb}\sin 2\omega}{\sqrt{1-e^2}}. \end{aligned} \tag{A3}$$

The value of $\Omega_{\rm L}$ therefore depends on the argument of pericentre ω. A good approximation to $\Omega_{\rm L}$ is

$$\Omega_{\rm L} \simeq \frac{3(1+4e^2)}{8t_k\sqrt{1-e^2}}|\sin 2\theta_{\rm lb}|. \tag{A4}$$

This expression is exact at both $e = 0$ and $e = e_{\rm max}$ (when $\omega = \pi/2$).

A2 Spin evolution due to the stellar quadrupole

We denote the spin angular momentum of the host star as $\boldsymbol{S}_\star = I_\star\Omega_\star\hat{\boldsymbol{S}}_\star$, where $I_\star = k_\star M_\star R_\star^2$ is the moment of inertia, $\Omega_\star$ is the spin frequency, and $\hat{\boldsymbol{S}}_\star$ is a unit vector along the spin axis. Note that we have introduced a coefficient $k_\star$, describing the interior mass distribution, where $k_\star = 0.1$ is used throughout this paper.

Due to the rotational distortion of the star, the stellar spin axis $\boldsymbol{S}_\star$ precesses around the orbital axis $\hat{\boldsymbol{L}}$ according to

$$\left.\frac{{\rm d}\boldsymbol{S}_\star}{{\rm d}t}\right|_{\rm SL} = \Omega_{\rm ps}\hat{\boldsymbol{L}}\times\boldsymbol{S}_\star, \tag{A5}$$

with the spin precession frequency $\Omega_{\rm ps}$ (see Section 2.1) given by equation (9).

The effects on the planetary orbit due to the stellar quadrupole are

$$\left.\frac{{\rm d}\boldsymbol{L}}{{\rm d}t}\right|_{\rm SL} = -\left.\frac{{\rm d}\boldsymbol{S}_\star}{{\rm d}t}\right|_{\rm SL} = \Omega_{\rm ps}\boldsymbol{S}_\star\times\hat{\boldsymbol{L}}, \tag{A6}$$

and

$$\left.\frac{{\rm d}\boldsymbol{e}}{{\rm d}t}\right|_{\rm SL} = -\dot{\omega}_\star\left[\cos\theta_{\rm sl}\hat{\boldsymbol{S}}_\star\times\boldsymbol{e} + \frac{1}{2}(1-5\cos^2\theta_{\rm sl})\hat{\boldsymbol{L}}\times\boldsymbol{e}\right], \tag{A7}$$

where $\dot{\omega}_\star$ quantifies the rate of apsidal precession due to the oblate star, and is given by

$$\dot{\omega}_\star = -\frac{S_\star}{L}\frac{\Omega_{\rm ps}}{\cos\theta_{\rm sl}} = \frac{3}{2}k_{q\star}\left(\frac{R_\star}{a}\right)^2\frac{\hat{\Omega}_\star^2}{(1-e^2)^2}\,n. \tag{A8}$$

A3 Pericenter precession due to short-range-forces

Besides the pericentre precession induced by the oblate host star, given in equation (A7), additional SRFs, due to general relativistic corrections, the (static) tidal bulge in the planet, and rotational distortion of the planet, induce precession of the eccentricity vector, given by (e.g. Correia et al. 2011; Liu et al. 2015)

$$\begin{aligned}\left.\frac{{\rm d}\boldsymbol{e}}{{\rm d}t}\right|_{\rm SRF} &= \left.\frac{{\rm d}\boldsymbol{e}}{{\rm d}t}\right|_{\rm GR} + \left.\frac{{\rm d}\boldsymbol{e}}{{\rm d}t}\right|_{\rm Tide} + \left.\frac{{\rm d}\boldsymbol{e}}{{\rm d}t}\right|_{\rm rot} \\ &= (\dot{\omega}_{\rm GR} + \dot{\omega}_{\rm Tide} + \dot{\omega}_{\rm rot})\hat{\boldsymbol{L}}\times\boldsymbol{e}, \end{aligned} \tag{A9}$$

where the precession frequencies take the form

$$\dot{\omega}_{\rm GR} = \frac{3\,GM_{\rm tot}}{c^2 a(1-e^2)} n, \tag{A10}$$

$$\dot{\omega}_{\rm Tide} = \frac{15}{2} k_{2\rm p} \frac{M_\star}{M_\rm p} \left(\frac{R_\rm p}{a}\right)^5 \frac{f_4(e)}{j^{10}} n, \tag{A11}$$

and

$$\dot{\omega}_{\rm rot} = \frac{3}{2} k_{qp} \left(\frac{R_\rm p}{a}\right)^2 \frac{\hat{\Omega}_p^2}{(1-e^2)^2} n, \tag{A12}$$

where $f_4(e)$ in equation (A11) is a dimensionless function of eccentricity, given in equation (A21), and in equation (A12) we have introduced a 'planetary rotational distortion coefficient' $k_{qp} = 0.17$, analogous to the stellar rotational distortion coefficient.

A4 Dissipative tides in the planet

The planet has spin angular momentum $\boldsymbol{S}_\rm p = I_\rm p \Omega_\rm p \hat{\boldsymbol{S}}_\rm p$, where $I_\rm p = k_\rm p M_\rm p R_\rm p^2$ is the moment of inertia, $\Omega_\rm p$ is the rotation rate, and where $k_\rm p = 0.25$ throughout this paper. Averaged over an eccentricity precession time-scale, the change in the planet spin due to tidal dissipation is (Correia et al. 2011)

$$\frac{1}{S_\rm p}\frac{{\rm d}\boldsymbol{S}_\rm p}{{\rm d}t} = -\frac{1}{2t_a j^{13}} \frac{L}{S_\rm p} \left[j^3 f_5(e)(\hat{\boldsymbol{S}}_\rm p + \cos\theta_\rm p \hat{\boldsymbol{L}}) \frac{\Omega_\rm p}{2n} - f_2(e)\hat{\boldsymbol{L}} \right], \tag{A13}$$

where $\cos\theta_p = \hat{\boldsymbol{S}}_\rm p \cdot \hat{\boldsymbol{L}}$, and $f_2(e)$ and $f_5(e)$ are given in equations (A19) and (A22). The time-scale t_a is

$$\frac{1}{t_a} = 6 k_{2\rm p} \Delta t_\rm L \frac{M_*}{M_\rm p} \left(\frac{R_\rm p}{a}\right)^5 n^2 \approx \frac{7.3\times10^{-21}}{\rm yr} \chi \bar{k}_{2\rm p} \frac{\bar{M}_\star \bar{M}_{\rm tot}}{\bar{M}_p} \frac{\bar{R}_p^5}{\bar{a}^8}, \tag{A14}$$

where $\Delta t_\rm L$ is the lag time, $k_{2\rm p}$ is the tidal Love number, and where we have introduced a tidal enhancement factor χ (relative to Jupiter), defined such that $\Delta t_\rm L = 0.1\chi$ sec. In this paper we assume $\boldsymbol{S}_\rm p = S_\rm p \hat{\boldsymbol{L}}$ (see Section 3.3 for a justification of this approximation), so that equation (A13) becomes

$$\frac{1}{S_\rm p}\frac{{\rm d}S_\rm p}{{\rm d}t} = -\frac{1}{2t_a j^{13}} \frac{L}{S_\rm p} \left[j^3 f_5(e) \frac{\Omega_\rm p}{n} - f_2(e) \right]. \tag{A15}$$

The effect of tidal dissipation on the orbit is

$$\left.\frac{{\rm d}\boldsymbol{L}}{{\rm d}t}\right|_{\rm Tide} = -\frac{{\rm d}\boldsymbol{S}_\rm p}{{\rm d}t} = -\dot{S}_\rm p \hat{\boldsymbol{L}}, \tag{A16}$$

The change in the eccentricity vector due to tidal dissipation takes the form

$$\left.\frac{{\rm d}\boldsymbol{e}}{{\rm d}t}\right|_{\rm Tide} = -\frac{1}{2t_a j^{13}} \left[j^3 f_4(e) \frac{\Omega_\rm p}{2n} (\boldsymbol{e}\cdot\hat{\boldsymbol{S}}_\rm p)\hat{\boldsymbol{L}} - \left(\frac{11}{2} j^3 f_4(e) \frac{\Omega_\rm p}{n} - 9 f_3(e) \right) \boldsymbol{e} \right], \tag{A17}$$

where the first term inside the brackets vanishes if $\hat{\boldsymbol{S}}_\rm p = \hat{\boldsymbol{L}}$. The dimensionless functions of eccentricity used to describe the tidal evolution take the form

$$f_1(e) = 1 + \frac{31e^2}{2} + \frac{255e^4}{8} + \frac{185e^6}{16} + \frac{25e^8}{64} \tag{A18}$$

$$f_2(e) = 1 + \frac{15e^2}{2} + \frac{45e^4}{8} + \frac{5e^6}{16} \tag{A19}$$

$$f_3(e) = 1 + \frac{15e^2}{4} + \frac{15e^4}{8} + \frac{5e^6}{64} \tag{A20}$$

$$f_4(e) = 1 + \frac{3e^2}{2} + \frac{e^4}{8} \tag{A21}$$

$$f_5(e) = 1 + 3e^2 + \frac{3e^4}{8}. \tag{A22}$$

A5 Stellar spin-down due to magnetic braking

We use the Skumanich law (Skumanich 1972), given by

$$\frac{{\rm d}\Omega_\star}{{\rm d}t} = -\alpha_{\rm MB}\,\Omega_\star^2 \Omega_\star, \tag{A23}$$

where we set $\alpha_{\rm MB} = 1.5\times10^{-14}$ yr to model G-type stars, and $\alpha_{\rm MB} = 1.5\times10^{-15}$ yr to model F-type stars (from Barker & Ogilvie 2009). See also Section 2.1.

This paper has been typeset from a TEX/LATEX file prepared by the author.